Chiral and topological spin textures and their ultrafast dynamics in thin-film materials with local inhomogeneities

Daniel Metternich

Angaben zur Veröffentlichung / Publication details:

Metternich, Daniel. 2026. “Chiral and topological spin textures and their ultrafast dynamics in thin-film materials with local inhomogeneities.” Augsburg: Universität Augsburg.

Chiral and topological spin textures and their ultrafast dynamics in thin-film materials with local inhomogeneities

Dissertation

zur Erlangung des akademischen Grades

Dr. rer. nat.

eingereicht an der

Mathematisch-Naturwissenschaftlich-Technischen Fakultät

der Universität Augsburg

von

Daniel Metternich

Augsburg, Juni 2025

Universität
Augsburg
University

Erstgutachter: Prof. Dr. Felix Büttner

Zweitgutachter: Prof. Dr. Hans Josef Hug

Drittgutachter: Prof. Dr. Reinoud Lavrijsen

Tag der mündlichen Prüfung: 08.12.2025

Abstract

Magnetic thin films with perpendicular anisotropy are widely studied as they exhibit a broad spectrum of magnetic domain textures and compelling properties for future spintronic and neuromorphic computing applications. A key factor influencing domain behavior is the chirality of the surrounding domain walls, which governs their stability, mobility, and topology. Since early research into bubble domain materials in the 1960s, the properties and dynamics of domain walls have been studied continuously. Although it has long been known that pinning at material defects affects domain walls, the ability to study these interactions at the microscopic level has been limited. Steady technological advancement in ultrafast excitation techniques and x-ray imaging now enables new insights into these nanometer-scale magnetic textures.

In this thesis, we examine how material defects and inhomogeneities affect the statics and dynamics of chiral and topological spin structures. We focus on three case studies, each targeting a distinct aspect of defect-induced magnetic behavior. For each project, we develop and deploy x-ray imaging and characterization techniques based on circular and linear magnetic x-ray dichroism contrast to resolve features spatially on the nanometer scale and with picosecond time resolution, supported by complementary measurements and modeling.

First, we investigate the impact of lateral inhomogeneities on the static domain wall chirality in DyCo thin films. Our vector imaging technique reveals strong lateral chirality variations imprinted by the local material properties, which appear to be influenced by the initial as-grown domain state.

Second, we utilize vector x-ray imaging to analyze domain wall defects in all-optically switched GdFe samples. Analysis of the defect density allows insights into the switching and nucleation dynamics of the domain wall itself. We uncover that post-nucleation domain wall propagation through an inhomogeneous material matrix is the dominant nucleation channel for domain wall defects.

Third, we study the laser-induced nucleation and localization of magnetic skyrmions in a patterned Co/Pt multilayer. We consolidate the homogeneous, exchange-driven nucleation of skyrmions after laser excitation with the observation that local anisotropy variations can induce a deterministic localization: We find that the localization is determined by purely local stability characteristics that induce skyrmion decay or proliferation.

Our findings collectively demonstrate how lateral material inhomogeneities govern both equilibrium configurations and dynamic processes of chiral and topological magnetic textures, offering key insights for future device design and fundamental studies of magnetic matter.

Contents

Acronyms

ASD atomistic spin dynamics

DMI Dzyaloshinskii–Moriya interaction

DOS density of states

FTH Fourier transform holography

HAPRE holography-aided phase retrieval

HI-AOS helicity-independent all-optical switching

L-TEM Lorentz transmission electron microscopy

LH linear horizontal

LLG Landau–Lifshitz–Gilbert equation

LV linear vertical

MFM magnetic force microscopy

MOKE magneto-optical Kerr effect

NIR near infrared

OOP out-of-plane

PEEM photoemission electron microscopy

PMA perpendicular magnetic anisotropy

RE rare-earth

SAXS small-angle x-ray scattering

SEM scanning electron microscopy

SEMPA scanning electron microscopy with polarization analysis

STEM scanning transmission electron microscopy

STXM scanning transmission x-ray microscopy

TM transition-metal

XAS X-ray absorption spectrum

XFEL x-ray free-electron laser

XMCD x-ray magnetic circular dichroism

XMLD x-ray magnetic linear dichroism

Chapter 1
Introduction

For many decades, magnetic thin films have been the focus of intense research and engineering efforts. On the one hand, they allow for fine-tuning of their magnetic properties by tuning not only their composition, but also the film thickness and layer stacking, which is in contrast to their bulk counterparts. On the other hand, magnetic thin films expose many unique magnetic phenomena: Not only are magnetic textures within thin films uniquely accessible to experimental observation techniques, their geometry also is the reason for many phenomena to emerge in the first place. One such phenomenon is perpendicular magnetic anisotropy (PMA). In a magnetic thin film with this property, the magnetization prefers to align collinear with the film normal, such that the magnetization either takes the magnetic state *up* or *down*. This binary distinction is the fundament for high density magnetic storage media, as it allows the creation of sub-micrometer-sized "bits" within a thin film that share one of these two magnetization directions. Understanding the physics of such magnetization textures in the form of magnetic domains on a fundamental level is not only the goal of countless research endeavors but also necessary for advanced future magnetization-based information storage and processing applications.

Of crucial importance for the behavior of magnetic domains are their boundaries, called domain walls. In domain walls, the magnetization gradually rotates by 180° from one perpendicular orientation to the other. The sense of the magnetization rotation from *up* to *down* orientation within the domain wall defines its chirality. Together with the domain wall width, this characteristic governs the behavior of the domain wall and – in extension – many properties of the domain. Exemplary, the chirality affects how (or even if) a domain wall moves in the presence of an external stimulus, such as an applied magnetic field [1, 2] or electric currents. The internal domain wall structure furthermore influences the stability, mobility, rigidity, and even topology of magnetic domains. In the context of field-induced magnetization reversal, the domain wall motion is also a determining factor in the nucleation and growth process. It is therefore of great interest to be able to control the domain wall chirality in the sense of selecting a certain chirality as well as determining the realized domain wall structure.

The domain wall characteristics can be tuned by manipulating the micromagnetic parameters of the system [3, 4]. Relevant properties include the anisotropy (the preferred orientation of the magnetization), the magnitude of the magnetization itself, and the strength of the exchange interaction between individual magnetic moments. Recently, asymmetric exchange in the form of the Dzyaloshinskii–Moriya interaction (DMI) has garnered interest as a tool to tune the domain wall chirality [5]. The presence of DMI favors the realization of one specific chirality, thereby suppressing other senses of rotation in the sample.

In many cases, it is sufficient to consider the domain wall as homogeneous along its spatial extent. Despite this stark simplification, the one-dimensional model accurately describes many aspects of field- and current-driven domain wall motion, such as the Döring mass and the Walker breakdown [6]. However, the one-dimensional model breaks down as soon as spatial variations in the domain wall chirality come into play. The most common of such chirality variations are domain wall defects in the form of Bloch lines, which form between two domain wall sections of opposing chirality. Bloch lines exhibit their own set of dynamics, as they can move along the domain wall, bunch up, or annihilate with other defects [7]. They are also particularly prone to being pinned at material defects in the magnetic film. These additional dynamics therefore impact the motion characteristics of the domain walls that host the Bloch line defects.

Material defects arise naturally during the deposition of the thin film. They encompass local deviations of the magnetic material from the perfect spatially homogeneous film. They can range from weak deviations like crystalline dislocations to changes in the film thickness and interface quality due to surface roughness. Of particular interest for this work are spatial variations of the composition in ferrimagnetic alloys. These spatial stoichiometry variations are suspected to play an important role in magnetization switching [8], but also in the formation of DMI [9] and even perpendicular anisotropy [10, 11] in these alloys. Material defects are generally undesirable, as they inhibit domain wall motion at low driving forces. They also facilitate the nucleation and trap the remnants of domains at applied magnetic fields far below or respectively above the film-averaged nucleation and collapse fields. These effects negatively impact the performance of the film for devices, as it broadens the switching-field characteristics of the magnetic film and makes motion of magnetic textures less predictable [12]. Despite continuous efforts to reduce the defect density by optimizing material deposition processes, some defects and inhomogeneities are intrinsically present in the materials. It is therefore paramount to understand the impact of material defects on magnetic structures. Furthermore, various successful attempts were made to harness artificially manufactured material defects to control the nucleation and movement of domains [13–16].

A lot of theoretical groundwork on films with perpendicular anisotropy was performed in the 1960s and 70s, when scientists investigated thin films with perpendic-

ular anisotropy as hosts for small, circular "bubble" domains. While these bubble materials were not commercially successful in data storage devices, research on them highlighted the importance of the domain walls, including the wall-internal defect structure [6, 17–19]. Some theoretical works also found a connection between material inhomogeneities and the creation of Bloch line defects in the domain walls [20, 21]. However, at the time, experimental imaging techniques were limited in spatial and temporal resolution and contrast. Available methods with sensitivity to the chiral information within the domain walls were mostly restricted to optical Kerr- and Faraday-microscopy, which is resolution limited by the optical wavelength, and Lorentz transmission electron microscopy (L-TEM), which has superior resolution but requires strong magnetic moments for adequate contrast.

Today, magnetic imaging methods have matured and developed considerably. Optimized experimental setups, improved measurement routines and sophisticated data processing allow us to resolve magnetic features down to tens of nanometers in size, in films that are only a few monolayers in thickness and time resolutions of femtoseconds. Together with improvements in optical and electron microscopy [22], as well as scanning probe techniques (magnetic force microscopy (MFM) and polarized scanning transmission electron microscopy (STEM)), x-ray magnetic imaging has been established as a powerful tool to investigate microscopic magnetic textures in thin films. With the discovery of x-ray magnetic dichroism at element specific absorption edges [23], it is possible to selectively observe magnetic features with strong, element-specific contrast by using polarized x-rays at synchrotron facilities. Besides volume averaging spectroscopy and scattering techniques, dichroism-based imaging methods include photoemission electron microscopy (PEEM), scanning transmission x-ray microscopy (STXM) and Fourier transform holography (FTH) [24]. Recently, with the help of fast parallelized computational resources, novel algorithms push the spatial resolution towards the level of electron microscopes via coherent imaging [25, 26].

A second critical technological advancement has been the development of optical and near infrared (NIR) lasers that can emit femtosecond long pulses. Since the discovery of ultrafast demagnetization by Beaurepaire et al. [27], the reaction of many magnetic systems to ultrashort optical stimuli has been investigated. One groundbreaking discovery was the phenomenon of all optical switching, where a laser pulse could deterministically switch the magnetization direction in a ferrimagnetic thin film [28, 29]. Another recent development was the possibility to nucleate skyrmions by applying a single ultrashort laser pulse to a ferromagnetic multilayer. Magnetic skyrmions are the conceptual successor to magnetic bubbles, as they are essentially also circular domains. However, their domain wall is defect free, which gives them a topological charge. The emergence and existence of topologically non-trivial magnetic textures makes these material systems uniquely suited to experimentally investigate the evolution, creation and annihilation of topological

charge on ultrafast time scales. How these optically created skyrmions form and if potential material defects play a role in that process is still not fully understood.

In this thesis, we investigate the influence of material defects and lateral inhomogeneities on chiral spin structures in the form of domain walls and magnetic skyrmions. We develop vector reconstruction techniques based on x-ray-based imaging methods to resolve the internal domain wall structure. These techniques allow us to determine the local chirality as well as to distinguish Bloch line defects in rare-earth transition metal alloys. We study the creation of domain wall defects during all-optical switching and find a strong link between the Bloch line creation and material defects. Similarly, we explore how the localization of magnetic skyrmions during an optically induced topological phase transition depends on spatial variations of the magnetic material. Finally, we uncover strong domain wall chirality variations that are not dynamically created defects but instead are imprinted by the host material itself.

The thesis consists of three independent investigations that each focus on one facet of the impact that material inhomogeneities have on chiral spin structures. After a general overview of the required fundamental physical concepts in chapter 2 and a brief introduction into the experimental techniques in chapter 3, each of the following three chapters reports on one of these investigations.

Chapter 4 is based around the development of a novel linear X-ray dichroism-based imaging technique for the investigation of local domain wall chirality. In combination with coherent imaging techniques, this method enables the full reconstruction of the domain-wall magnetization with 15 nm spatial resolution, which has not been achieved before with sub-surface sensitivity. Deploying this technique on a ferrimagnetic DyCo-alloy revealed the coexistence of extended Bloch- and Néel -type domain walls within the same sample. Besides being a hint for the presence of bulk DMI in the material, this coexistence also indicates an apparent spatial inhomogeneity of magnetic parameters that allow such chirality variations. Successive ultra-sensitive MFM measurements revealed a field-independent contrast pattern below the ferrimagnetic domains, which appears to be growth related. While we could not find an obvious coincidence between these features and the domain wall chirality, the data suggests a spatial composition variation that arises from an interplay of the sample's composition and its own magnetic stray fields during the growth process. These findings have been compiled into a publication, which is still work in progress. However, submission is postponed until the nature and origin of these unexpected additional features has been confirmed.

In chapter 5, we resolve the static domain wall structure after single-shot all-optical switching in GdFe thin films. We find high densities of vertical Bloch line defects, irrespective of the optical excitation parameters. By comparing different samples and optical nucleation with field induced switching, we highlight the impact of material defects on the Bloch line creation. The contents of this chapter have been

published in the journal *Structural Dynamics* [30]. Paragraphs that are identical to the paper manuscript or were only modified slightly, are marked with the symbol †. These sections were written by the author and subsequently iterated with the coauthors of the publication.

Finally, in chapter 6 we focus on the localization mechanism of magnetic skyrmions upon nucleation with an ultrafast optical stimulus. We investigated this process by performing time-resolved small angle x-ray scattering SAXS at an x-ray free electron laser source. By patterning a magnetic cobalt platinum multilayer with artificial nucleation sites, we could separate the scattering contributions from localized and non-localized magnetic features. By matching experimental data to atomistic spin dynamics simulations, we found that the localization of skyrmions is a local, decay dominated process, which sets in after the system exits the initial fluctuation regime. A manuscript for publication of these results is currently in preparation.

The main results of the thesis are summarized in chapter 7. Additionally, we discuss the ramifications of our results on the current scientific discourse and propose possible follow-up experiments. Finally, supplementary measurements are reported on in the appendix.

Chapter 2
Fundamentals

In this thesis, we investigate the formation, stability, and dynamics of a wide range of complex spin structures in magnetic thin films. These complex spin structures include domains, domain walls and topological features, such as domain wall defects and skyrmions. All these textures represent non-uniform arrangements of magnetic moments (compare Fig. 2.1a). The behavior of spin textures is governed by a delicate interplay of exchange interactions, magnetostatic energy, anisotropy, and other spin-orbit coupling effects, such as the Dzyaloshinskii-Moriya Interaction (DMI). Understanding the influence of each of these contributions to the formation of magnetic textures and how they can be used to tune magnetic behavior is essential for designing experiments involving such textures and interpreting their outcomes effectively.

Magnetic features emerge from collective quantum interactions within ensembles of particles. The theoretical description of such systems is overly complex, with analytical solutions existing only for a few exceptionally simple cases. Moreover, first-principles computational approaches for magnetic systems are limited in the simulated ensemble size by current computational resources.

Micromagnetic treatment offers a convenient theoretical framework for understanding and modeling meso-scale magnetic textures – structures that are significantly larger than the atomic spacing. Instead of representing individual spins, the micromagnetic approach treats the magnetization in materials as a continuous vector field $\mathbf{M}$. This field locally represents the collective average magnetization, characterized by a magnitude M_s and a direction $\mathbf{m}$. By reducing the complexity of the problem, micromagnetics enable the accurate modeling and analysis of a wide range of spin textures, providing sufficient precision to address the concepts and results explored in this thesis.

The following section provides a brief overview of the key competing micromagnetic terms involved in determining the magnetic behavior. With these basic interactions established, we introduce various spin textures in order of increasing complexity. One kind of these spin textures are magnetic skyrmions. In their context, we introduce topology, skyrmion stability, as well as recent advances in skyrmion nucleation with ultrashort laser pulses. Lastly, we introduce the material class of

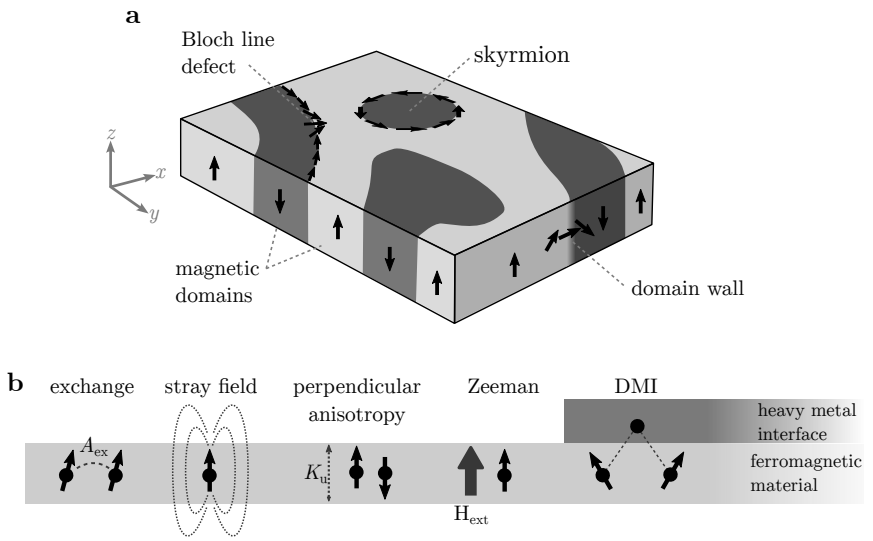

Figure 2.1 | Magnetic textures and micromagnetic energy contributions involved in their formation. **a** Sketch of a complex magnetic domain landscape in a ferromagnetic thin film, including examples of objects that are discussed in this thesis. Extended adaptation from [3]. **b** Sketch of the impact of each micromagnetic energy term that contributes to the formation of complex spin textures.

ferrimagnetic rare-earth transition-metal alloys, focusing on the phenomenon of all-optical magnetization switching that can be observed in these materials.

2.1. Micromagnetism

Micromagnetic textures are governed by a set of competing interactions (compare Fig. 2.1b). Each interaction influences the orientation of the magnetization vector $\mathbf{M}$ in a characteristic way:

- The **magnetic exchange** is the fundamental interaction between individual magnetic moments to establish magnetic order and favors uniform magnetization alignment. Depending on the sign of the exchange constant A_{ex}, parallel or antiparallel alignment is favored between neighboring magnetic moments.

- **Magnetic anisotropy** describes the tendency of the magnetization to align along one (or multiple) preferred axis. In our thin films, the magnetization prefers alignment along the film-normal (z), which has been coined as perpendicular magnetic anisotropy (PMA).

- **Stray fields** act against the PMA and exchange and are the main contributor in breaking a uniform magnetization state into multiple domains.

- The **Dzyaloshinskii-Moriya interaction** (DMI) favors a chiral orthogonal alignment of neighboring moments and thus results in the creation of chiral domain walls (i. e., domain walls with one preferred sense of rotation).

- Finally, a finite magnetic moment tends to align with an applied magnetic field $\mathbf{H}_{\text{ext}}$, due to the **Zeeman** energy.

The impact of all contributions acting on the magnetization is expressed in the total energy of the spin system

$$E_{\text{tot}} = E_{\text{exchange}} + E_{\text{anisotropy}} + E_{\text{Zeeman}} + E_{\text{demag}} + E_{\text{DMI}}, \tag{2.1}$$

where each energy term E_i is the volume integral of a local energy density $\epsilon_i(\mathbf{M})$ [31]. In the following, we briefly evaluate the form of each individual contribution as well as their origin.

2.1.1. Magnetic exchange

The exchange interaction is fundamental for magnetic order. The exchange stiffness gives rise to the energy density

$$\epsilon_{\text{exchange}} = A_{\text{ex}} \left[(\nabla m_x)^2 + (\nabla m_y)^2 + (\nabla m_z)^2 \right], \tag{2.2}$$

where ∇m_i is the local gradient of the magnetization and A_{ex} the material specific exchange stiffness [3]. The exchange stiffness term represents the direct Heisenberg interaction between neighboring spins in a magnetic material that arises as an interplay of Coulomb repulsion and the Pauli exclusion principle [32]. Despite the fundamental picture of localized spins, the model also holds true in good approximation for non-localized magnetic moments, i. e. metallic band magnetism. Depending on the sign of the exchange interaction, spins favor parallel (ferromagnetic) or antiparallel (antiferromagnetic) alignment.

In this thesis, we consider ferro- and ferrimagnetic materials. While the latter show antiparallel alignment between two different sublattices, the net magnetic moment represents the average of many magnetic moments from both species. We may therefore treat the ferrimagnet like a ferromagnet with a reduced magnetization magnitude M_{s}.

The exchange stiffness favors (anti-)parallel alignment of neighboring magnetic moments. Hence, uniform textures and slow, gradual changes of the magnetization orientation incur a smaller energy penalty than abrupt spatial transitions of the magnetization direction.

2.1.2. Anisotropy

The magnetic anisotropy describes the preference of the magnetization to align with a specific energetically "easy" axis, multiple equivalent axes, or an easy plane. In this thesis, we exclusively discuss films that exhibit perpendicular magnetic anisotropy (PMA). In this case, the magnetization favors out-of-plane orientation, hence collinear alignment with the film normal $\mathbf{n} = (0,0,1)$. The micromagnetic energy is thus formalized as

$$\epsilon_{\text{anisotropy}} = -K_{\text{u}}(\mathbf{n} \cdot \mathbf{m})^2, \tag{2.3}$$

with the anisotropy strength K_{u}. Multiple effects contribute to the sign and magnitude of K_{u}, including magneto-crystalline, strain-induced, and interfacial anisotropy terms.

The *magneto-crystalline anisotropy* is connected to the local crystal structure and is a bulk material property. Exemplary, cubic bulk iron has three easy axes along the <100> crystal directions [31]. *Strain anisotropy* stems from deformations of the crystal lattice, e. g., due to a lattice mismatch between the substrate or seed layer and the magnetic film. The *interfacial anisotropy* arises from symmetry breaking at the interface between two different materials or at the surface of the thin film. This symmetry breaking leads to modifications in the electron orbitals in the direction of the interface, while orbitals in the plane are less affected. In a Co-based multilayer, these interface interactions at periodically repeating material interfaces dominate the other anisotropy contributions.

Amorphous rare-earth transition-metal alloys show strong perpendicular anisotropy, even in relatively thick films. The exact origin of the PMA in this material class is still under debate and a multitude of different origins for the anisotropy have been proposed [33, 34]. Theories for the origin of PMA range from pseudocrystalline short-range order in the amorphous matrix [35] over selective resputtering during deposition that leads to pair ordering [36, 37] to the growth of columnar structures in the thin film [38] and magnetoelastic coupling [39]. The more generally accepted theories propose a structural origin from anisotropic packing of nearest neighbors in-plane versus along the film normal [40, 41], with strong evidence from x-ray absorption fine-structure measurements [42].

2.1.3. Stray fields – demagnetizing energy

The demagnetizing energy is caused by the fact that each finite magnetic moment within the sample creates its own magnetic field. Hence, the finite magnetization of a magnetic sample leads to a stray field inside and outside the material itself.

This stray field is compensated by an internal demagnetizing field $\mathbf{H}_\mathrm{d}$, which leads to the local energy density [31]

$$\epsilon_\mathrm{demag} = -\frac{\mu_0}{2}\mathbf{H}_\mathrm{d} \cdot \mathbf{M}. \tag{2.4}$$

Because the stray field and therefore the local demagnetizing field depends on the global magnetic texture, the numerical treatment of stray field-related effects is not straightforward and usually the most computationally expensive calculation. However, the demagnetization energy generally tends to minimize external magnetic stray fields, which has two important consequences: True to its name, the demagnetization energy is the main drive for the formation and stabilization of magnetic domains. Dividing the material into regions with different magnetization directions allows for the suppression of far-reaching stray fields. In our films with perpendicular anisotropy, only two types of domains coexist, with their magnetization pointing parallel or antiparallel to the film normal.
Assuming a monodomain state, in which all magnetic moments point in the same direction, stray field minimization prefers the magnetization to lie within the film plane. This preference for an in-plane orientation is called shape anisotropy and acts against the local perpendicular anisotropy K_u, which prefers out-of-plane magnetization alignment. The strength of this easy-plane contribution to the anisotropy is well described by Stoner and Wohlfahrt [43], assuming an infinite aspect ratio between film extent and thickness and can be quantified as $\frac{\mu_0 M_\mathrm{s}^2}{2}$. Combining the local anisotropy with the shape effects results in the total effective anisotropy

$$K_\mathrm{eff} = K_\mathrm{u} - \frac{\mu_0 M_\mathrm{s}^2}{2}. \tag{2.5}$$

If K_u is larger than the shape anisotropy term, the magnetic film exhibits PMA. If the shape anisotropy is larger than K_u, however, the film tends to form in-plane textures. The same relation is expressed in the quality factor

$$Q = \frac{2K_\mathrm{u}}{\mu_0 M_\mathrm{s}^2}, \tag{2.6}$$

which needs to satisfy $Q > 1$ for effective perpendicular anisotropy [44].

2.1.4. Dzyaloshinskii-Moriya interaction

The Dzyaloshinskii–Moriya interaction (DMI) [45, 46] is an indirect, asymmetric exchange coupling between magnetic moments. It requires the presence of spin orbit coupling and local breaking of inversion symmetry. DMI favors spiraling spin structures with a specific sense of rotation, which depends on the sign of the DMI-contant D. In our samples, strong DMI facilitates the formation of domain

walls with a specific Néel chirality (see section 2.2). This effect is formalized in the micromagnetic energy density contribution

$$\epsilon_{\mathrm{DMI}} = D\left[M_z \nabla \mathbf{M} - (\mathbf{M} \cdot \nabla) M_z\right] \tag{2.7}$$

within a magnetic thin film [1].
One distinguishes between bulk and interfacial DMI. Bulk DMI is a material specific effect and arises, e. g., in B20-crystals, in which the crystal structure itself is non-centrosymmetric [47]. Recently, bulk DMI was also reported in the rare-earth transition-metal GdFeCo, where symmetry breaking originated from a growth-induced material composition gradient [9]. In contrast, interfacial DMI arises at interfaces between a magnetic film and a heavy metal due to strong spin-orbit coupling between the magnetic moments and the heavy metal atoms. Symmetry is inherently broken at an interface. Interfacial DMI arises at the interface, but the effect quickly diminishes further away from the interface. Therefore, interfacial DMI mostly plays a role in films that are only few nanometers thick and in repeating multilayer structures. Furthermore, the sign of the interfacial DMI depends on the stacking order of the magnetic and heavy metal layer. Contributions from identical interfaces on both sides of a magnetic film therefore tend to cancel each other.

2.1.5. Applied magnetic fields – Zeeman energy

Similar to the demagnetizing field contribution, applying an external magnetic field to the film modifies the energy of each magnetic moment depending on the direction of the moment with respect to the applied field [31]:

$$\epsilon_{\mathrm{Zeeman}} = -\mu_0 \mathbf{H} \cdot \mathbf{M} \tag{2.8}$$

Hence, the Zeeman-contribution acting on a finite magnetization prefers alignment of the magnetic moments with the magnetic field vector.

2.1.6. Dynamics: The Landau-Lifshitz-Gilbert equation

In magnetostatics, the magnetic configuration represents an energy minimum, which constitutes either the energetic ground state (hence, the absolute energy minimum) or a metastable state (a local minimum). Hence, to find a (meta-) stable magnetic state, minimization of the total energy E_{tot} is sufficient. The treatment of magnetization dynamics, however, requires solving (or computing) the Landau–Lifshitz–Gilbert equation (LLG)

$$\frac{\mathrm{d}\mathbf{M}}{\mathrm{d}t} = \gamma \mathbf{M} \times \mathbf{H}_{\mathrm{eff}} + \frac{\alpha}{M_{\mathrm{s}}} \mathbf{M} \times \frac{\partial \mathbf{M}}{\partial t}, \tag{2.9}$$

with the gyromagnetic ratio γ and the Gilbert damping α [48, 49]. The expression $\mathbf{H}_{\text{eff}}$ translates the torque that all energy contributions exert on the magnetization into an effective magnetic field, defined as the functional derivative

$$\mathbf{H}_{\text{eff}} := -\frac{1}{\mu_0}\frac{\delta E_{\text{tot}}}{\delta \mathbf{M}}. \tag{2.10}$$

The Gilbert damping factor α is a phenomenological property that indicates how fast a precessing magnetization dissipates angular momentum and returns to the equilibrium position.
To conclude, the local micromagnetic properties of a magnetic film are described by a set of parameters, namely the exchange stiffness A_{ex}, the saturation magnetization M_{s}, the anisotropy strength K_{u} and the DMI constant D. To describe dynamics, also the Gilbert damping α is necessary. Knowledge of all parameters is required for proper micromagnetic treatment of a sample system. Note that these parameters are not only material specific but also vary with temperature.

2.2. Magnetic domain walls

In ferro- and ferrimagnetic thin films, regions of opposite magnetization direction are called magnetic domains. The transition region between two neighboring magnetic domains is called a magnetic domain wall. In these domain walls, the magnetization vector $\mathbf{M} = (M_{\text{x}}, M_{\text{y}}, M_{\text{z}})$ rotates continuously from one out-of-plane direction $\mathbf{M} = (0, 0, M_{\text{s}})$ to the inverted direction $\mathbf{M} = (0, 0, -M_{\text{s}})$. The manner of rotation largely impacts the static and dynamic properties of the domain walls and therefore the domains themselves.
Many domain wall characteristics can be discussed in a one-dimensional model, where only changes of the magnetization normal to the domain wall are considered. In this simplified model, the magnetization profile along the domain wall normal x is well described by

$$\mathbf{M}(x) = M_{\text{s}} \begin{pmatrix} \cosh^{-1}(x/\Delta)\cos(\psi) \\ \cosh^{-1}(x/\Delta)\sin(\psi) \\ \tanh(x/\Delta) \end{pmatrix}, \tag{2.11}$$

where Δ is the domain wall width parameter and ψ the transverse domain wall angle, as indicated in Fig. 2.2a [6]. The width of the domain wall, in which the transition from the spin up to the spin down orientation, or vice versa, takes place, is $\pi\Delta$, with

$$\Delta = \sqrt{\frac{A}{K_{\text{eff}}}}. \tag{2.12}$$

Hence, the domain wall width increases with the exchange parameter and decreases with the anisotropy strength. Both can be understood intuitively, as the exchange

energy prefers larger, slowly rotating magnetic structures, while the perpendicular anisotropy term is unfavorable if the magnetization is not collinear with the film normal.

The transverse domain wall angle ψ defines the chirality of the domain wall, i. e., how the magnetization rotates in the transition between the two out-of-plane magnetizations. For $\psi = \pm\pi/2$, the magnetization rotates exclusively in the (y,z)-plane of the domain wall. Such a configuration is called a Bloch domain wall. For $\psi = 0$ and $\psi = \pi$, the magnetization rotates in the (x,z)-plane, hence, the magnetization tilts in the direction of the normal vector of the domain wall. These domain walls exhibit Néel chirality (compare Fig. 2.2b). Solely taking exchange, anisotropy and demagnetizing fields into account, Bloch walls are energetically preferred over Néel walls or intermediate states [6]. The magnetization component normal to the domain wall gives rise to magnetic volume charges at the edges of the domain wall (see Fig. 2.2a). The resulting demagnetizing fields, which increase the total energy of the wall, are absent in a domain wall with Bloch chirality. To make Néel type domain walls energetically favored, in-plane fields or in-plane anisotropies ar required [6]. A third way to stabilize Néel domain walls is the introduction of sufficiently strong DMI to overcome the energy penalty from volume stray fields. The total energy per domain wall section follows the expression [50]

$$\sigma_{\mathrm{DW}} = 4\sqrt{A_{\mathrm{ex}} K_{\mathrm{eff}}} \pm \pi D. \tag{2.13}$$

Intuitively, the in-plane, twisting magnetization structure leads to an energy penalty from the exchange and anisotropy terms. DMI favors one Néel orientation over the other. Hence, the domain wall energy increases or decreases with the DMI strength, depending on the present chirality. The domain wall angle ψ can be calculated via

$$\cos(\psi) = \begin{cases} -D/D_{\mathrm{thr}}, & |D| < D_{\mathrm{thr}} \\ -\mathrm{sgn}(D), & |D| \geq D_{\mathrm{thr}} \end{cases} \tag{2.14}$$

with the threshold DMI strength

$$D_{\mathrm{thr}} = \frac{2\mu_0 M_{\mathrm{s}}^2}{\frac{\pi^2}{t\ln(2)} + \pi\sqrt{\frac{K_{\mathrm{u}} + \frac{\mu_0 M_{\mathrm{s}}^2}{2}}{A_{\mathrm{ex}}}}} \tag{2.15}$$

where t is the thickness of the magnetic sample [51]. As expected, for $D = 0$, the wall is Bloch-type with two degenerate solutions, $\psi = \pm\pi/2$. For $|D| \geq D_{\mathrm{thr}}$, the domain wall exhibits one specific Néel handedness and smaller values stabilize intermediate states.

The one-dimensional model breaks down if the chirality is not homogeneous along the domain wall. Besides lateral inhomogeneities and domain wall defects (see next section), the chirality may also vary along the thickness direction of the film

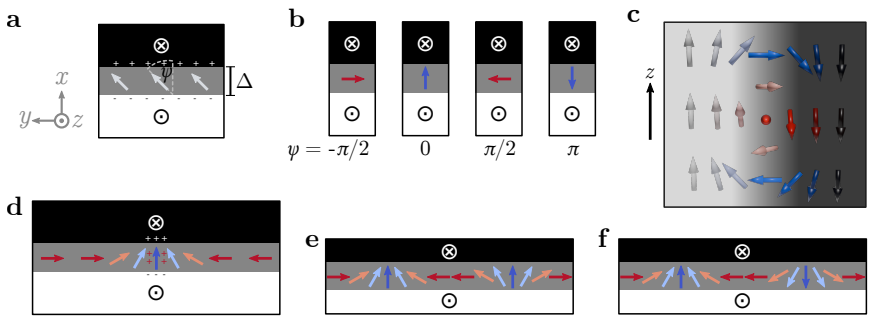

Figure 2.2 | Static domain wall textures. **a** One-dimensional domain wall with intermediate transversal domain wall angle ψ, domain wall width parameter Δ and magnetic volume charges. **b** Néel and Bloch type domain walls with opposing chirality. **c** Vertical cross section through a domain wall with flux closure end caps. **d** Bloch line defect between two Bloch domain wall sections with opposite polarity. **e** Unwinding and **f** winding pair of vertical Bloch lines

due to flux closure effects. These phenomena arise in thick magnetic films, where the film thickness is larger than the exchange length $l_{\mathrm{ex}} = \sqrt{\frac{2A_{\mathrm{ex}}}{\mu_0 M_{\mathrm{s}}^2}}$ [52, 53] and in exchange-decoupled multilayer systems [54]. In such samples, the tendency to minimize stray fields leads to a chirality profile as shown in Fig. 2.2c [55]: Without DMI, the center of the domain wall is Bloch type but towards the top and bottom of the film the chirality rotates towards two Néel configurations with opposite chirality ($\psi = 0$ and $\psi = \pi$). The stray field induced stabilization of Néel chirality acts like an effective DMI, that varies in magnitude and also changes sign across the thickness dimension. As a result, the required DMI to achieve full uniform Néel chirality across the entire layer increases: Irrespective of the sign of the DMI, at one layer surface the effective DMI opposes the desired Néel chirality [54].

2.2.1. Vertical Bloch lines

The two possible polarities of a Bloch wall are energetically degenerate [6]. Therefore, no polarity is preferred and both appear with equal likelihood in a magnetic domain texture. If sections of opposite polarity are present within the same domain wall, at their contact point the in-plane domain wall angle ψ must rotate by 180°. Such a defect in the domain wall structure is called a vertical Bloch line, in which the in-plane magnetization rotation results in a locally confined Néel configuration (compare Fig. 2.2d). Similar to how the manner of rotation of the magnetization in a domain wall can be classified in terms of chirality, the handedness of a Bloch line can be assigned based on the sense of rotation of ψ. The shape of a vertical Bloch line is determined by the interplay of two types of arising magnetic charges: On one hand, the local Néel character induces volume charges transversal to the domain wall. On the other hand, the converging or diverging Bloch sections on

either side of the vertical Bloch line induce a magnetic charge within the Bloch line. The balance of these two contributions, in conjunction with the exchange stiffness, lead to the profile of the domain wall angle

$$\psi(y) = \pm \arctan(\exp(y/\Lambda_0)), \tag{2.16}$$

with the vertical Bloch line width parameter $\Lambda_0 = \pi\sqrt{2\mu_0 A_{\mathrm{ex}}/M_{\mathrm{s}}^2}$ [3].
In a closed domain wall (e. g., of a circular bubble domain), vertical Bloch lines must always exist in pairs. Bloch lines preferably form at material inhomogeneities and pinning sites during domain wall dynamics [20]. Additionally, due to the energy degeneracy of Bloch walls polarities, Bloch lines are expected to form naturally in many material systems.
As a continuous rotation of the in-plane magnetization, isolated vertical Bloch lines can easily propagate along the domain wall. At distances much larger than their own size, multiple consecutive Bloch lines along the same domain wall section always attract each other: The volume charge created by the opposing Bloch walls on both sides of the defect alternates between consecutive Bloch lines because after each Bloch line with converging Bloch wall sections a Bloch line with diverging Bloch walls must follow. The volume charge is therefore opposite, which leads to long-range attraction and causes Bloch lines to form clusters [6].
Once the distance of Bloch lines is comparable to their extent, the interaction of consecutive Bloch lines depends on the sense of rotation from one Bloch polarity to the other [3, 6]. At small distances, vertical Bloch lines with opposite handedness (Fig. 2.2e) annihilate upon contact and continuously unwind their magnetic configuration into the defect-free Bloch wall. However, two neighboring Bloch lines with the same handedness cannot merge continuously. As the distance decreases, the angle ψ must rotate more rapidly from one Néel chirality to the other. This rotation would become essentially discontinuous if the centers of the Bloch lines were to contact each other. As a result, the diverging exchange energy enforces a minimum distance between winding pairs of vertical Bloch lines [6].

2.2.2. Field-driven domain wall motion

If an out-of-plane magnetic field is applied to an equilibrium multi-domain state, one magnetization direction becomes energetically favored over the other due to the Zeeman energy (see equation (2.1)). To reach the new global energy minimum, domains with the energetically favorable orientation expand at the expense of neighboring domains with opposite magnetization. The result is field-driven motion of the domain walls.
The simplest way to model domain wall propagation is once again a one-dimensional model, which assumes homogeneous dynamics along the entire domain wall. The sketch in Fig. 2.3a depicts a Bloch wall traveling along the x-direction when field

is applied along the z-axis. Colored vectors indicate the involved torques that act on the magnetization within the wall. According to the LLG-equation 2.9, the applied external field $\mathbf{H}$ induces a precession $\boldsymbol{\tau}_\mathrm{p}$ of the magnetization in the plane, while the damping term $\boldsymbol{\tau}_\alpha$ acts in the direction of the applied field, hence in the direction of the favorable magnetization [56]. Because the magnetization is tilted away from the Bloch configuration towards a Néel chirality, volume charges form on both sides of the domain wall, leading to a demagnetizing field $\boldsymbol{H}_\mathrm{K}$ in the x-direction. Importantly, this demagnetizing field creates a damping torque $\boldsymbol{\tau}_{\mathrm{K},\alpha}$, which opposes the precessional term caused by the applied field and increases further as the magnetization is canted away from the equilibrium chirality. The precessional term $\tau_{\mathrm{K,p}}$ that originates from the demagnetizing field further enables the rotation of the magnetization towards the preferred out-of-plane magnetization direction [6].

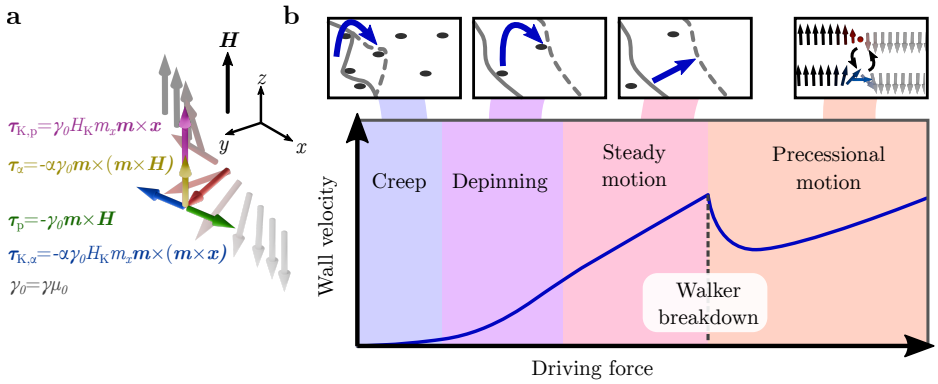

Figure 2.3 | Field-induced domain wall motion. a Individual torques $\boldsymbol{\tau}$ acting on a moving domain wall under an applied out-of-plane field in the one-dimensional picture. At rest, the domain wall has Bloch chirality. **b** Qualitatively different motion regimes. The domain wall velocity is plotted against an external driving force, e. g., an applied magnetic field. Insets sketch the characteristic domain wall dynamics in the respective motion regime. Graphics adapted from [56].

As long as the external field is moderate, a dynamic steady state configuration can be achieved, where the precessional term from the external field and the restorative damping term are equal. In this case, the domain wall travels with a constant chirality that deviates from the static Bloch chirality, up to full Néel chirality. The propagation speed is proportional to the applied field strength. If, however, the applied field is strong enough such that restorative forces cannot stabilize the precessional term, the domain wall continuously precesses in the plane and the chirality periodically changes from Bloch to Néel. This continuous precession leads to an oscillating domain wall speed and generally results in a decrease of the propagation velocity compared to steady-state motion [55]. The driving field

at which the precessional motion sets in is called the Walker breakdown field B_{W} (compare Fig. 2.3b).

Extending the domain wall model to three dimensions introduces multiple new phenomena into the picture of domain wall motion. Material imperfections can trap the domain wall at pinning points, e. g., regions of reduced anisotropy, where the in-plane components of the domain wall are more energetically favorable. At low driving fields, this domain wall pinning leads to energy barriers that need to be overcome, e. g., by thermal activation, after which the domain wall jumps to the next pinning site [57]. This domain wall creep reduces the domain wall speed at low driving fields, while at larger fields, pinning no longer plays a significant role ("depinning"-regime). The motion regimes are illustrated in figure 2.3b for a domain wall depinning threshold far below B_{W}. Depending on the Walker field, the temperature, and the pinning strength, it is possible that the Walker breakdown is masked entirely by pinning related effects [58].

A three-dimensional domain wall picture also allows for the dynamic creation and motion of internal domain wall defects during propagation [59]. Similarly to the Walker breakdown, vertical and horizontal Bloch lines form if the external driving force reaches a particular threshold [6, 21, 55]. Under an applied magnetic field, Bloch lines easily move along the domain wall. These dynamics lead to a reduction in the domain wall mobility. The presence of Bloch lines tends to distort the domain wall shape, as Bloch lines are more easily pinned and, in general, exhibit lower mobility than a defect free domain wall section. Additionally, Bloch lines tend to bunch up, hence forming clusters, which lead to highly inhomogeneous wall mobility [6].

2.3. Magnetic skyrmions

Skyrmions are circular domains with non-trivial topology. The topological charge of a two-dimensional magnetic texture is defined as [60]

$$Q = \frac{1}{4\pi} \int \mathbf{m} \cdot \left(\frac{\partial}{\partial x}\mathbf{m} \times \frac{\partial}{\partial y}\mathbf{m} \right) \mathrm{d}x \, \mathrm{d}y. \tag{2.17}$$

This quantity measures how many times the magnetization winds around the unit sphere [61]. A more instructional expression for the topological charge is

$$Q = P \cdot W, \tag{2.18}$$

where the polarity P indicates whether the OOP-magnetization inside the domain points into or out of the plane and W is the winding number of the domain. W is defined by the structure of the surrounding domain wall, which therefore dictates the topological charge, assuming a fixed polarity.

Skyrmions take the form of circular domains with a defect-free domain wall, as illustrated in Fig. 2.4. They therefore carry a topological charge of $Q = \pm 1$ with $P = \pm 1$ and also $W = \pm 1$. Even though the topology is encoded in the structure of the domain wall, the domain wall angle ψ does not influence the topological charge. However, the chirality influences the dynamic characteristics of the skyrmion, e. g., the response to electric current excitations. The topological charge leads to a gyroscopic Magnus force, which induces motion perpendicular to the excitation current in the form of the skyrmion Hall effect [62, 63]. This deflection angle varies, depending on the chirality of the skyrmion [64, 65].

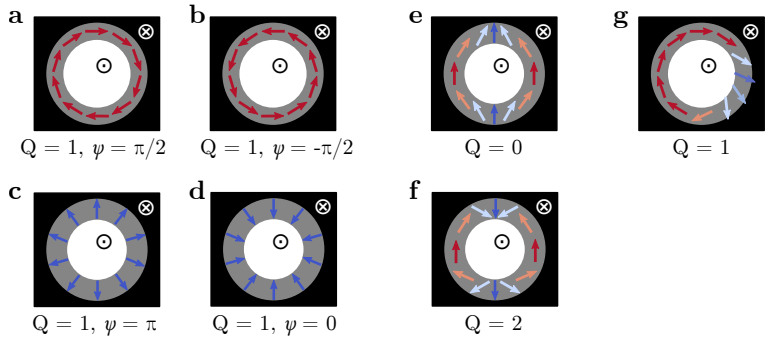

Figure 2.4 | Topology of circular domains defined by the domain wall structure. All domains have the same polarity $P = 1$ but varying winding numbers W. **a-d** Magnetic skyrmions with topological charge $Q = 1$ and winding number $W = 1$ and various domain wall chiralities. **e** Example for a bubble domain with trivial topology. **f** Bubble domain with topological charge $Q = 2$, as the magnetization winds twice around 360°. **g** Bubble with topological charge $Q = 1$ but inhomogeneous domain wall chirality.

The homogeneously magnetized film does not carry topological charge ($Q = 0$). The same is true for most domains with domain wall defects. In the example shown in Fig. 2.4e, the in-plane magnetization does not realize a complete 360° rotation along the domain wall, hence no topological charge is present. Specific arrangements of winding sets of vertical Bloch lines can lead to magnetic bubbles with topological charge > 1 (compare, e. g., Fig. 2.4f, where the magnetization performs two full rotations).

In a continuous, micromagnetic picture, it is not possible to transform a magnetic state with one specific topology into another state with a different topological charge by gradually modifying the magnetization texture. At some point, neighboring magnetic moments align antiparallel, which results in a large penalty in exchange energy. The corresponding energy barrier associated with the necessary non-continuous spin flip constitutes the topological energy barrier, sometimes mislabeled as the topological protection of a skyrmion. Also note that the domain wall of a skyrmion does not necessarily need to be homochiral to carry topological charge: The bubble shown in Fig. 2.4g carries a unitary topological charge even though the domain wall chirality varies locally.

2.3.1. The skyrmion stability model

While skyrmions are often associated with DMI, the presence of DMI is not necessarily required to form or stabilize a skyrmion texture in a magnetic thin film. Indeed, skyrmions have been found in ferromagnetic multilayer structures with symmetric interfaces. In these material stacks, interfacial DMI contributions from two identical interfaces on both sides of one magnetic layer cancel each other due to opposite signs of the effect. Hence, in such magnetic multilayer systems, observed skyrmions are predominantly stabilized by stray fields. Even in asymmetrically stacked multilayers with finite DMI, the stabilization of skyrmions is a balance between multiple interactions, with demagnetizing fields always playing a key role. The main effect of strong DMI on the skyrmion is the definition of the domain wall chirality, hence the possible stabilization of a Néel wall.
Even before the rise of magnetic skyrmions, the interplay of energy terms was investigated for the stability of bubble domains [66, 67]. These models were later extended to topological features. Of particular interest here is the work of Büttner et al. [64], who introduced a framework to calculate the stability of a spatially isolated magnetic skyrmion, which allows for the computation of the energy of such a skyrmion with a specified diameter compared to the homogeneously magnetized film.

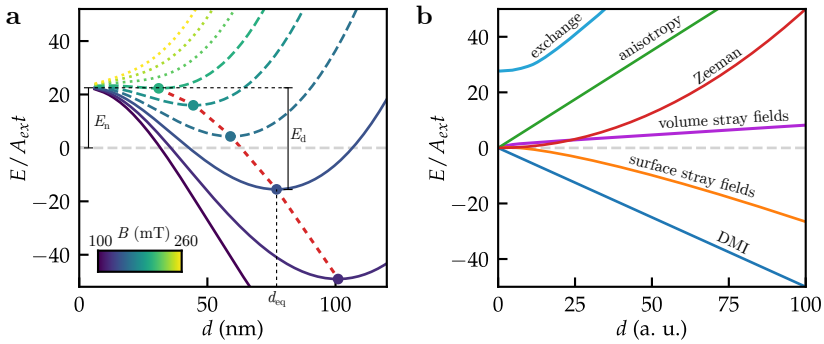

Figure 2.5 | Stability of isolated skyrmions. a The total skyrmion energy depending on the skyrmion radius R for various applied magnetic fields. The (meta-)stable skyrmion radius is marked, as well as the nucleation and decay energy barriers. **b** Individual energy terms contributing to the curves plotted in (a). All curves are qualitative and not to scale with each other. Adapted from [64].

Figure 2.5a depicts the skyrmion energy curves as a function of the skyrmion diameter d for various applied out-of-plane magnetic fields. Note, that the field direction is opposite to the magnetization direction within the skyrmion. This way, the field prevents the skyrmion from deforming from its circular shape and breaking up into a maze domain state. For some field values, the energy curves have a local minimum at a finite diameter, which corresponds to the equilibrium skyrmion size for the chosen set of parameters. If the value of the total energy

at this minimum is negative, the skyrmion is energetically favorable compared to the saturated film and therefore stable (solid lines in Fig. 2.5a). In the case of a positive total energy, the skyrmion state is metastable (dashed lines). If no local minimum exists, no skyrmions can stabilize and any transiently nucleated skyrmion will collapse. These stability considerations assume a continuous, deformation-free contraction of the skyrmion towards $d = 0\,\mathrm{nm}$ and a homogeneous material without domain wall pinning.

Figure 2.5b splits the skyrmion energy into the elementary interaction terms as introduced in section 2.1. With increasing skyrmion diameter d, the total domain wall length increases linearly $\approx 2\pi d$, while the area of inverted out-of-plane magnetization increases with $\approx \pi d^2$. For large skyrmion diameters, the energy is dominated by the Zeeman term from the applied magnetic field. The energy increases with the skyrmion size (hence, d^2), as the skyrmion polarization is antiparallel to the applied field. As the term with the highest order d-dependence, this term leads to the universal energy increase towards infinity, which we see in Fig. 2.5a. Furthermore, with all other parameters fixed, an increase in the applied field pushes the energy minimum, and thus the skyrmion size, towards smaller values of d.

Because the domain wall disrupts the parallel, out-of-plane alignment of the magnetization, each section of the domain wall has an energy cost due to exchange and perpendicular anisotropy. The energy penalty from these terms therefore increases linearly with d. Note that at small skyrmion diameters the exchange deviates from the linear relation and is the only finite contribution at $d = 0\,\mathrm{nm}$. The resulting energy offset only depends on the exchange stiffness A_{ex} of the material and the thickness t of the film, with reported values between $8\pi A_{\mathrm{ex}} t$ [68] and $38 A_{\mathrm{ex}} t$ [69].

Also, the DMI contribution is proportional to the length of the domain wall, as it prefers rotating spin structures, which reduces the domain wall energy accordingly. If DMI is present, however, the domain walls have a Néel component. The induced volume charges along the domain wall (compare section 2.2) introduce a small energy penalty. Finally, the stray field contributes significantly to the stabilization of the skyrmion. It is not straightforward to analytically determine an exact value, but multiple approximations exist. For example, for very large d, the stray field energy follows $-d \log(d)$.

The model allows us to determine two important energy barriers: The nucleation barrier E_{n} is the energy required to nucleate (meta-)stable skyrmions from the homogeneous state (to which $E = 0$ is normalized). Conversely, the decay barrier E_{d} describes the necessary thermal energy for a skyrmion to collapse (compare Fig. 2.5b). In this framework, the creation of a skyrmion involves the nucleation of a topological charge of infinitesimal size $d = 0\,\mathrm{nm}$ and subsequently expanding it to the stable diameter d_{eq}, while decay is the reverse process. The decay

barrier strongly depends on all micromagnetic parameters, as shown for the applied magnetic field. The nucleation barrier is essentially field independent, as it is predominantly determined by the exchange.

2.3.2. Optical skyrmion nucleation

As discussed previously, the transition from a homogeneously magnetized magnetic thin film to a topological skyrmion arrangement involves a significant topological energy barrier that has to be overcome in the skyrmion nucleation process. This exchange-induced threshold has magnitudes on the order of $500 k_{\mathrm{B}} T$ [70], which makes it nearly impossible to adiabatically enter the skyrmion phase, for example, via field cycling (even though the actual energy barrier may be much smaller [71]). Hence, various kinds of external stimuli have been explored to overcome or circumvent the topological barrier to enter the topologically non-trivial skyrmion phase. Upon injecting electric current into an asymmetric magnetic multilayer, the spin-Hall effect leads to the creation of spin-polarized currents within the magnetic material. These spin currents induce a spin-orbit torque, which enables skyrmion nucleation at naturally occurring or artificially created material defects, which act as nucleation sites [70, 72, 73]. Another way to create skyrmions is to heat the magnetic film, either by Joule heating of a magnetic strip [74], multiple consecutive optical laser exposures [75] or direct thermal transfer from patterned heating elements [76]. These experiments, however, mostly report on the creation of skyrmions by breaking up existing stripe domain states into small circular bubbles, instead of starting with a homogeneous state.

As technically another way of heating, skyrmions can be nucleated by exposing a magnetic film with a single intense, femtosecond-short laser pulse. This nucleation method is the fastest known way to nucleate skyrmions in magnetic multilayers and significantly faster than conventional thermally induced domain creation in the same material class [70, 77]. However, experimentally following the skyrmion creation process is challenging and – so far – only few time-resolved investigations have been reported [70, 78, 79]. These experiments use scattering and space-averaging techniques and thus no time-resolved real-space imaging of the nucleation process exists. Therefore, the interpretation of experimental results primarily relies on simulations, mainly atomistic spin dynamics (ASD) and micromagnetic simulations, which are tuned to match the experimentally recorded data.

In consequence, the transient dynamics during the transition from the topologically trivial to the skyrmion state are still under debate. Zhang et al. found that, as their perpendicular anisotropy is reduced at high sample temperatures, HoCo films transiently enter an in-plane state during laser exposure. In the following cooling process, skyrmions can form in the spin-reorientation transition back to an out-of-plane state [79]. Parrapurath et al. observed in ASD-simulations of GdFeCo that heating above the Curie temperature – hence, entering the paramagnetic state

– is required to form skyrmions [80]. In contrast, Büttner et al. found that in ferromagnetic multilayers it is not required to enter the paramagnetic state to form skyrmions [70]. Instead, they found the footprint of a distinct high-temperature transient phase, which is characterized by a severe reduction of long-range order and exchange between individual magnetic layers as well as spatial and temporal fluctuations of the magnetic order, while preserving short-range magnetic exchange. Their findings are a particularly important foundation for our investigation in chapter 6 and are therefore briefly summarized in the following.

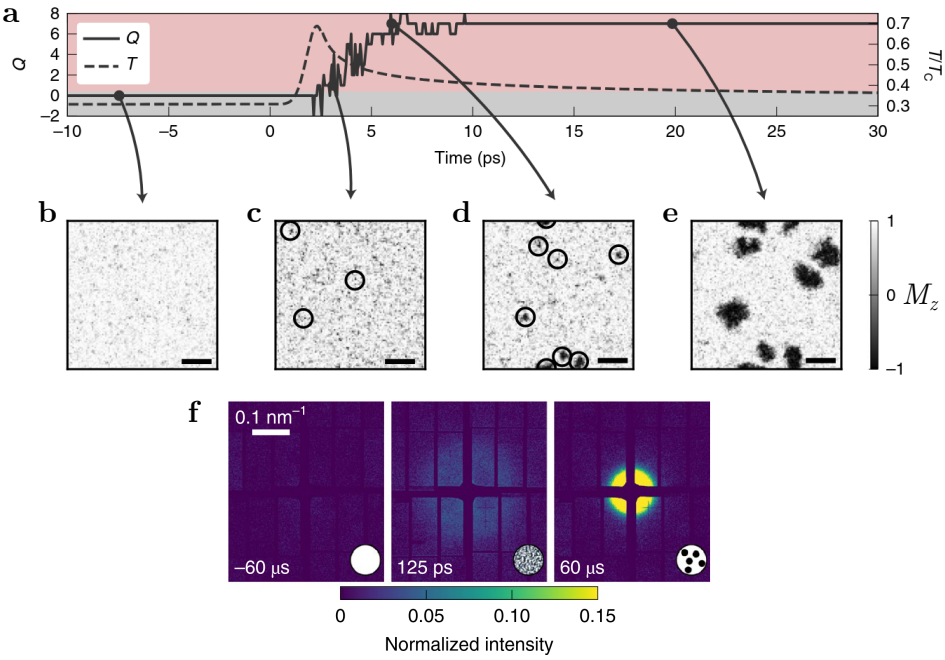

Figure 2.6 | Skyrmion nucleation after optical excitation. **a** Evolution of the integrated topological charge computed via ASD-simulation. **b-e** Snapshots of the time evolution of the out-of-plane magnetization M_z. **f** Respective experimental x-ray scattering pattern. The intermediate fluctuating phase corresponds to homogeneous scattering up to high q. Adapted with permission from [70].

The optical skyrmion nucleation process in ferromagnetic Co/Pt was experimentally studied by small angle x-ray scattering (see section 3.2.2 for a methodological description) and modeled with an ASD-simulation (compare Fig. 2.6). Approximately 100 ps after the laser excitation, the initially homogeneously magnetized sample enters the transient fluctuation phase. In this phase, short-range exchange is still present, but long-range order is suppressed. This breakdown of long-range exchange together with the discrete spacing of individual magnetic spins greatly reduces the required energy to discontinuously flip the magnetic moments to create a local topological charge. This energy barrier can be overcome by the thermal energy in the sample. In consequence, topological skyrmion cores stochastically

nucleate and annihilate (Fig. 2.6b-2.6d), which leads to a rapid increase in the integrated topological charge (Fig. 2.6a). Once the sample cools down and exits the fluctuation phase, long-range exchange is established again and no skyrmion nuclei are created or collapse. Instead, the skyrmions grow by interaction with thermal magnons that coalesce with the nuclei [81] (Fig. 2.6e). While the duration of the creation process of topological charges should be influenced by the temporal temperature profile – and thus the heat-dissipation properties of the sample – it could be determined experimentally that the nucleation of topological charge was finished after as short as 300 ps after initial excitation.

2.4. Ferrimagnetic rare-earth transition-metal alloys

So far, we employed a purely ferromagnetic picture to describe the magnetization textures in our magnetic systems. Hence, neighboring magnetic moments prefer parallel alignment. Ferrimagnetic materials consist of two chemically different ferromagnetic sublattices that each are comprised of one or multiple elements. These two sublattices are antiferromagnetically exchange coupled, hence, their respective magnetic moments have antiparallel alignment. As such, these ferrimagnetic materials combine ferro- and antiferromagnetic properties, which gives rise to phenomena that cannot be found in ferromagnetic samples.

One material class that is of elevated importance for this thesis are rare-earth transition-metal alloys, specifically gadolinium iron (GdFe) and dysprosium cobalt (DyCo) thin films. Here, the rare-earth (RE) and the transition-metal (TM) sublattices couple in an antiferromagnetic manner. The net magnetization of the material is the difference between the two sublattice magnetizations, M_{RE} and M_{TM}. If both contributions are equal, the material is compensated and does not exhibit any net magnetization, comparable to an antiferromagnet [31].

Figure 2.7 shows the temperature dependence of the two antiparallel magnetization contributions of the sublattices as well as the absolute net magnetization in a typical GdCo thin film. Due to the exchange coupling between both elements, they share an ordering temperature T_{C} between the Curie-temperatures of both pure materials. Because the temperature dependence of the two sublattice magnetizations has different slopes, the net magnetization also changes with temperature and reaches compensation at one specific (magnetization) compensation temperature T_{M}. The compensation temperature of a RE-TM alloy uniquely identifies its stoichiometry. Note that, depending on the material composition, full compensation may not be possible between 0 K and T_{C}, e. g., if the TM-concentration is so high that the transition metal sublattice already dominates at $T = 0\,\mathrm{K}$ [82].

When approaching T_{M}, the net magnetic moment gradually reduces. In consequence, the Zeeman energy term, which is proportional to the local magnetization, weakens. The necessary field strength to change the magnetization orientation

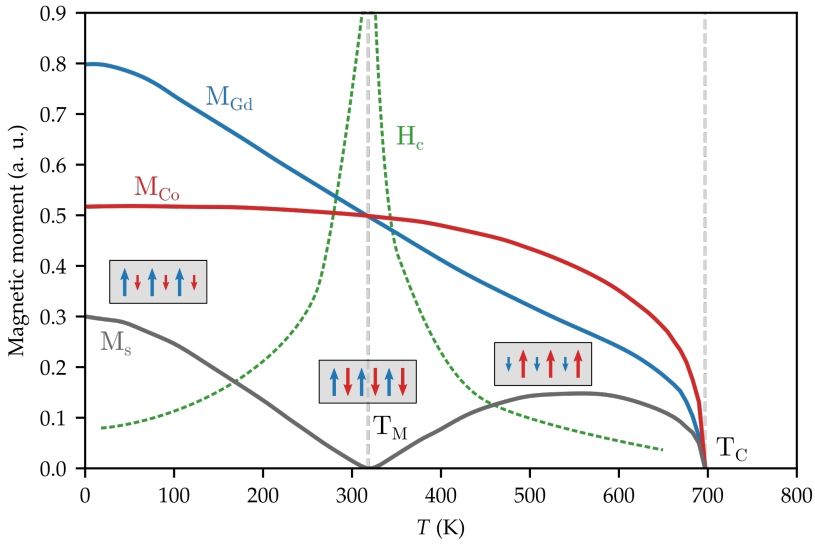

Figure 2.7 | Temperature dependent behavior of a ferrimagnetic alloy. Magnetic moments M_{Co} and M_{Gd} of the Co and Gd sublattice in a GdCo alloy versus the ambient temperature up to the ordering temperature T_C. The resulting total saturation magnetization M_s is the difference of the two sublattice contributions. The coercive field curve is a representative approximation of the behavior close to the compensation point T_M. Magnetization data adapted from [31].

increases inversely. Therefore, the coercive field diverges at the compensation temperature and measuring the divergence of H_c is a particularly sensitive method to determine T_M. This simplified model, however, describes the ideal case of a homogeneous, defect-free RE-TM alloy. In real experiments, however, growth-induced imperfections and inhomogeneities lead to modifications in the magnetic behavior [8, 9, 83]. These inhomogeneities as well as the resulting complex hysteresis loops are discussed in detail in sections 4.2 and A.1.

2.4.1. Helicity-independent all-optical switching

One of the most intriguing phenomena observed in ferrimagnetic rare-earth transition-metal alloys is helicity-independent all-optical switching (HI-AOS). This process describes the coherent inversion of the out-of-plane magnetization direction in response to irradiation by a laser pulse. HI-AOS has attracted significant interest, particularly for high-speed data storage and spintronics applications, due to its ability to switch magnetization on a picosecond timescale without the need for an external magnetic field [84].

Since its initial discovery in 2007 [85] – where circularly polarized light was used to switch the magnetization of a GdFeCo film – subsequent studies have demonstrated that laser pulses of arbitrary polarization can induce switching, provided they are short (on the order of femtoseconds to a few picoseconds [86]) and deposit

a suitable amount of thermal energy [87]. Recent findings have even reported successful switching after heating with picosecond electric pulses [88], reinforcing the understanding that HI-AOS is fundamentally a thermally driven process.

HI-AOS has been observed in a variety of ferrimagnetic materials, including Gd-containing and Gd-doped RE-TM alloys, ferrimagnetic RE-TM multilayers [89–91], and Heusler half-metal Mn_2Ru_xGa [92]. Investigations using MOKE and XMCD techniques [93], along with theoretical treatments through atomistic simulations [29] and micromagnetic models [94, 95], have provided a general framework for understanding the switching process.

The magnetization switching process critically depends on the temporal evolution of the sample temperature following laser excitation as well as the structure and composition of the ferrimagnetic material. These factors dictate the coupling and angular momentum transfer between the sublattices and their interaction with the non-magnetic electron and phonon system. The switching dynamics can be broadly divided into three distinct regimes [96]:

Immediately after laser excitation, the sample is rapidly heated above its Curie temperature T_C, as indicated in Figure 2.8a (marked in red). At this stage, the exchange coupling between the RE and TM sublattices is lifted, and each sublattice undergoes demagnetization at its own intrinsic rate. Notably, the Gd sublattice demagnetizes significantly more slowly than the transition metal sublattice due to its much larger magnetic moment (7.6 μ_{Bohr} for Gd, compared to, e. g., 1.92 μ_{Bohr} for Fe [96]). While the transition metal sublattice can become completely demagnetized on this timescale, the temperature drops below T_C before the Gd system fully demagnetizes, allowing exchange coupling to reestablish.

As the sample cools but remains at an elevated temperature, angular momentum is transferred from the Gd sublattice to the transition metal sublattice. Due to angular momentum conservation, a reduction in Gd magnetization leads to an increase in transition metal magnetization in the same direction, forming a transient ferromagnetic-like state in which both sublattices are aligned parallel—contrary to their equilibrium antiferromagnetic order [93]. In this phase, momentum transfer between the two magnetic sublattices dominates over dissipation into the phonon system.

The tendency of angular momentum to transfer from Gd to the transition metal can be understood by examining the temperature-dependent magnetization curves (Figure 2.7). As the temperature rises, the equilibrium magnetization of the transition metal sublattice decreases more slowly than that of the rare-earth element, leading to an increasing magnetization ratio in favor of the transition metal. The momentum transfer continues until the magnetization of both sublattices is inverted in relation to the initial state.

As the switched magnetization stabilizes, the reestablished antiferromagnetic coupling between the sublattices drives the system toward its new equilibrium configu-

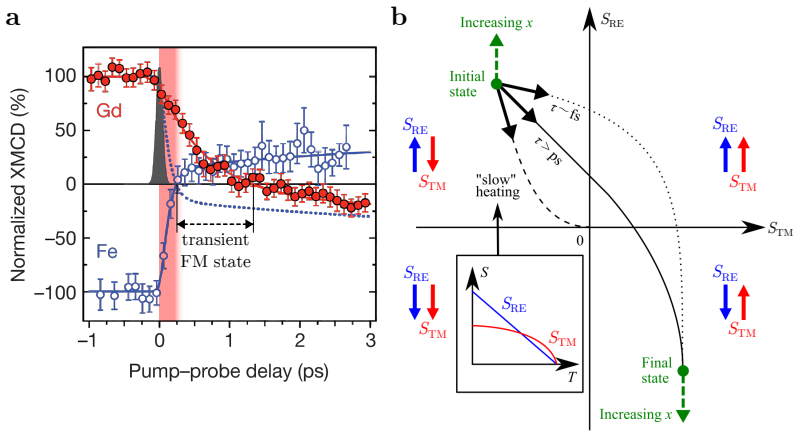

Figure 2.8 | Helicity-independent all-optical switching dynamics in a RE-TM alloy. a Time evolution of the Gd and Fe sublattices in a GdFeCo sample after excitation with a single fs-short laser pulse. The plots show the XMCD-signal (which is proportional to the out-of-plane magnetization) of the two elements. The pulse profile, the relativistic regime, and the transient ferromagnetic state are indicated. Adapted with permission from [93]. **b** Trajectories of a two-component system during HI-AOS for various pulse lengths. S_{RE} and S_{TM} correspond to the angular momentum of the rare-earth and transition-metal sublattice, respectively. The dashed line corresponds to thermal demagnetization according to the inset. Dotted and solid lines represent full magnetization switching with and without an initial decoupled demagnetization phase, respectively. Reproduced with permission from [95].

ration. In this final phase, angular momentum dissipation into the surrounding environment plays a dominant role in determining the final magnetic state [96].

The dominance of either the initial demagnetization or the intersublattice momentum transfer in driving HI-AOS depends on the material properties and excitation parameters. Figure 2.8b illustrates the trajectories of sublattice magnetization in a GdFe alloy in response to heat pulses of varying durations. Slow, adiabatic heating (dashed line) allows the sample to remain in equilibrium, following the magnetization curves of Figure 2.7, ultimately leading to full demagnetization above T_C [95]. In contrast, rapid heating via a femtosecond pulse (dotted line) results in ultrafast demagnetization of the transition metal sublattice, followed by relaxation into the switched state. The solid trajectory in Figure 2.8b represents a scenario where strong interlattice momentum transfer enables switching even after relatively slow picosecond pulses, allowing angular momentum to be directly transferred from Gd to Fe while maintaining angular momentum conservation [95].

Note that these considerations mostly operate in macro-spin picture. In such a model, the magnetization is considered as spatially homogeneous. Additionally, only longitudinal dynamics are considered, as the transversal dynamics are expected to only come into play at large time scales during the final phase of the switching process. Lateral dynamics cannot be ignored, however, as Graves et al. found that lateral chemical inhomogeneities lead to lateral angular momentum transfer on the

nanometer scale [8]. Recent studies further underline the inhomogeneous nature of the switching dynamics in RE-TM materials [81, 97].

Chapter 3
Experimental techniques

The primary results presented in the experimental chapters have been obtained using imaging, scattering, and spectroscopy techniques that rely on soft x-ray radiation. Consequently, most experiments were conducted at synchrotron and x-ray free-electron laser (XFEL) facilities. This chapter therefore aims to introduce the general working principles of the employed methods.
We begin with an introduction into the origin of the contrast mechanisms in the form of magnetic circular and linear dichroism effects. This is followed by a general overview of the working principles of each utilized x-ray radiation-based technique, including scanning transmission x-ray microscopy, small angle x-ray scattering, and Fourier transform holography. Details regarding specific experimental setups, as well as the data acquisition and processing workflows, are provided in the respective chapters.
In addition to x-ray-based methods, the experiments were complemented by a variety of laboratory-based imaging and bulk characterization techniques. These include magnetic force microscopy (MFM), L-TEM, STEM, and Kerr-microscopy for imaging and SQUID, laser-MOKE, and Hall transport measurements for bulk magnetometry characterizations. Details about these techniques are provided in section 3.3 of this chapter and in the relevant topical chapters, where they support the presented findings.

3.1. Accessing magnetic features with x-rays

The interaction of photons with matter is fundamental for a majority of experimental techniques in the research of solid-state magnetism. Visible light is widely used in microscopy, spectroscopy, and scattering experiments. However, as samples become more complex and the investigated textures shrink towards smaller feature sizes, the limits of such optical techniques become apparent. The absolute resolution-limit of a microscope is given by the Abbe diffraction limit, which determines the minimum resolvable distance d_{min} between two features as

$$d_{\mathrm{min}} = \frac{\lambda}{2\mathrm{NA}}, \tag{3.1}$$

where λ is the optical wavelength and $\mathrm{NA} = n\sin(\theta)$ is the numerical aperture of the microscope setup [98, 99]. In consequence, even the best immersion microscope with an (practically impossible) optical half-opening angle of $\theta = 90°$ and an immersion oil with refractive index $n = 1.45$, using violet light ($\lambda = 400\,\mathrm{nm}$), can at best expect a resolution of approximately 70 nm. Even though resolutions beyond the diffraction limit have been demonstrated, the involved methods are highly complicated and in practice, resolutions beyond 200 nm are immensely challenging [100, 101]. In this thesis, however, we need to resolve magnetic features as small as 30 nm, hence, one order of magnitude smaller.

The transition from visible light (400-700 nm) to the soft x-ray regime (0.4-2 keV, corresponding to 0.6 - 3 nm) offers two major advantages: First, the smaller wavelength results in a significant improvement of the (theoretically) achievable resolution, proportional to the reduction in wavelength. Second, while visible light primarily interacts with electronic states in the valence band, the increased photon energy of x-rays also allows us to excite the inner, localized electron states [102]. The resulting absorption edges allow for element-specific probing of materials and give access to versatile magnetic contrast mechanisms in the form of x-ray magnetic circular dichroism (XMCD) and x-ray magnetic linear dichroism (XMLD). These two dichroism effects are key for magnetic imaging with x-rays. Despite these advantages, the use of soft x-rays introduces specific challenges that one must take into consideration when designing experiments [103].

First, aside from material specific resonant conditions, the real part of the refractive index of x-rays in matter is close to unity. Additionally, the penetration depth in most materials is limited to a few hundred nanometers [104]. In consequence, efficient high-power refractive x-ray optics do not exist, which inhibits the construction of refractive imaging systems. Therefore, alternative, less conventional imaging techniques using diffraction or reflection must be used. We used two of these methods in this work, namely scanning transmission x-ray microscopy (STXM), which uses a Fresnel zone plate as a diffractive focusing optic [105], and Fourier transform holography (FTH), which entirely eliminates the need for focusing elements in the experiment chamber. When imaging is impractical, pure x-ray scattering techniques can provide valuable insights into magnetic phenomena on the nanometer scale.

Second, magnetic imaging with soft x-rays imposes strict requirements on the light source. The x-rays must be monochromatic, coherent, and usually polarized, with controllable polarization being crucial for many techniques. These requirements are fulfilled at undulator-equipped beamlines at synchrotron and x-ray free-electron laser (XFEL) facilities, which also deliver the high photon flux necessary for achieving reasonable integration times. Additionally, the short x-ray pulses produced by these sources enable time-resolved experiments with temporal resolutions on the picosecond (synchrotron) and femtosecond (XFEL) scales.

In the following sections, we first introduce the origins of XMCD and XMLD contrast, which the entirety of our x-ray-based research relies on. Afterwards, we discuss the deployed x-ray imaging techniques, STXM and FTH, as well as small-angle x-ray scattering.

3.1.1. Resonant x-ray absorption

Absorption-based imaging techniques measure the spatially varying attenuation of x-rays through a material. The exponential decay of the x-ray transmission intensity I for a homogeneous film of thickness d is given by the Beer-Lambert law

$$I(d) = I_0 e^{-\mu d}. \tag{3.2}$$

Here, μ is the energy dependent, material specific absorption coefficient [106]. In the soft x-ray regime, absorption processes are dominated by photoelectric excitations. Generally, μ decreases with increasing photon energy, roughly following a $\frac{1}{E^3}$-relation [106].

Exceptions to this rule are material specific absorption edges. Here, the photon energy matches the required energy to excite an electron from a strongly bound core level into an unoccupied state in the valence band. Because of the Pauli-exclusion principle, the excited electron must be elevated above the Fermi energy E_F. The X-ray absorption spectrum (XAS) is therefore a probe of the number of excitable electrons in the core state and the unoccupied density of states (DOS) above E_F. The fact that localized core electron states are excited gives the XAS its element specificity: The higher the atomic number, the stronger electrons in a particular state are bound and the excitation energy for a specific transition increases accordingly.

Relevant for this work are the L_3 edge of the transition metal cobalt as well as the M_5 edges of the rare-earth elements gadolinium and dysprosium, which are shown in Fig. 3.1. They correspond to the excitation of electrons from the $2p_{3/2}$-level into empty $3d$-states and from the $3d_{5/2}$-states into the valence $4f$-band, respectively [107].

The existence of multiple absorption edges in a close energy range is caused by spin-orbit splitting of the core states. Exemplary, the L_2 and L_3 edges in a $3d$-metal like cobalt stem from the $j = l + s$ and $j = l - s$ spin orbit coupling, which results in two levels $2p_{1/2}$ and $2p_{3/2}$, roughly 15 eV apart [107]. Because the electronic occupation of the $2p_{3/2}$-state is twice as high as the occupation of the $2p_{1/2}$ state, the photon absorption at the corresponding edge is doubled as well. The spin-orbit splitting of the core states is also of fundamental importance for the dichroism effects.

In resonant x-ray absorption spectroscopy, the imaginary part β of the complex refractive index $n = \delta + i\beta$ of the material is probed. Exactly on resonance, the

contribution of the transition to the refractive index is purely imaginary, hence, only the absorption is affected. Nevertheless, away from the absorption maximum, the real part δ of the refractive index is finite and can be estimated from the absorption spectrum via the Kramers-Kronig relations [108]. Indeed, even many electronvolts away from the absorption edge, the real part can still be considerable [109] and lead to a finite phase contribution down to vanishing photon energy. Because the real part imprints a phase shift on the propagating photons, it can be probed by phase-sensitive techniques, such as holography and ptychography [110]. With one exception, x-ray experiments performed in this thesis were either not phase sensitive and only measured the photon absorption or were performed on the resonance energy. We therefore simplify the discussion of contrast mechanisms by only considering contrast that arises from differences in the x-ray absorption.

3.1.2. X-ray magnetic circular dichroism

XMCD describes the phenomenon that the resonant absorption of circular polarized x-rays varies depending on the alignment of the magnetization of the sample with the angular momentum of the photon. The effect was first theoretically described in 1975 [111] and experimentally observed in 1987 [23] at the Fe K-edge. Much larger dichroism effects are observable in the soft x-ray regime at the L and M edges of rare earth elements and transition metals.

We explain the XMCD-effect for a magnetic transition metal, e. g., cobalt. Figure 3.1a shows the spin resolved electronic configuration of the orbitals in a ferromagnetic $3d$-metal that are responsible for the emergence of XMCD. The spin-up and spin-down $3d$-valence bands are shifted with respect to each other, due to Stoner-splitting [32]. As a result, the occupation of up- and down-states is different. This causes the existence of a spin-majority, hence a non-zero magnetic moment. Importantly, the minority band has more electron-holes, respectively non-occupied electron states. While the $4s$-states also contribute to the DOS at the Fermi energy, they are essentially homogeneously distributed over a wide energy range and can therefore be ignored when considering the spin asymmetry of the DOS.

The $2p$-orbitals are split into two distinct energy levels, $2p_{1/2}$ and $2p_{3/2}$, due to spin-orbit coupling. A circular polarized photon with matching energy can excite an electron from a $2p$-orbital into the valence band. In this process, dipole selection rules mandate that the orbital moment quantum number of the excited electron needs to change by $\Delta m_l = \pm 1$ (as the electron absorbs the orbital momentum of the photon), while the electron spin is conserved ($\Delta m_s = 0$) [106]. Thus, a $2p$-electron with spin $s = +1/2$ can only be excited into an empty spin $s = +1/2$ state.

During the excitation process, the photon couples to the orbital momentum of the electron. The spin-orbit coupling of orbital momentum and spin in the $2p$-

states leads to a difference in the photonic excitation probability of a spin-up or spin-down electron, depending on the total angular momentum of the $2p$-state and the circular polarization of the photon. The circular polarization or "helicity" of the photon is either left- (σ^-) or right-handed (σ^+). The excitation probabilities and resulting electron spin polarizations are shown in Tab. 3.1b for a σ^+-polarized photon [106]. For σ^--polarization, all probabilities and polarizations are flipped. Note that these values assume empty valence states (or at least equally empty bands, hence no Stoner splitting). The key observation is that circular polarized x-rays excite electrons from a spin-orbit-split $2p$-orbital with a bias towards one specific electron-spin polarization.

Due to the Stoner-splitting, the valence $3d$-bands offer more possible final states above the DOS for electrons with minority spin-polarization. The transition probability increases accordingly, compared to an electron with majority spin-polarization. Hence, in the state presented in Fig. 3.1a, a spin-up electron is more readily excited than a spin-down electron. Therefore, a σ^+-photon is more likely to excite an electron from the $2p_{3/2}$ states into the valence band than a σ^--photon. The photon-absorption in the material scales accordingly, which results in the circular dichroism. Note that the sign of the dichroism is opposite for the transitions $2p_{1/2} \rightarrow 3d$ and $2p_{3/2} \rightarrow 3d$. The identical dichroism effect can either be measured by changing the photon polarization or by inverting the direction of the magnetic moment.

The experimentally determined XMCD absorption spectrum for the L_2 and L_3 edges of cobalt is shown in Fig. 3.1c. As predicted, the sign of the dichroism at the two absorption edges is inverted, as they correspond to excitations from core states with opposite orbital momentum. Figure 3.1d shows the XMCD at the M_5 edge of dysprosium. The circular dichroism is large with up to 50 % of the peak resonant absorption and therefore allows for high imaging contrast.

If the spin quantization axis and light polarization are not collinear, the absorption probability of a photon by a minority or majority electron scales with the geometrical projection. Hence, the XMCD-induced absorption is sensitive to the direction of the magnetic moment $\mathbf{m}$ with respect to the angular momentum direction of the photon $\mathbf{L}_{\mathrm{ph}}$, which can be generalized to

$$I_{\mathrm{XMCD}} \propto \mathbf{m} \cdot \mathbf{L}_{\mathrm{ph}} \propto \cos(\theta), \tag{3.3}$$

for arbitrary angles θ between $\mathbf{m}$ and $\mathbf{L}_{\mathrm{ph}}$ [102]. In practical terms, $\mathbf{L}_{\mathrm{ph}}$ points along the axis of photon propagation and XMCD is therefore sensitive to the magnetization component along the photon propagation direction. Most thin-film transmission experiments probe the sample in a normal incidence geometry, in which XMCD probes the out-of-plane magnetization component. This is particularly useful for imaging magnetic domains in magnetic thin films with perpendicular

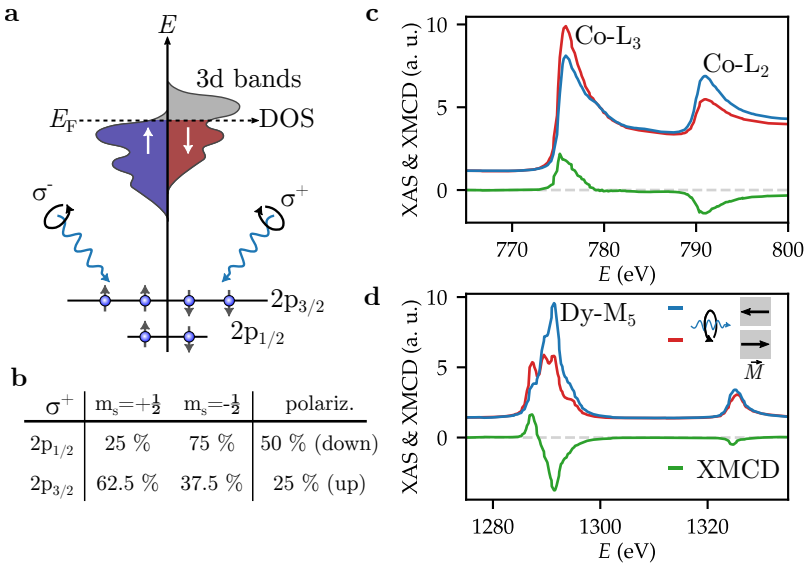

σ^+	$m_s=+\frac{1}{2}$	$m_s=-\frac{1}{2}$	polariz.
$2p_{1/2}$	25 %	75 %	50 % (down)
$2p_{3/2}$	62.5 %	37.5 %	25 % (up)

Figure 3.1 | Origin of x-ray magnetic circular dichroism. **a** Spin-resolved density of states for the 2p and 3d bands in a 3d-metal. **b** Excitation probabilities for photoelectrons excited by a right-handed circular polarized photon. **c** XAS and XMCD spectrum of the L_2 and L_3 edges of Co. **d** XAS and XMCD spectrum of the M_5 and M_4 absorption edges of Dy. Absorption data was acquired by transmission spectroscopy at the VEKMAG endstation at BESSY.

anisotropy. Non-normal incidence setups additionally allow probing components of the in-plane magnetization. In general, XMCD can be used to probe ferromagnets and ferrimagnets, hence, materials that exhibit a finite element-specific magnetic moment. This is particularly interesting for probing compensated ferrimagnets, as the dichroism contrast does not depend on the net magnetization but has selective sensitivity to a single element.

3.1.3. X-ray magnetic linear dichroism

XMLD is a complementary dichroism effect that was postulated [112] and experimentally confirmed [113] around the same time as XMCD. It describes an angular dependence in the absorption spectra of linear polarized photons in the presence of a magnetic moment. The XMLD arises from a charge anisotropy induced by axial spin alignment, mediated by spin-orbit coupling [102]. Here, the electric field of the photon acts as a "search light" that probes the spatial distribution of valence band holes in alignment with the polarization axis **E** of the x-rays [24].
At an absorption edge without linear dichroism, the charge distributions of all energetically degenerate valence orbitals sum up to an isotropic spherical charge distribution. Hence, the excitation probability of electrons from a core state to a valence state does not depend on the polarization direction of the photon. If, however, the energy levels of individual orbitals are split, e. g., by spin-orbit

coupling or multiplet-splitting, certain photon energies may become sensitive to non-isotropic orbitals in which the electron occupation depends on the direction of bonding orbitals (x-ray natural linear dichroism, XNLD) or the magnetic moment (x-ray magnetic linear dichroism, XMLD).

XMLD is particularly strong in materials that exhibit well-defined multiplet splitting, which increases the distance between energy levels of individual orbitals. One example for materials exhibiting such strong XMLD are transition-metal oxides [102]. In pure 3d-metals, however, the XMLD effect is weak: The strength of the XMLD signal at the $L_{2,3}$ edges is roughly 5 % of the XMCD signal [114] due to weak spin-orbit coupling and a large bandwidth [115]. Furthermore, transitions from individual multiplets of the same spin-orbit split core state (e. g., the $2p_{1/2}$ state in Fe) can contribute to the XMLD signal with opposite sign.

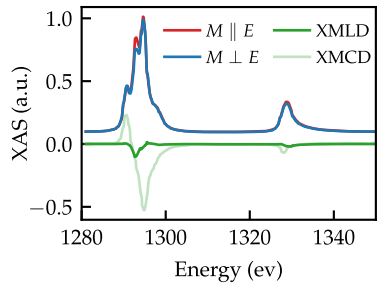

Figure 3.2 | XAS and XMLD in DyCo a the Dy M_5 edge. The XMCD spectrum is shown for comparison. Measured at VEKMAG/BESSY-II.

In comparison, the M_5-edges of the rare earth elements exhibit much more structure within their absorption spectra [116]. Exemplary, in Dysprosium individual absorption peaks are separated by approximately 2 eV. Accordingly, the XMLD effect is expected to be much larger than in transition metals. Indeed, Luo et al. measured a noticable amount of XMLD signal in a narrow energy band at the rare-earth M_5-edge of Dy [83].

Figure 3.2 shows the XMLD spectrum of one of our DyCo alloys at the Dy M_5-edge. Note that the effect is still significantly smaller than the XMCD effect at the same edge shown in Fig. 3.1d. The three peaks of the M_5 edge correspond to different transitions where the magnetic moment of the involved $4f$-orbital is (in order of increasing energy) antiparallel, transversal, or parallel oriented with respect to the x-ray propagation direction [117]. Unsurprisingly, the XMLD effect appears on the peak corresponding to the transversal direction.

In practical terms, the XMLD-intensity depends on the alignment of the magnetization with the polarization axis $\mathbf{E}$ of the photon according to [102]

$$I_{\mathrm{XMLD}} \propto |\mathbf{m} \cdot \mathbf{E}|^2 \propto \cos^2(\theta). \tag{3.4}$$

In normal-incidence on a thin-film, the electric field direction of the x-rays lies in the plane. Therefore, the XMLD absorption probes the axial alignment of the in-plane magnetization with the polarization. Because XMLD is only sensitive to the magnetization axis, it is also uniquely suited to probe natural antiferromagnets.

3.2. Synchrotron radiation-based techniques

3.2.1. Scanning x-ray transmission microscopy

In a scanning transmission x-ray microscope STXM, the light is focused on a small spot on the sample to determine the local x-ray attenuation [118]. By scanning the sample position and by exploiting XMCD and XMLD, the map of transmission versus position is recorded, which results in an image showing magnetic contrast. By recording the same field of view with positive and negative circular polarized photons (or two orthogonal linear polarizations), purely magnetic contrast can be extracted by calculating the difference or ratio of the two images.

Figure 3.3 depicts the experimental geometry of the imaging system. The polarized and monochromatized photons are focused by a Fresnel zone plate, which uses diffraction to focus the x-rays on a spot of few tens of nanometers. Because the zone plate essentially acts as a diffraction grating, multiple orders of diffraction exist behind the sample. Besides the focused first order beam, the 0th order direct transmission and higher order diverging beams are undesirable and need to be blocked by an order-selecting aperture (OSA). The sample itself is positioned exactly in the focal plane to minimize the area of material that is probed and therefore maximize the spatial resolution. Behind the sample, a photodetector measures the transmission through the measured film. The sample stage is moved by piezo-electric scanners with nanometer precision.

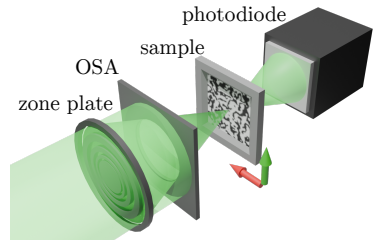

Figure 3.3 | Schematic of a typical STXM setup, including the Fresnel zone plate, order-selecting aperture, sample on xy-scanner stage and photodetector.

STXM images presented in this thesis were acquired with the MAXYMUS-instrument at BESSY-II [119]. The beamline supplies photon energies at all relevant absorption edges (transition-metal L_3- and rare-earth M_5-edges). The undulator can be tuned to supply circular polarized photons of positive or negative helicity as well as horizontal and vertical linear polarized light. The microscope setup is equipped with a He-cryostat and the ability to apply magnetic fields of up to 250 mT. A fiber laser allows for the in-situ optical excitation of samples with pulse lengths below 1 ps. Furthermore, it is possible to mount the sample rotated by 30° in the plane, which allows for non-normal incidence measurements. [120]

The main advantage of the STXM setup lies in its straight-forward manner to acquire images. The recorded data is immediately interpretable without the need for complex processing. The recording of large sample areas is possible, and one can freely choose the desired field of view, as long as the magnetic material is deposited on a large x-ray-transparent membrane. Additionally, STXM is a quantitative

technique: The total amount of transmitted photons is recorded, which allows precise determination of the local magnetic polarization of the sample. Potential downsides of the technique include the achievable spatial resolution of about 20 nm, which is given by the numeric aperture of the zone plate and mechanical vibrations, and the necessity to regularly realign the sample laterally and in the focus due to thermal drift. Finally, the distances between zone plate, OSA, sample and detector are small ($< 1\,\mathrm{mm}$), which restricts sample sizes and geometries and makes the integration of sample environments and actuators challenging (for example, strong electromagnets or azimuthal sample rotation stages).

3.2.2. Small-angle x-ray scattering

Small-angle x-ray scattering (SAXS) is an experimental characterization technique that uses elastic scattering of x-rays to probe structural, topographic, and magnetic correlations in materials [104, 121]. The prototypical transmission-based SAXS setup, as depicted in Fig. 3.4a, involves an x-ray beam passing through a semi-transparent sample. For sufficient x-ray transmission, the sample must be a thin film or lamella, either freestanding or deposited on an x-ray transparent substrate. The scattered x-rays are recorded by a pixel detector, typically an in-vacuum CCD or CMOS camera, while a beamstop is positioned to block the high-intensity, directly transmitted 0th-order light to prevent saturation or damage to the detector. In elastic scattering, the wave vector magnitudes of the incoming (k_i) and outgoing (k_f) x-rays are identical. Angular deflections (2θ) correspond to a momentum transfer $q = 2k\sin(\theta)$ (with $q = |\mathbf{q}|$, compare Fig. 3.4b). For a thin, homogeneous sample, the incident wave function $\Psi_0(x,y)$ is modulated by the material's transmission function $T(x,y)$, resulting in an exit wave $\Psi_{\mathrm{exit}}(x,y) = T(x,y)\Psi_0(x,y)$. The transmission function T has contributions from both topographic variations (T_c) due to material density, thickness, or composition, and magnetic texture (T_m) arising from magnetic contrast mechanisms. Thus, $T = T_c \cdot T_m$ [104].
According to the Fraunhofer approximation, the scattered wave front in the far field represents the Fourier transform of the exit wave. Assuming an incident plane wave $\Psi_0(x,y) = |\Psi_0|$, the scattering pattern on the detector $\Psi_{\mathrm{det}}(x_{\mathrm{det}},y_{\mathrm{det}})$ relates to the real space transmission via

$$\Psi_{\mathrm{det}}(x_{\mathrm{det}},y_{\mathrm{det}}) = \mathcal{F}[\Psi_{\mathrm{exit}}(x,y)](q) = |\Psi_0|\mathcal{F}[T(x,y)](q), \tag{3.5}$$

where $\mathcal{F}$ is the Fourier transform operator [104]. Consequently, the scattering pattern encodes spatial wave vectors corresponding to the modulations in the transmission function. When the scattering pattern is centered on the detector, low-frequency information (corresponding to large features) appears near the center, while high-frequency information is recorded near the frame edges. The largest $\mathbf{q}$ and thereby the smallest detectable spatial feature size is therefore geometrically limited

by the detector size and distance, in combination with the x-ray wavelength. The Fraunhofer approximation assumes full spatial and temporal coherence. However, if the spatial coherence of the x-rays is less than the illuminated sample area, the SAXS signal represents the ensemble average of non-coherently added contributions, suppressing speckle patterns while retaining spatial correlation information common to the entire area.

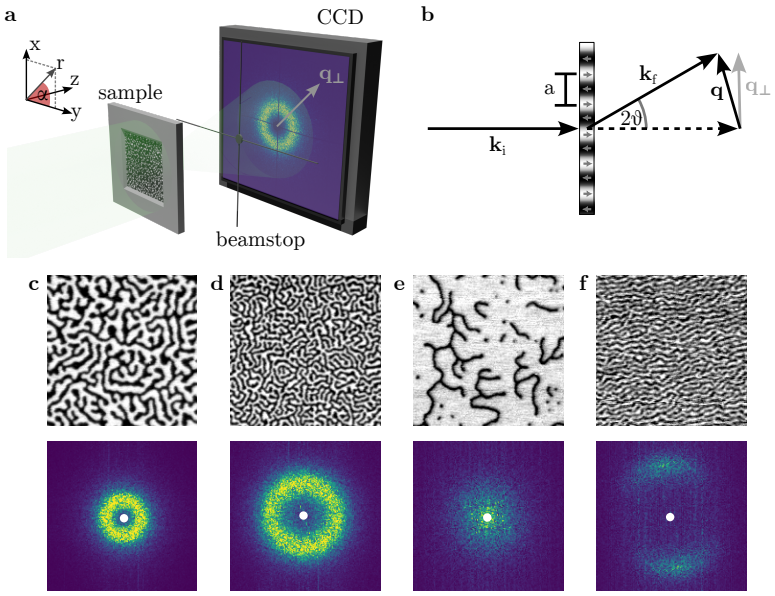

Figure 3.4 | Small angle x-ray scattering geometry. a Sketch of a typical experimental setup. **b** Scattering geometry of a magnetic sample with stripe domains with a spatial period of L. **c-f** Various magnetic domain configurations (top) and their expected SAXS diffraction pattern (bottom). The scattering patterns were calculated from the real space STXM-images.

The magnetic transmission factor T_m is primarily governed by the XMCD effect, which is sensitive to the out-of-plane magnetization. Consequently, magnetic SAXS is particularly effective at probing domain structures in films with perpendicular magnetic anisotropy (PMA), where periodic changes between up and down magnetization create maximum transmission contrast. Notably, circularly polarized x-rays are not mandatory for magnetic SAXS scattering, as linearly polarized or unpolarized light can be expressed as the sum of two circular polarized components with opposite polarization. Even though the XMCD contrast of the two polarizations is inverted, the probed correlations are the same. Both polarizations therefore add constructively in the far-field scattering pattern.

As shown in eq. (3.5), the scattering contains contributions from the non-magnetic charge topography as well as the magnetic texture. To isolate the magnetic scattering signal, the following methods are utilized [104]: By using clean samples with minimal inhomogeneities, defects, and contamination, the charge scattering

contribution is reduced by ensuring $T_c(x,y) = \text{const}$. If topographic features are required for the experiment, e. g., lithography-patterned structures, they can be designed in a way that their scattering occupies different **q**-space regimes than the magnetic scattering, such that these parts can be blocked with a beam stop. Finally, recording and subtracting a scattering image of purely the charge scattering without magnetic contributions, e. g., of a magnetically saturated sample reliably removes remaining topographic scattering contributions [104].

Figures 3.4c-f illustrate how specific magnetic domain patterns in thin films correspond to distinct SAXS patterns. A maze domain state, characterized by worm-like domains, produces ring-like scattering: The uniformity of domain widths gives rise to a specific dominant scattering angle $|\mathbf{q}|$, while the random domain arrangement is reflected in the azimuthal isotropy of the SAXS pattern (Fig. 3.4c). Reducing the domain width shifts the scattering maximum to larger **q**-values (Fig. 3.4d). In cases where magnetic features are sparsely distributed across the sample, the lack of short-range order manifests as diffuse scattering that increases towards $q = 0$ (Fig. 3.4e). Interestingly, an arrangement of closely packed skyrmions produces a ring-like scattering pattern nearly identical to that of a maze domain state (compare, e. g., Fig. 3.4a), highlighting the importance of complementary characterization techniques for definitive structure determination. In contrast, a stripe domain state with preferred alignment yields an anisotropic scattering pattern, as depicted in Fig. 3.4f. If stripe domains have a preferred alignment direction, the SAXS signal reflects this symmetry breaking by predominately scattering in the direction of the magnetization modulation.

While it is not possible to directly access the real space magnetic texture via SAXS, the technique does have certain advantages over imaging techniques. First, because full spatial coherence of the light is not required, the technique still performs well at x-ray sources with limited coherence, which can be the case at synchrotron facilities. Second, it enables the acquisition of XMCD-based magnetic information even at linear or unpolarized light sources, providing greater experimental flexibility. Third, SAXS can probe large sample areas simultaneously, yielding statistical information and improved signal-to-noise ratios that make weak signals detectable. Advanced analysis techniques allow for the extraction of domain properties, such as the domain wall width, from the q-dependence of the SAXS pattern [122, 123].

SAXS is particularly useful for rapidly characterizing static and dynamic domain states, especially in samples with short-range domain order. It also enables investigations of processes inaccessible to direct imaging, either due to experimental limitations or intrinsic properties of the process. A prime example are time-resolved, stroboscopic pump-probe experiments at x-ray free-electron laser (XFEL) facilities, where SAXS can overcome challenges such as limited spatial coherence due to beam jitter and stochastic dynamics on the nanometer scale. By averaging over

many events, SAXS can reveal the overall dynamics, offering a robust approach to studying ultrafast magnetic phenomena.

3.2.3. Fourier transform holography

Fourier Transform Holography (FTH) is a powerful technique for magnetic imaging that overcomes fundamental limitations of conventional x-ray scattering experiments [124, 125]. While the diffraction pattern of a magnetic sample mathematically contains all information about the real space magnetic configuration, common x-ray detectors can only measure the intensity but not the phase of the scattered light. This phase information, however, is crucial for the recovery of real space information. Therefore, while SAXS patterns encode characteristic spatial frequencies and provide insight into certain properties of domain walls, the reconstruction of the real space magnetization configuration is impossible from the recorded intensity alone.

Holographic methods solve this phase problem by encoding the phase information into the recorded diffraction pattern through modulation of the intensity signal originating from the sample by superposition with a known reference wave. In Fourier transform holography [126], the sample and reference wave are spatially separated to facilitate the reconstruction. The experimental setup is virtually identical to SAXS (compare Fig. 3.5a), but the method imposes some additional requirements on the sample. The magnetic film is covered by an opaque absorption mask (in our case a 3.5 µm thick Cr/Au multilayer), into which a holographic mask is milled using focused ion beam lithography. This mask contains a 1-5 µm large object aperture that exposes only a part of the magnetic film and one or more through holes (with a diameter between 20 and 80 nm) serving as reference apertures (compare Fig. 3.5b). The exit wave from the object hole and the reference wave interfere and form the hologram on the detector.

Exemplary holographic diffraction patterns are depicted in Fig. 3.5c for left and right-handed circular x-ray polarizations, respectively. The high frequency modulations represent the interference pattern with the reference waves. In the difference image asymmetries between the two polarizations become evident, which are caused by magnetic domain contrast within the object aperture. Assuming small scattering angles and valid Fraunhofer conditions, the real space information is reconstructed by applying an inverse Fourier transform to the diffraction pattern, yielding a convolution of the exit wave front with itself (Fig. 3.5d). This autocorrelation contains the self-correlations of object and references in its center, while the cross-correlations of object and reference appear at distances corresponding to their real space separation. For an infinitesimally small reference hole, this cross-correlation directly represents the exit wave form of the object, which – assuming XMCD contrast achieved by tuning the photon energy to a suitable x-ray absorption edge – gives an image of the domain structure [125].

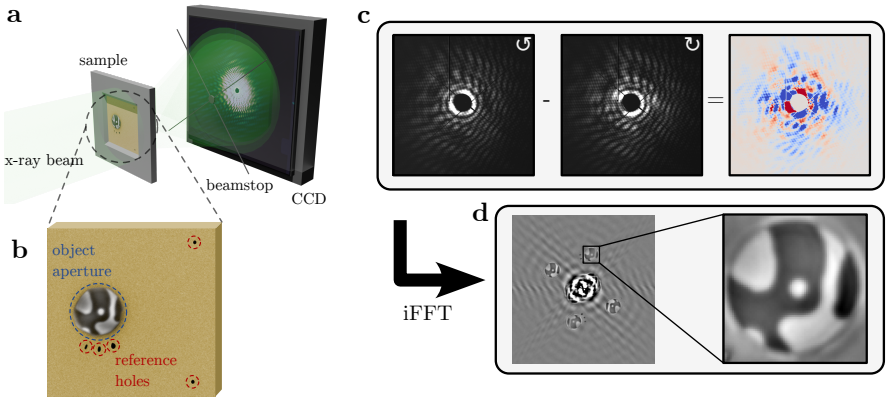

Figure 3.5 | Fourier transform holography of magnetic thin films. a Experimental geometry of a Fourier transform holography setup **b** Example for a holographic mask attached to a magnetic thin film. **c** X-ray scattering patterns of the same sample for left- and right-handed circular polarized light and the difference. **d** Patterson map and enlarged view of an object hole reconstruction.

The design of reference holes requires careful consideration of several factors. They must be positioned far enough from the object to prevent overlap of the reconstruction with the object's autocorrelation but also close enough to maintain spatial coherence between the apertures. The spatial resolution of FTH is primarily limited by the reference hole size, hence, reference apertures should be as small as possible. However, reduced hole diameters result in decreased transmitted intensity and consequently weaker cross-correlation signals. Focal propagation and deconvolution methods can further improve the resolution [127].

Recent developments have combined FTH with phase retrieval algorithms, achieving significant improvements in spatial resolution beyond the reference hole size [25, 26, 128]. Phase retrieval recovers the phase of the scattering pattern by iteratively optimizing the phase data while keeping the recorded intensity in **q**-space and the spatial extent of the sample (the "support") as optimization restraints.

Limitations of FTH include the intricate and time-intensive fabrication of the holographic mask. Moreover, the field of view is restricted to the object aperture, which is typically no larger than a few micrometers in diameter. However, FTH also offers significant advantages: The fixed field of view facilitates observation of the same specific sample area over a long time [129, 130], which can be particularly beneficial for time-resolved experiments. Additionally, because the holographic mask is directly attached to the sample, FTH is highly resistant to sample drift. The technique requires only basic experimental equipment for direct imaging, and the absence of nearby optics allows for versatile sample environments, including strong magnets, cryostats, optical lasers, and conduction lines for electrical excitations.

Table 3.1. | Comparison of the utilized soft x-ray-based techniques.

	Advantages	Disadvantages
STXM	Straight forward image creation Large, unrestricted field of view	Limited spatial resolution Tight sample environment Prone to drift
FTH	High spatial resolution No beam-forming elements required Spacious sample environment Inherently drift-free	Restricted field of view Labor intensive sample preparation Involved image reconstruction
SAXS	Works with arbitrary x-ray polarization Signal accumulation over a large area Easy to implement	No direct real-space imaging

3.2.4. Summary

To summarize, we use a set of x-ray-based techniques due to their element-specific magnetic contrast mechanisms and high-resolution options. Table 3.1 gives an overview of the comparative advantages and disadvantages of the three techniques discussed. Most static imaging experiments were carried out with STXM. This includes domains and domain walls in ferrimagnetic alloys in the chapters 5 and 4, as well as skyrmions and worm domains in Co/Pt multilayers (chapter 6). To push the spatial resolution, coherent imaging was used in chapter 4 to record a detailed image of the domain wall structure. To achieve picosecond temporal resolution, SAXS was used at an X-FEL facility to follow the skyrmion nucleation in chapter 6.

3.3. Auxiliary techniques

Many different techniques aside from x-ray-based methods were deployed to record the data presented in the topical chapters. Parts of the experimental results were supplied by our collaborators, and some datasets required careful analysis and post-processing. Also, some specific requirements for measurements made modification of existing experiments and the creation of multiple entirely new setups necessary. In the following, we highlight lab-based techniques that were set up, modified and utilized over the course of the PhD.

3.3.1. MOKE and Kerr microscopy

The interaction of light in the optical wavelength regime in the form of the magneto-optical Kerr effect (MOKE) and Faraday effect has become the go-to characterization technique for magnetic thin films [131]. These optical methods detect magnetization-induced changes in the polarization state of reflected light, providing a direct and non-invasive probe of the sample's magnetic state [132, 133].

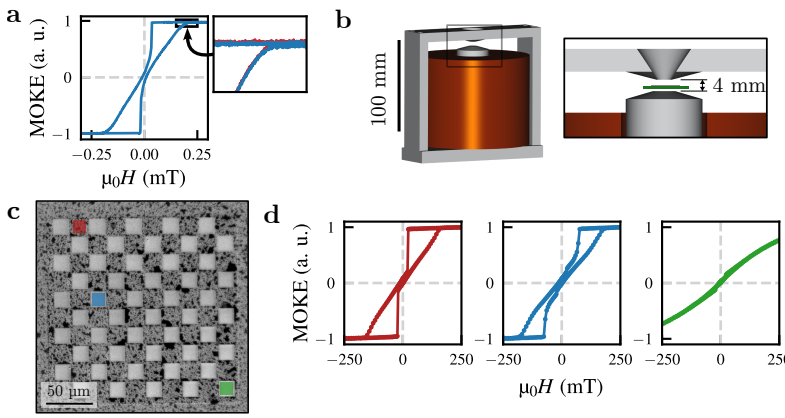

Figure 3.6 | Sample characterization via MOKE. a Hysteresis loop of a Co/Pt-multilayer recorded with the newly implemented laser-MOKE setup. The inset demonstrates the vanishing drift between two consecutive measurements (red versus blue) and the low base noise level of <0.4 %. No filters and drift corrections are applied. **b** Overview of the flux-closed magnet design. The pole geometry close to the sample is shown in the inset. **c** Wide-field image of the domain structure in an ion-patterned Co/Pt-multilayer sample. **d** Raw data of local hysteresis loops extracted at the positions marked in (c) for various ion doses.

In this thesis, MOKE was used both to record field-dependent hysteresis loops and to investigate domain nucleation dynamics with picosecond temporal resolution.

A laser-based MOKE setup was constructed for rapid and reliable magnetic characterization. It enables hysteresis loop measurements under applied fields of up to 1.4 T, averaged over a circular spot of approximately $\varnothing = 2\,\mathrm{mm}$. A single loop is recorded within 0.1 s to 10 s, depending on the required field resolution. To minimize long-term drift, the optical path was kept compact, and all components, including the sample, were rigidly mounted. The resulting system exhibits minimal signal drift and maintains a low noise floor (<0.4 %), as seen in Fig. 3.6a. Oversampling and digital filtering can further improve signal quality if necessary.

The laser-MOKE setup averages over a large area of the sample surface. However, for the engineering of artificial nucleation sites, we required the measurement of the field-response of microscopic patches of material, where the local magnetic properties were altered by ion bombardment. To this end, we built an epi-illuminating Kerr-microscope, which uses the Kerr-effect to make magnetic domain contrast visible. The microscope integrates a custom-built electromagnet with a flux-closed yoke (Fig. 3.6b) that provides fields up to 1.4 T. Its enclosed geometry effectively confines the magnetic field, significantly suppressing stray fields and minimizing parasitic Faraday rotation within optical components, such as the objective lens.

Figure 3.6c shows ion-bombarded patches in a Co/Pt film arranged in a checkerboard pattern. For the color-indicated regions of size 10 µm × 10 µm the local hysteresis loop is plotted in Fig. 3.6d. The locally extracted measurements not

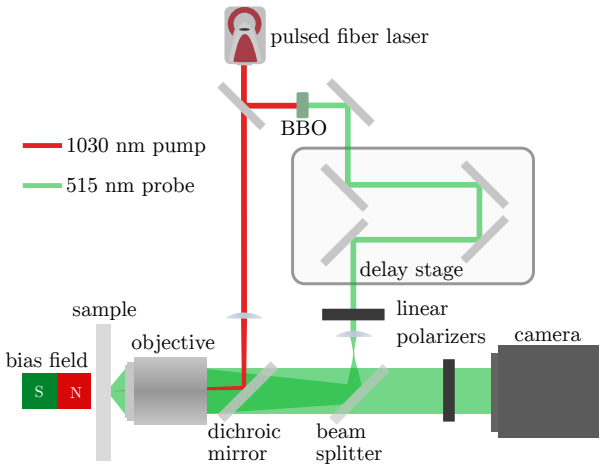

Figure 3.7 | Sketch of the time-resolved Kerr microscopy setup. The infrared laser pulse is split up into the pump part and the frequency-doubled probe beam, which is used for real space imaging of the magnetic state via MOKE.

only demonstrate the strong lateral variability of the shape of the hysteresis loop but also show the almost negligible contribution of the parasitic Faraday signal: At saturation, signal plateaus confirm the negligible contribution of Faraday rotation, matching the performance of the laser-MOKE system with slightly reduced acquisition speed.

Quasi-static and time resolved domain nucleation studies were performed with a laser-based full-field pump-probe MOKE microscope (compare Fig. 3.7 and [134] for a detailed description). A fiber laser emits 1030 nm pulses with durations as short as 250 fs. Each pulse is split into an excitation beam at the fundamental frequency and a probe beam, which is frequency-doubled with a BBO crystal. Both pulses hit the sample collinearly through an objective lens with a tunable delay between −50 ps and 1 ns. Fine-grained field control was achieved by integrating the same electromagnet design as described above.

3.3.2. Anomalous Hall effect measurements

A custom-built Hall transport setup was developed to record hysteresis loops of thin film samples under varying temperatures and applied magnetic field angles (see Fig. 3.8). Compared to MOKE, anomalous Hall effect (AHE) measurements offer several advantages: The measured signal is free from strong parasitic contributions, in contrast to potentially strong Faraday contributions in MOKE measurements, and the only additional unavoidable signal in an AHE-measurement is the normal Hall effect, which is negligibly small in comparison [135, 136]. Additionally, AHE probes the full thickness of the sample, rather than just the surface, making it particularly valuable for analyzing thick or inhomogeneous films. Finally, samples do not need to be optically accessible or mechanically stable. Instead, only four

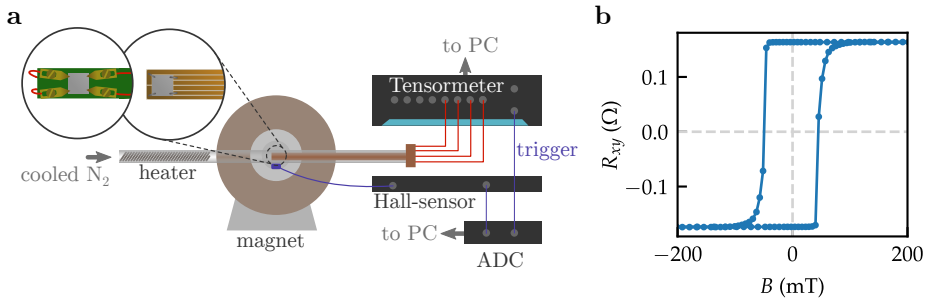

Figure 3.8 | Anomalous Hall effect measurement setup. **a** Schematic of the experimental setup. The transversal sheet resistance is measured with the Tensormeter with a repetition rate of 50 Hz. Its trigger signals are recorded simultaneously with the magnetic field by an ADC at 5 kHz. **b** Example for a OOP hysteresis loop of a DyCo thin film measured in the rapid acquisition scheme.

electrical connections to the sample are required, which facilitates the integration into a complex sample environment.

Similar to MOKE, AHE primarily probes electronic states near the Fermi level [102, 137, 138]. In rare-earth transition-metal alloys, this implies that the measured magnetic signal originates almost exclusively from the transition metal, since the magnetic $4f$ states of the rare-earth element lie several electronvolts above and below the Fermi energy $E_\mathbf{F}$ [139].

The setup (Fig. 3.8a) is built around a commercial Tensormeter RTM1 measurement device. This device can measure the offset-free Hall signal in a four-wire geometry by switching the input-output configuration between consecutive measurements. By capturing the magnetic field strength simultaneous to the trigger signal of the Tensormeter, each field value and data entry can be matched. Samples are mounted and connected onto a carrier board with electric signal lines either by metal clamps or wire bonding. The carrier is inserted into a flow cryostat between the pole shoes of an electromagnet. Because the sample can be freely rotated within the cryostat, the angle of the applied field can be freely chosen while measuring the OOP magnetization component (exemplary shown in Fig. 3.8b). The sample environment allows for arbitrary magnetic fields up to 2 T and temperatures between 80 K and 450 K. The capabilities of the setup are used in chapter 5 to determine the composition of a RE-TM alloy and in chapter 6 to specify the magnetic anisotropy of a ferromagnetic thin film.

3.3.3. SQUID magnetometry

An MPMS3 magnetometer was used to determine material parameters and to investigate the low-temperature behavior of our ferrimagnetic samples. The device employs a commercial implementation of a superconducting quantum interference device (SQUID), allowing for the precise measurement of a sample's magnetic

moment in applied bipolar magnetic fields up to 7 T and at cryogenic temperatures. Since a SQUID measures a signal proportional to the total magnetic moment along the instrument's oscillation axis, the absolute magnetization can be determined if the sample dimensions are known and the instrument is properly calibrated. Owing to its superior sensitivity compared to classical vibrating sample magnetometers (VSMs), SQUID magnetometry is particularly well suited to determine saturation magnetization values of our magnetic thin-film samples [31, 140].
For measurements, samples were mounted inside plastic straws, aligned either OOP or IP with respect to the field and oscillation axis (see also [141]). The high-speed VSM-SQUID mode was typically used to acquire high-quality hysteresis loops. When absolute magnetization values were required, the DC-SQUID mode was employed. While the latter offers slightly lower signal-to-noise performance, it is significantly less susceptible to sample drift, which can lead to erroneous readings of the magnetic moment.
Additional care had to be taken with the sample preparation and data interpretation [142]: Substrates add a para- or diamagnetic background to the signal that needs to be removed. Additional impurities and contaminations on the sample and sample holder give rise to parasitic signals. Finally, the calibration of the instrument assumes a specific size and oblong cylindrical shape of the sample. Our deviating sample geometry may skew the absolute measured values of the magnetization [143]. Indeed, measuring the same sample in OOP- compared to IP-configuration led to variations in measured M_s by up to 10 %.
Examples for data acquired with SQUID can be found in the appendices A.1, A.2, and A.4.

3.3.4. Lorentz-TEM

Lorentz transmission electron microscopy (L-TEM) is a powerful technique for resolving magnetic structures in thin films at nanometer scale. All measurements presented in this work were performed by our collaborators in the group of Prof. Claus Ropers at the Georg-August-Universität Göttingen.
When electrons are transmitted through a magnetic sample with a finite magnetization, the electrons are exposed to a Lorentz force $\mathbf{F_L} = -e(\mathbf{v} \times \mathbf{B})$. Here, $-e$ is the electron charge, $\mathbf{v}$ the propagation direction of electrons and $\mathbf{B}$ the local induction caused internal and external stray fields due to the magnetization of the specimen. This Lorentz force leads to deflection of electrons passing through the sample [144]. By slightly defocusing the electron microscope (Fresnel mode) this deflection becomes visible on the detector. Due to the cross product, only magnetization perpendicular to the electron beam contributes to the Lorentz-contrast.
For samples with perpendicular magnetic anisotropy, this implies that contrast arises primarily from domain walls, where in-plane magnetization components exist. Specifically, under normal incidence ($\theta = 0°$), only Bloch-type domain

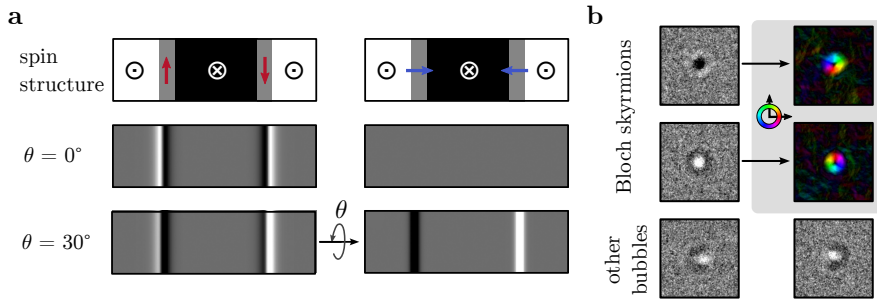

Figure 3.9 | Interpretation of Lorentz-TEM data. a Expected domain wall contrast for Bloch and Néel -type domain walls in defocused Fresnel-mode. While in normal incidence ($\theta = 0°$), only Bloch-type walls are visible. Tilted incidence enables contrast from Néel-type walls. Adapted from [145]. **b** L-TEM images of Bloch skyrmions with clockwise and counterclockwise chirality and their corresponding reconstructed in-plane magnetization. Non-topological bubble domains show deviating contrast.

walls produce Fresnel contrast, appearing as black-white or white-black transitions depending on their chirality (Fig. 3.9a) [145]. In contrast, the electron deflection of Néel-type domain walls cancels out in normal incidence, such that no contrast emerges. Tilting the sample away from normal incidence gives additional signal at the domain walls, hence also Néel walls become visible (compare Fig. 3.9a).
At a vertical Bloch line, two Bloch domain walls with opposite chirality meet. This results in an inversion of the Lorentz-contrast along the domain wall – shifting from black-white to white-black or vice versa. In consequence, a defect-free, homochiral domain wall of a magnetic Bloch-type skyrmion exhibits a uniform contrast orientation across its perimeter [146]. Figure 3.9b shows examples of Bloch skyrmions with both chiralities, along with their reconstructed in-plane magnetization. For comparison, bubble domains with non-topological wall structures display distinct contrast patterns that deviate from those of skyrmions.

Chapter 4
Chirality variations in ferrimagnetic rare-earth transition-metal alloys

The material class of rare-earth transition-metal alloys exhibits many appealing physical properties, including ferrimagnetism, perpendicular magnetic anisotropy, all-optical switching and bulk DMI. The latter is of particular importance for the stability of small, mobile skyrmions in compensated magnetic materials. Such compensated skyrmions can be moved without detrimental skyrmion Hall effect. The most unambiguous way to determine the presence of DMI in a magnetic thin film is to observe Néel-type domain walls. In this chapter, we introduce a vector spin imaging technique based on x-ray magnetic linear dichroism contrast. We demonstrate the technique on thin films of a DyCo alloy with perpendicular magnetic anisotropy. In this material, we find not only Néel-type domain walls that are likely bulk-DMI stabilized but also observe generally strong lateral variations of the domain wall angle. Hence, while the material exhibits DMI and hosts chiral domain walls, the chirality is a local property. Even defect free skyrmionic bubbles are not necessarily surrounded by a homochiral domain wall. We present evidence that the chirality variations could be caused by regions of altered material composition. Our findings suggest that the lateral material composition changes emerge during sample growth and are directly linked to and potentially even caused by the as-grown magnetic domain configuration. These magnetism-induced inhomogeneities join the growing set of exotic phenomena in rare-earth transition-metal alloys. While they give rise to fundamental questions about the growth characteristics, they also offer possibilities to control the local domain wall chirality as well as the micromagnetic properties in future nano-spintronics applications.

4.1. Introduction

Rare-earth transition-metal alloys combine many unique magnetic properties and phenomena, including ferri- and sperimagnetism [147], skyrmions [148, 149] and helicity-independent all-optical switching [28]. The material class is therefore highly appealing for fundamental research and for potential future applications. Among

these intriguing phenomena is the recent discovery of bulk Dzyaloshinskii–Moriya interaction (DMI) in GdFeCo thin films [9]. Bulk DMI does not rely on the symmetry breaking at a heavy metal material interface. It is therefore a highly desirable property for the development of thick, compensated magnetic films with strong DMI, which do not require stray field interactions like high-DMI repeating multilayer structures. Such films are ideal hosts for thermally stable, yet small and mobile skyrmions with Néel chirality. These compensated skyrmions would be movable by electric currents, without the emergence of the skyrmion Hall effect, which introduces a generally undesirable skyrmion propagation perpendicular to the current flow [63, 150], and generally have a higher skyrmion velocity. Bulk DMI was found to emerge from a growth-induced vertical composition gradient in combination with spin-orbit coupling within the ferrimagnetic material. In the same material class, in the context of all-optical switching, it was observed that also lateral composition variations exist in the sputtered films [8]. The question remains how such lateral composition gradients impact the statics and dynamics of magnetic textures in the thin film and specifically the domain wall chirality.

The chirality of a magnetic domain wall is one of its most defining properties. Of heightened interest for spintronics applications are domain walls and skyrmions with pure Néel-type chirality, as these can easily be moved by electric currents [148, 151]. Local domain wall defects, such as vertical Bloch lines, further modify the stability [6], topology and mobility [152, 153] of magnetic features. It is therefore of great scientific interest to engineer and tune the domain wall to a desired chirality. Equally important, however, is the ability to also investigate and resolve the local domain wall spin structure. Techniques range from volume-averaging methods like chiral XRMS [154, 155] to direct imaging techniques, including Lorentz-TEM [145, 156], MFM [157], SPLEEM [158, 159] and SEMPA [22, 160]. Each technique has specific strengths for particular use cases, such as the element-specificity of x-ray-based techniques, the high resolution and sensitivity of MFM or the bulk sensitivity of Lorentz-TEM. Missing, however, is a technique that combines the power to resolve the domain wall chirality with high spatial and temporal resolution with bulk sensitivity and element specificity, while also working well in complex sample environments.

In this study, we investigated DyCo thin films with the goal to find bulk DMI-stabilized Néel-walls as well as to develop a robust technique to identify such chiral structures. We developed an XMLD-based vector spin imaging technique, which allows the unambiguous distinction between Bloch and Néel type domain walls as well as states of intermediate chirality. We observed strong spatial variations of the domain wall chirality in the as-grown state of the magnetic film, ranging from full Bloch to full Néel handedness. Complementary MFM-imaging revealed a faint magnetic background contrast that coincides with the position of the initial as-grown domain walls. We connect both observations to spatial variations of the material

composition, which leads to modifications in the local saturation magnetization and DMI strength. We suspect an interplay between these phenomena and the domain wall formation during sample growth.

4.2. Sample fabrication and characterization

We prepared DyCo-alloy thin films on x-ray transparent SiN-membranes. The specific layer configuration was SiN/Ta(4 nm)/Pt(6 nm)/$Dy_{0.19}Co_{0.81}$(50 nm)/Ta(3 nm)/Pt(4 nm), as shown in Fig. 4.1a. We chose DyCo for two reasons: First, the required composition gradient [83] as well as strong spin-orbit coupling have been reported in this material [161], which makes it a likely candidate to show bulk DMI. Second, the material reportedly exhibits measurable XMLD at the Dy M_5-edge [83], which our imaging method is based on. The alloy was terminated asymmetrically with Ta and Pt to allow for future spin-orbit-torque-based spintronics experiments. We do not expect that the induced interfacial DMI has a major impact on the domain wall chirality, due to the considerable thickness of the magnetic layer.
The DyCo samples were grown via magnetron (co-)sputtering at a base pressure of $p_{\mathrm{base}} = 1.4\times10^{-8}$ mbar and a working pressure of $p_{\mathrm{w}} = 1.5\times10^{-3}$ mbar. All growth rates r for each individual component were determined prior to the deposition with a quartz crystal monitor at the substrate position and the deposition times were linearly extrapolated. For the growth rate of the co-sputtered DyCo alloy we assumed $r_{\mathrm{DyCo}} = r_{\mathrm{Dy}} + r_{\mathrm{Co}}$.
We determined the volume averaged alloy composition by measuring the compensation temperature $T_M = 162$ K with SQUID (comp. Fig. 4.1d). This temperature value was then compared to compensation-temperature versus composition data for DyCo found in the literature [162]. The precise sample thickness was determined by cutting a lamella of the thin film and resolving the element distribution with transmission electron microscopy (Fig. 4.1c). The magnetic anisotropy K_{u} was calculated as described in appendix A.2.
A room temperature hysteresis curve of the material is shown in Fig. 4.1b. The loop is generally square shaped, with full remanence and a sharp nucleation at $H_{\mathrm{N}} = -40$ mT. However, the following gradual approach towards full magnetization inversion at $H_{\mathrm{S}} = -110$ mT hints towards low domain wall mobility. The cause for the mobility reduction is strong magnetic pinning within the material, which hinders the domain wall propagation at moderate driving fields. A side effect of the pinning is the possibility to create a stable multi-domain state via field cycling. The domains in such a demagnetized state are, however, considerably larger than in the initial as-grown domain state (comp. Fig. 4.1b).
While the room temperature hysteresis loop is essentially square, its form changes considerably when approaching the compensation temperature (Fig. 4.1e). Here, the magnetization stays almost zero, up until a transition above 2 T. Such behavior

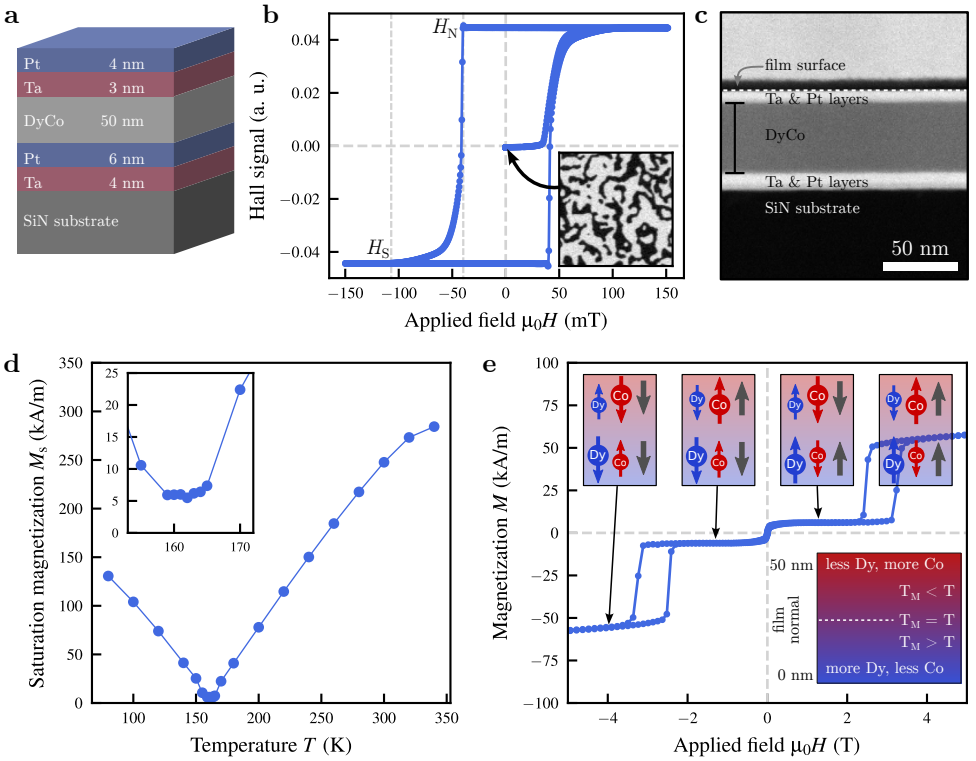

Figure 4.1 | Characterization results of the DyCo thin film. **a** Sputter-grown materials stack. **b** AHE-recorded OOP-hysteresis loop, including the virgin curve. The inset shows the as-grown domain state. **c** TEM cross section through the sample. On top of the capping layer, a protective Pt-cap was deposited for the lamella milling. **d** Saturation magnetization versus temperature measured at an OOP holding field of 1.5 T. The inset shows a zoomed in view around the compensation temperature (162 K). **e** SQUID-recorded OOP hysteresis loop at the compensation temperature. The magnetic transitions at high fields by creation and annihilation of the horizontal domain wall are visible. The transition at zero field could also be parasitic signal from magnetic material deposited on the edges of the substrate [163]. The bottom inset illustrates the varying compensation temperature in the material due to a composition gradient, which splits the magnetic layer into two regions, one below and one above T_M. The top insets show the magnetic configuration in these two regions for the highlighted field regimes.

is the fingerprint of a synthetic antiferromagnet [164]. It was shown that in DyCo this effect originates from a composition gradient along the film normal, such that the material is partially above and below the local compensation [83, 165]. Compare appendix A.1 for the entire temperature dependent dataset.
With signs of the compositional gradient present, our sample exhibits all requirements for bulk DMI. We cannot measure the DMI directly: Brillouin light scattering (BLS) requires the sample to be in-plane magnetized and low damping of spin waves. The first requirement would call for strong, technically challenging in-plane fields, while the second requirement is simply not given in our samples. We attempted field-angle dependent coercivity measurements as described in [166]. This method did not succeed, however, also due to the considerable magnetic pinning. The same would likely be the case for domain expansion experiments. Hence, determining the DMI strength from the domain wall chirality and searching for Néel-type domain walls was the most logical procedure. Here it was important to use a thickness-averaging measurement technique to probe the chirality of the entire domain wall profile along the film normal. A surface sensitive technique (e. g., SEMPA) would not be able to distinguish between DMI-stabilized Néel-type domain walls and flux closure Néel caps (compare section 2.2).

4.3. XMLD vector imaging

We developed XMLD vector imaging as a technique to resolve the local chirality of magnetic domain walls. We aimed to be able to clearly distinguish Bloch and Néel walls as well as intermediate states of chirality. The analysis method was adapted from a technique used to image magnetic vortices with XMLD-PEEM in IP-hematite [167] to domain wall imaging in transmission geometry in our thin films with perpendicular anisotropy. In this section, we detail the steps necessary to get a domain wall reconstruction. We show the requirements for the experimental setup to achieve a high-quality vector image and verify the validity of the method by comparing it to Lorentz-TEM. Finally, we show our best reconstruction result thus far, which was achieved by combining our technique with the resolving power of coherent x-ray imaging.

4.3.1. Acquisition and reconstruction process

The XMLD effect describes the different absorption of linear polarized x-rays in a magnet, depending on the angle between light polarization and magnetization (compare section 3.1.3). In first approximation, the additional absorption is proportional to $\cos^2(\alpha)$, with α being the angle between the light polarization and magnetization: The XMLD effect is maximal if the light polarization and the magnetization direction align, and minimal if they are orthogonal. Depending on

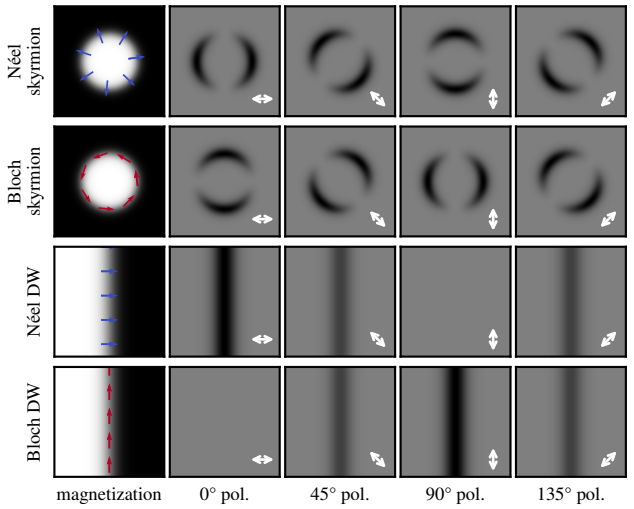

Figure 4.2 | Calculated XMLD contrast examples for a variety of basic magnetic features, including skyrmions and domain walls of pure Bloch- and Néel chirality. The black-white contrast in the first column is proportional to the expected XMCD-contrast. The other columns show the expected XMLD absorption for linear polarized x-rays with varying polarization angle (indicated by white arrows).

the photon energy, the magnitude and sign of the XMLD can change. However, in our samples, at the photon energy with maximal XMLD contrast, alignment of the polarization and magnetization always resulted in increased absorption, hence a reduction in transmission (compare Fig. 3.2). Recording the local XMLD-absorption in a magnetic thin film with x-rays under normal incidence is therefore sensitive to the direction of the in-plane magnetization. Figure 4.2 shows simulations of the XMLD-induced transmission contrast for various prototypical magnetic features and x-ray polarizations. One finds that the XMLD-contrast solely depends on the in-plane magnetization axis and not the actual magnetization direction. This loss of directionality stems from the fact that linear light polarization of a certain angle θ is equivalent to the polarization angle $\theta + 180°$. This property also transfers to the XMLD contrast.

With full directional information, two orthogonal linear light polarizations would suffice to reconstruct the two-dimensional in-plane magnetization vector: They would each be proportional to one in-plane component of the magnetization (compare XMCD imaging in chapter 5, where this is the case). However, with the directional degeneracy added as a degree of freedom in the XMLD-contrast, certain magnetic configurations cannot be distinguished: Compare, e. g., in Fig. 4.2 the Bloch and Néel domain walls, which give the identical signal for both diagonal x-ray polarizations. In consequence, it is required to record more than two polarization angles to unambiguously reconstruct the in-plane magnetization axis. We opted for four different angles, 45° apart, which worked well for us in practice.

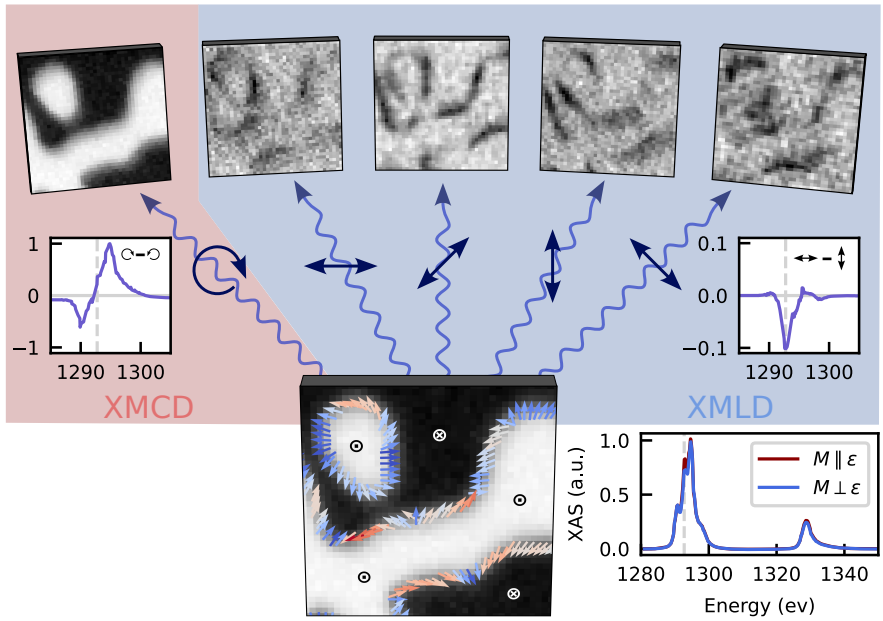

Figure 4.3 | Overview of the XMLD vector reconstruction process. Each image in the top row shows the recorded transmission data for the indicated x-ray polarization from the reconstructed magnetization pattern. Inset plots show the XMCD-spectrum (left) and XMLD-spectrum (right) around the absorption edge, as well as the extended XAS spectrum, highlighting the small XMLD contribution. Images were recorded at MAXYMUS and spectra at the VEKMAG enstation at BESSY-II.

Laterally resolved images of the XMLD contrast under different angles must be aligned with each other, and possible sample drift needs to be removed. All images are normalized against the maximum transmission, hence the parts of the material where the magnetization is orthogonal to the polarization. Each pixel-coordinate has a set of four different absorption values, one for each polarization angle (identical to the images in Fig. 4.2). By fitting $I_{\text{transm.}} = I_0(1 - A\cos^2(\alpha - \alpha_{\text{max}}))$ to this data, the angle of maximum absorption – and therefore the angle of the magnetization axis – can be determined. Here, α is the x-ray polarization angle, α_{max} is the fit parameter that determines the magnetization axis, and A an arbitrary scaling factor of the XMLD strength.

In practice, most beamlines that we used for XMLD-imaging only supplied linear polarized light in two orthogonal angles (i. e. the horizontal and vertical linear polarization axes). Other beamlines did offer arbitrary linear polarization angles. However, angles aside from the two prime polarization directions were often not perfectly linear but contained a small amount of circular polarization. Because the XMCD effect is substantially stronger than XMLD in DyCo, even when the photon energy was optimized for XMLD contrast, the recorded images were dominated by XMCD-based out-of-plane signal, which completely drowned out the XMLD

contributions. In consequence, to record four different angles of linear polarization, we opted to rotate the sample instead by 45° and align the images in post-processing.
The vector reconstruction method is compatible with any x-ray absorption based imaging technique. We opted to deploy the reconstruction-method with STXM and Fourier transform holography. Both microscopy techniques are transmission-based techniques that have high spatial image resolution with bulk sensitivity and allow for potential time-resolved experiments as well.
Exemplary absorption data acquired by STXM is shown in Fig. 4.3. Each panel shows the absorption contrast for either circular polarized light or for one of each linear polarization direction. The additional absorption from the XMLD clearly appears within the domain walls. However, while the XMCD contrast is essentially noise free, the individual absorption images of linear light exhibit far poorer signal quality. In fact, the XMLD effect is very small in our DyCo alloy and requires long integration times (compare the energy scans in Fig. 4.3, where the XMCD magnitude is ten times larger than the XMLD). However, for this work, only the in-plane spin information within the domain walls was of interest for us, i e. the in-plane information along a one-dimensional manifold that follows the domain wall. We thus applied a directional smoothing algorithm that applies a biased local Gaussian filter, which is very broad normal to the domain wall but narrow parallel to the wall. This treatment improved the signal quality by averaging perpendicular to the wall while conserving the original imaging resolution along the domain wall. As an additional benefit, the impact of slight misalignments between individual images was reduced this way.
The final vector reconstruction is shown in Fig. 4.3. The black-white contrast denotes the out-of-plane magnetization component, while the in-plane magnetization is shown as arrows. The color coding of the arrows follows the convention of Bloch walls being red and Néel walls being blue. Note that the arrow heads are not a result of the XMLD reconstruction but are at this point essentially arbitrarily chosen and may serve as a guide to the eye. The scientific interpretation of the magnetization structure will be discussed in section 4.4.

4.3.2. Verification of reconstruction and integration of Lorentz-TEM contrast

We performed Lorentz-TEM imaging to verify the validity of our vector spin imaging technique. In Fresnel mode, the objective lens is deactivated, ensuring that the sample remains free from externally applied magnetic fields. Thereby, the as-grown magnetic state can be imaged without disturbance by defocusing the beam. In this imaging mode, the deflection of electrons by the local magnetization of the magnetic material can be detected. In normal incidence, no magnetic contrast arises within the OOP-magnetized domains, due to vanishing Lorentz-forces in

the case of parallel field and electron propagation direction. Within domain walls, however, the in-plane magnetization component gives rise to a Lorentz deflection. Bloch type domain walls lead to a characteristic black-to-white fringe pattern, wherein the direction of black-to-white contrast depends on the chirality of the wall. Pure Néel type domain walls do not show Lorentz contrast.

In Fig. 4.4a) and Fig. 4.4b) the same field-of-view of the DyCo film is shown as reconstructed from XMLD imaging and recorded via Lorentz-TEM. Wherever the XMLD reconstruction predicts a domain wall with a non-zero Bloch component, the domain wall shows Lorentz contrast. Where we expect Néel walls, the Lorentz contrast vanishes (sections marked blue in Fig. 4.4b). Due to the good agreement between both techniques, we can reasonably assume that the results from XMLD vector imaging are valid. Specifically, we can distinguish pure Néel chirality from sections with a Bloch component and reliably determine the domain wall angle.

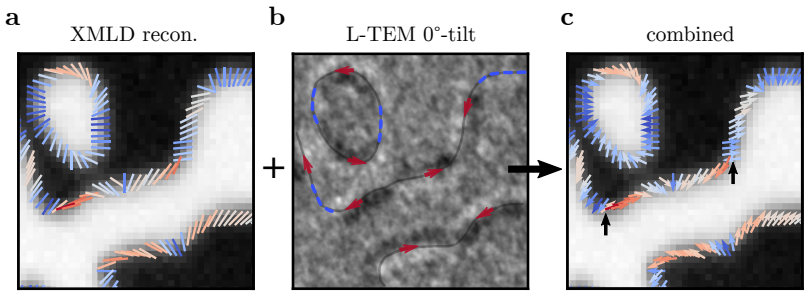

Figure 4.4 | Integration of Lorentz-TEM data. **a** XMLD-based reconstruction without directional information. **b** Lorentz-TEM contrast of the same state. Solid lines indicate the domain wall position in the STXM data. Red arrows show the derived Bloch chirality. Dashed blue lines denote domain wall sections with vanishing Lorentz contrast due to Néel chirality. **c** Recovered full directional in-plane magnetization information. Black arrows highlight mismatching chirality.

Additionally, the information of Bloch directionality in the L-TEM data allows us to lift the directional degeneracy in the XMLD reconstruction. Where a sufficiently large Bloch component is present, the direction of the black-to-white transition in the Lorentz-contrast directly defines the direction of the in-plane magnetization (such sections are marked by red arrows in Fig. 4.4b) Adjacent Néel sections can be recovered by minimizing the total exchange energy in the simplified domain wall: In general, the ferro- and ferrimagnetic exchange interaction favors parallel alignment of the magnetization (within the same sublattice). Hence, magnetic moments in the domain wall should rotate smoothly. Starting from the Bloch sections with known directionality, the alignment between pairs of neighboring spins is compared and the orientation chosen such that the scalar product between the two is maximized. This in return minimizes the magnetostatic energy. This Ising-like optimization routine of the spin alignment is performed throughout the entire domain wall, thereby “combing” the magnetic moments into one direction.

Aside from few exceptional points (marked with black arrows in Fig. 4.4c), this method returns a smooth vector field for the majority of domains. We can attribute these points to either local domain wall defects such as vertical Bloch line defects, which are so small that the finite resolution of the STXM makes them appear as discontinuities or XMLD-reconstruction artifacts due to a low signal-to-noise ratio.

4.3.3. Resolution benchmark: Coherent XMLD vector imaging

STXM is an extremely versatile and user-friendly technique that works well together with XMLD vector imaging. However, the achievable resolution is limited by the size of the scanning x-ray spot on the sample, caused by the relatively small effective numerical aperture of the focusing x-ray optics. Additionally, sample drift makes longer acquisitions for better SNR and the alignment of the different polarizations difficult, especially for samples with weak XMLD-contrast. Coherent imaging techniques are a way to overcome the spatial resolution limit, as they theoretically allow for resolutions up to the wavelength limit. Fourier transform holography is particularly interesting for low-contrast samples, as the fixed mask makes the technique inherently drift free and the alignment of multiple images trivial. The relatively new HAPRE imaging and reconstruction method promises to combine cutting-edge resolution with drift-free imaging [26]. Here, we demonstrate XMLD vector reconstruction working exceptionally well together with this coherent imaging technique.

Coherent imaging experiments were performed at the BOREAS-beamline at the ALBA synchrotron. We used a holographic mask layout that was designed specifically for HAPRE. A SEM-micrograph is shown in Fig. 4.5a. The total footprint of the mask was minimized such that the spatial coherence between the object and reference wave from the two small reference holes is as large as possible. Additional large transmission holes were placed close to the object aperture. Their size and position results in increased scattering over a large q-range, which makes it easier to acquire magnetic signal at large scattering angles through heterodyne mixing and thereby resolve smaller features.

An exemplary XMLD-scattering pattern is shown in Fig. 4.5a. It depicts the difference in the holograms acquired with horizontal and vertical linear polarized light. We can see modulations of the magnetic signal up to the edges of the screen, which corresponds to a reconstructed pixel resolution of 15 nm at the Dy M_5 edge (1292.6 eV [107]). Each individual hologram is a composite of two scattering images with differently sized beam stops. The phase of each hologram was reconstructed via phase retrieval as detailed in [26].

The real space reconstructions of the XMLD contrast are shown in Fig. 4.5b and 4.5c for the two sets of orthogonal linear polarizations. Each image is presented as the difference of two polarizations such that the otherwise dominant topographic signal cancels out. Combining the individual images results in the vector reconstruction

as shown in Fig. 4.5d. Here, the in-plane domain wall information is depicted on top of the XMCD contrast, which corresponds to the out-of-plane magnetization. The color of the in-plane component corresponds to the reduced domain wall angle $\Psi = \arcsin|\sin(\psi)|$, which indicates if the domain wall is closer to a Néel ($\Psi = 0°$) or Bloch configuration ($\Psi = 90°$).

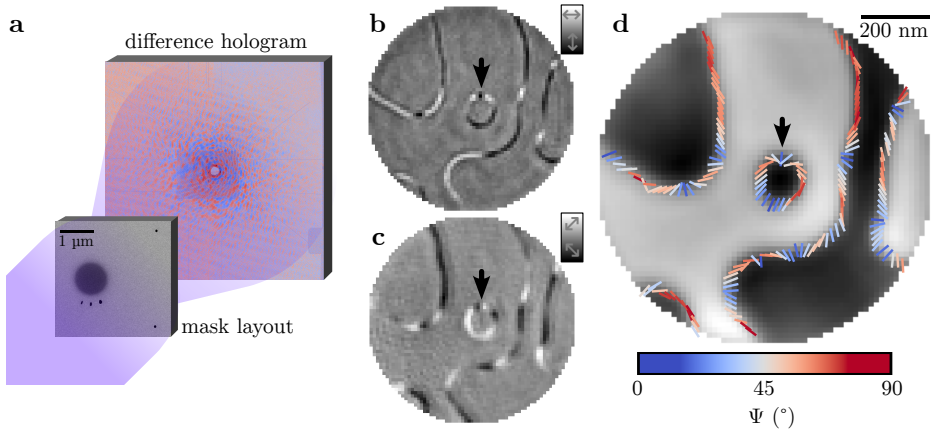

Figure 4.5 | XMLD holography scattering image and reconstruction. a SEM image of the FIB-fabricated optimized holography mask and difference scattering pattern LH-LV linear polarization. **b** Difference image of the phase retrieved reconstructions of linear horizontal and vertical XMLD contrast, **c** the same for diagonal polarizations. **d** Vector reconstruction of the domain wall chirality overlaid with out-of-plane magnetization from XMCD contrast. The color indicates the reduced domain wall angle Ψ with red equalling Bloch and blue equalling Néel chirality.

In the top third of the field of view, the domain walls are essentially monochiral with dominant Bloch characteristics. The rest of the reconstruction reveals strong in-plane modulations in the form of chirality variations and domain wall defects. We focus on the small, circular bubble domain in the center of the reconstruction. At the top of the bubble, a vertical Bloch line separates two Bloch domain wall sections (marked). Because this domain wall defect is compact, it results in rapid contrast changes in the XMLD difference images. Indeed, in Fig. 4.5b we observe a transition from white to black to white over just four pixels. Each individual transition therefore must be less than two pixels in width, which is close to the theoretical recoverable maximum resolution. Our reconstruction resolution therefore likely takes full advantage of the capabilities of the imaging setup with the potential to easily achieve even higher spatial resolutions by deploying a larger detector or a smaller sample-detector distance to capture a larger q-range.

4.4. Spatial variations of magnetic properties

4.4.1. Chirality variations in DyCo

With the validity of XMLD-based vector spin imaging established, we can utilize the method as a tool to resolve the domain wall chirality in our DyCo thin film. Figure 4.6a shows the full field vector reconstruction of the as-grown state in DyCo. X-ray data was recorded with STXM at MAXYMUS (BESSY-II) and the in-plane magnetization directionality was added via Lorentz-TEM. The large field of view of 3.3 µm × 3.3 µm contains many domains, which results in representative statistics of the overall domain wall chirality. The histogram of the chirality distribution is shown in Fig. 4.6b. A significant amount of domain walls exhibits Néel character. Indeed, we observe multiple extended sections of pure Néel chirality (examples are marked by blue dashed lines in Fig. 4.6a). These sections are too large to be simple Bloch line defects; hence they are likely stabilized by DMI. In the same field of view, we also find some domain wall sections of Bloch chirality (marked red) and a majority of sections with intermediate chirality. Throughout the sample, the domain walls exhibit strong spatial variations of their chirality. Even in 200-300 nm small bubble domains (e. g., top-left in Fig. 4.6a) we find transitions from Néel to Bloch chirality.

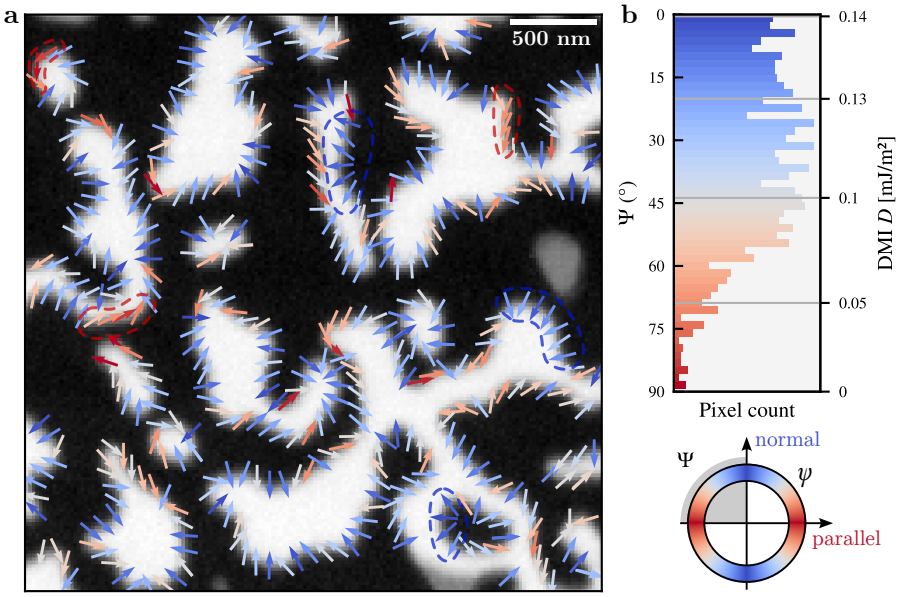

Figure 4.6 | XMLD vector reconstruction. **a** Full vector reconstruction of the magnetization. Colors denote the local chirality of the domain wall, with red=Bloch and blue=Néel. Gray contrast with missing domain wall information are domains that were annihilated during sample manipulation between scans and are therefore missing full in-plane information. The scalebar is 500 nm. **b** Distribution of the reconstructed reduced domain wall angle Ψ. The right axis denotes the required DMI strength to stabilize a certain chirality according to equation (2.14), assuming a fixed M_s.

Cooling the sample from room temperature towards T_M without an applied field leads to no change in the observed OOP domain pattern contrast. Hence, the domain wall positions are stabilized by pinning.

At room temperature, we also saturated the sample with an OOP magnetic field and demagnetized it subsequently by field cycling with decreasing amplitude. The as-grown domain pattern and the demagnetized state of the same sample area are shown in Fig. 4.7 for a fixed FOV. The average domain size after demagnetization is generally larger than the as-grown domains. Notably, the domain walls prefer to form at the same positions where the as-grown domain walls were located before. The domain walls in the material therefore exhibit high magnetic return-point memory.

Figures 4.7c and 4.7d show XMLD difference images of the same magnetic textures before and after the (de-)magnetization process. Domain walls that coincide in both magnetic states show identical XMLD absorption contrast modulations. Even though the recorded information is insufficient to fully reconstruct the magnetization vector, the observation of identical XMLD-contrast heavily implies that the local chirality is the same in both states. Hence, the local chirality largely does not depend on the history of the sample, but rather on the location in the magnetic film. In consequence, the observed variations in chirality must originate from laterally varying material properties.

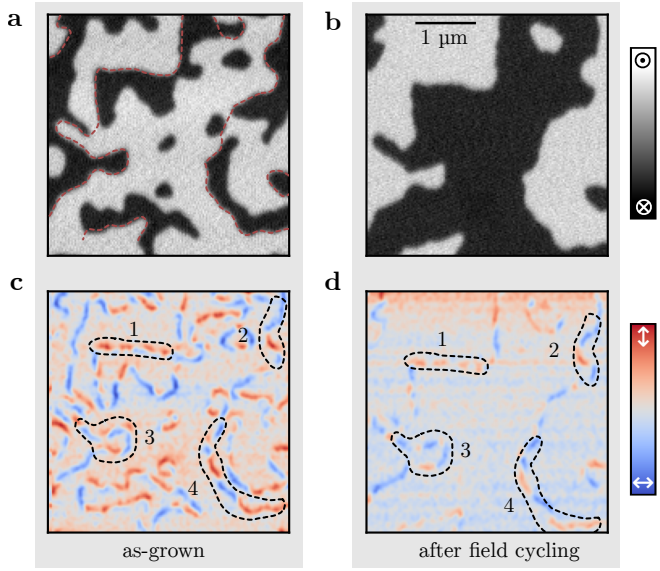

Figure 4.7 | Comparison of domain states in DyCo before and after field-cycling. **a** XMCD image of the original as-grown domain state. **b** Same FOV after saturation and demagnetization by field cycling. The domain outlines were transferred to (a) as red lines for easier comparison. **c** & **d** XMLD difference image (LH-LV) for the same two magnetic states. Examples for regions with high similarity are marked by dashed lines for easier comparison.

4.4.2. Micromagnetic investigation of the chirality variations

We performed micromagnetic simulations to investigate which material parameter variations could lead to the observed strong chirality modulations. We used mumax3 [168] to simulate a $3\,\mu m \times 3\,\mu m$ large area of the thin film, discretized into cells of size $2\,nm \times 2\,nm \times 7.1\,nm$ (hence, 7 layers along the film normal z). We used the material parameters as determined in section 4.2. An initial random magnetization was energetically relaxed to achieve a demagnetized domain pattern. To model the material parameter variations, the film was subdivided into Voronoi-tessellated grains with an average size of 250 nm. A random parameter value was assigned to each grain. We separately varied the local anisotropy K_u, the magnitude of DMI D, and the saturation magnetization M_s.

The resulting domain patterns are illustrated in Fig. 4.8. Figure 4.8a shows the impact of the variation of the DMI, while Fig. 4.8b depicts the results for lateral variations in M_s. We omit the results from varying the anisotropy, as we did not find strong chirality variations. This simulation result is reasonable when considering formula (2.15), where D_{thr} (and therefore the chirality) only weakly depends on K_u. Note that these considerations only include variations of the perpendicular anisotropy, without taking potential in-plane anisotropy terms into account, which go beyond the scope of this thesis.

In contrast, we find strong chirality variations when varying either the DMI or the saturation magnetization. As expected, Bloch and Néel walls in Fig. 4.8a correspond to areas with lowered and increased DMI strength. The threshold for pure Néel chirality is $D = 0.16\,mJ/m^2$. In comparison, in Fig. 4.8b, domain walls turn more Néel upon reduction of M_s. Such behavior is expected, as the required D_{thr} for pure Néel chirality is reduced accordingly (eq. (2.15)). Noteworthy, however, is the required range of M_s-variation to achieve (almost) pure Bloch and Néel chirality in the same sample: The chosen constant DMI-strength $D = 0.1\,mJ/m^2$ requires the saturation magnetization to vary between 200 kA/m and 320 kA/m to form Néel and Bloch walls, respectively, with otherwise identical parameters.

Besides the chirality variations, the variation of M_s also leads to a variation of the local domain size: As the local magnetic moment increases, the stray field energy increases accordingly, which makes smaller domains energetically favorable, as these textures suppress the stray fields outside the film. The same effect leads to domain wall pinning in regions with high M_s, as in-plane structures are favored in high-M_s areas. Note that the domain size is not a good metric to compare to the experimental observations. Aside from a varying M_s-value, the domain size in the simulation is mainly influenced by the size of the grains, which was arbitrarily chosen.

Both simulated magnetization patterns exhibit large amounts of vertical Bloch line defects. Unlike the extended areas of Néel chirality due to parameter variation, these defects are spatially confined to a few nanometers. The experimental STXM data

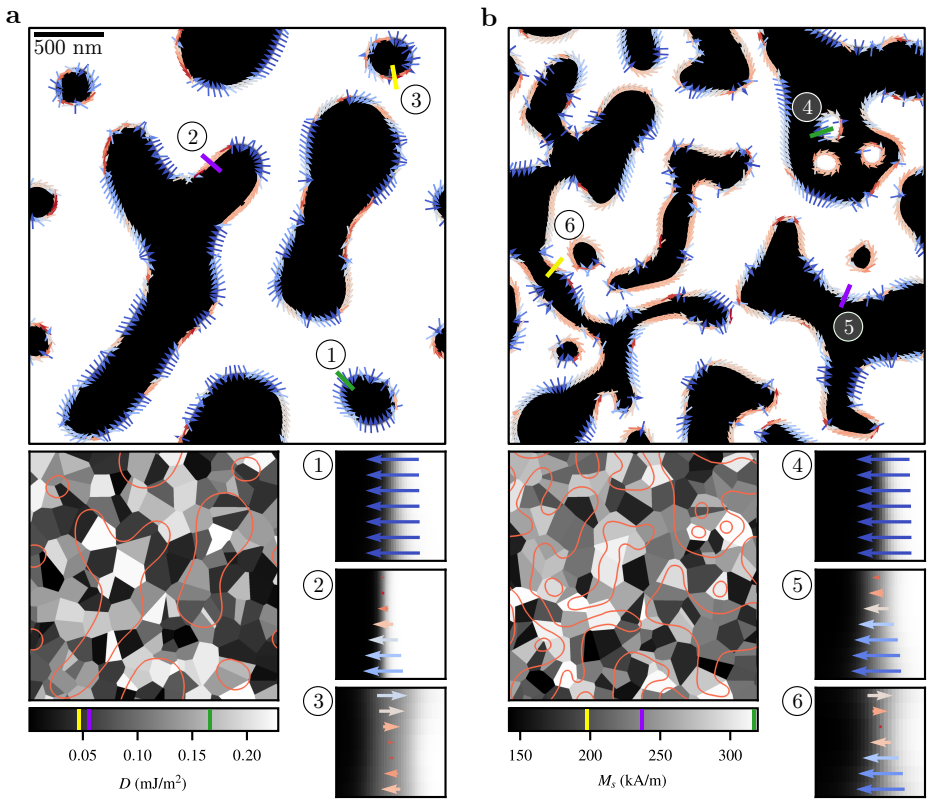

Figure 4.8 | Micromagnetic simulations of inhomogeneous films. Relaxed domain pattern from a random state. **a** Spatial variation of DMI-strength D. **b** Spatial variation of the saturation magnetization M_s. The voronoi-pattern of the parameter variation is shown in the subplot, superimposed with the domain outlines. Other micromagnetic parameters are kept spatially homogeneous. Cross-sectional views of marked domain wall sections and the corresponding parameter value are shown.

in Fig. 4.6 also shows some spin structures that are likely Bloch lines. Especially in domain wall sections where the in-plane component abruptly changes by 180° a Bloch line is likely hidden beneath the finite STXM resolution. In fact, the Bloch line defects are clearly resolved in coherent imaging (Fig. 4.5d).

Figure 4.8 also shows cross-sections through domain walls of varying chirality. On the one hand, these confirm the pure Néel-type chirality all throughout the film for sections with high DMI or low M_s. On the other hand, intermediate and "Bloch"-sections show a pronounced twist of the in-plane component from Néel to Bloch to Néel with inverse chirality. Such behavior is typical for flux closure effects, which minimize the energy cost of stray fields outside the magnetic film by rotating the domain wall chirality. In a DMI-free material, the center of the domain wall is Bloch, and twists towards Néel at the interfaces. Once DMI is introduced, one Néel chirality becomes energetically favorable. In consequence, the Bloch

section is localized closer towards the interface, thus reducing the higher-energy Néel component.

Due to the twisting domain wall angle, a zero-DMI flux closure domain wall is not purely Bloch type. However, it still appears as such in the XMLD vector-analysis as well as the Lorentz-TEM data. The former averages over the entire film thickness and determines the average magnetization axis, which is the central Bloch-alignment. The latter is inherently not sensitive to Néel-components in the 0°-tilt configuration, due to the contrast mechanism. Nevertheless, "Bloch-like" flux closure domain walls are still a sign for either vanishing DMI or increased saturation magnetization.

4.4.3. Imprint of the as-grown domain state on material properties

According to the micromagnetic simulations, variations of the DMI and the saturation magnetization can equally contribute to the domain wall chirality variations. To untangle both contributions, we performed MFM imaging in search for variations in M_s. Measurements were performed with a custom-built in vacuum setup by our collaborators in the group of Prof. Hans Josef Hug at EMPA. The high quality factor of the cantilever in combination with single pass operation [169] allows for exceptional sensitivity and resolution of the setup, even within applied magnetic fields (compare, e. g., [170–172]). We imaged the same sample that was investigated in the XMLD-imaging experiment in STXM.

Our findings are illustrated in Fig. 4.9. Figure 4.9a shows the purely magnetic signal of the DyCo film after demagnetization via field cycling. This signal corresponds to the stray field gradients near the sample surface. The domain walls are therefore visible as strong black-to-white contrast variations. Large signal deviations of the MFM-frequency shift are shown with an extended color scale. We find that the domain wall signal varies considerably along the walls. These strong variations of multiple Hz along the domain walls are another sign of chirality modulation within the domain wall [157], which agrees with our findings thus far.

Besides the primary domain wall contrast, the MFM image also uncovers additional unexpected features in the form of thin, worm-like structures all throughout the sample. They have a consistent width of few tens of nanometers and are thus significantly smaller than the magnetic domains. These features are purely of magnetic origin and do not appear at all in the topographic signal. Indeed, when the magnetization direction of the major domain pattern is switched by applying a field, the contrast of the worms also inverts. This behavior can be observed in Fig. 4.9b, where the same field of view was imaged after saturating the magnetic film. Additionally, the worm contrast is stable against very high fields: The patterns remain seemingly unchanged, even after exposure to an ex-situ 7 T strong OOP-

field. We can thus conclude that these features must be related to local material properties. They are decisively not, e. g., strongly pinned trapped 360°-domain walls, as reported in [173, 174].

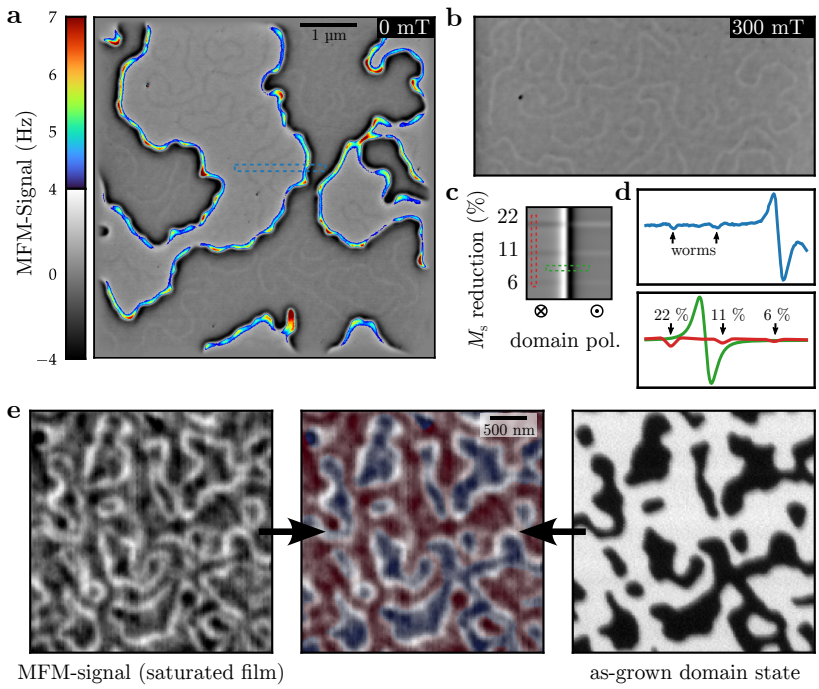

Figure 4.9 | Compositional lines in DyCo. **a** MFM-image of the demagnetized domain state. Strong black-white contrast corresponds to domain walls, while weaker worm-like contrast stems from the compositional lines. **b** Saturated state of the same film region. **c** Micromagnetic simulation of MFM-signal for a Néel domain wall and stripes of reduced M_s. **d** Comparative cross-sections of the MFM-signal found experimentally (top, blue line in (a)) and in simulations(bottom). **e** Comparison of the MFM-contrast of the saturated film (left) with the as-grown magnetic state as observed via STXM (right). The center image shows both datasets overlayed, with red-blue hue representing the STXM data and dark-bright representing the MFM-data.

We simulated the MFM contrast for lateral variations in the major magnetic parameters (A_{ex}, K_u, M_s, D) with the built-in simulation toolbox of mumax. Of these parameters, only a variation of the saturation magnetization resulted in a measurable MFM signal. Figure 4.9c shows the simulated MFM-signal for a vertical Néel domain wall and three 40 nm wide horizontal strips of reduced M_s. The contrast is qualitatively identical to the experimental data. Hence, we attribute the additional worm contrast to a local reduction in the saturation magnetization. Assuming a reduction in the saturation magnetization, the most probable explanation for such a locally reduced M_s are spatial variations of the material composition. In the following we therefore call the worm contrast *compositional lines*. Indeed, we can infer that the lines represent a local Dy enrichment: The reduction of M_s at room temperature is caused by a shift of T_M from cryogenic temperatures closer

towards room temperature. This in turn is the result of a stronger Dy-sublattice. Overall, it is important to consider that the evaluated model is not complex enough to extract quantitative information from the MFM data, which requires much more involved modeling of the probe [175]. Nevertheless, the simulations give a rough qualitative idea about the origin of the contrast.

A crucial detail is the connection between the compositional lines and the as-grown domain state. Figure 4.9e depicts the MFM-signal of the saturated DyCo film and compares it to the as-grown domain pattern. Even though the signal quality in the MFM data is not optimal due to considerable carbon deposition on the sample surface from previous x-ray imaging, the general form of the compositional lines is recognizable. Upon comparison of the MFM and STXM image, it becomes apparent that the compositional lines follow exactly the as-grown domain walls and perfectly trace the initial domain state. A second, not depicted MFM experiment on a fresh as-grown sample confirmed that as the as-grown domains collapse, they leave behind worm contrast at their original borders.

Compositional lines only exist at positions of original as-grown domain walls. Along the domain outline, however, the observed MFM signal of the compositional lines varies. We compared the chirality variations (Fig. 4.6) with the MFM-contrast (Fig. 4.9e) in the same field of view. We did not find a relation between the chirality and the MFM-signal, even though the latter should be a sign for local change of magnetic parameters. However, we must consider the degraded MFM signal quality of this particular image, which may mask an existing correlation of composition lines and chirality variations.

4.5. Discussion

4.5.1. XMLD vector imaging as an experimental tool

We have demonstrated that XMLD vector imaging can be used to reliably probe and reconstruct the domain wall chirality in rare-earth transition-metal thin films. We could realize an imaging resolution up to 15 nm, which corresponds to the diffraction limit of the used imaging setup. It is likely that significantly higher resolutions can be achieved by using specialized coherent imaging endstations that can record higher spatial frequencies. The increased photon flux and coherence from new 4th-generation synchrotrons may further help to improve image quality. Although already useful, the technique was held back by the necessity to rotate the sample for a full in-plane magnetization reconstruction. Having an x-ray source with full polarization control without ellipticity at arbitrary polarization angles is the main step to fully unlock the potential of the imaging technique. When applied to samples that exhibit stronger XMLD, or at lower temperatures where the XMLD in rare-earth transition-metal alloys generally is stronger [161], a high

throughput of samples for fast chirality determination should be achievable. Using XMLD vector imaging also in combination with novel techniques like ptychography [176] would combine quantitative scanning of large field-of-views with the high resolution of coherent imaging techniques.
With improved SNR it also becomes viable to utilize more complex physical descriptions to model the x-ray transmission. By not only determining the maximum absorption angle but also the amplitude of the angle dependent absorption modulation, also three-dimensional textures inside the walls could become reconstructable, including horizontal Bloch lines and flux closure domain walls. For full three-dimensional imaging of complex structures, techniques like tomography [177, 178] and laminography [179, 180] are still necessary. Nevertheless, XMLD-vector imaging has the potential to be a faster and easier complementary technique, because – in contrast to tomography and laminography – it is not strictly necessary to rotate the sample, which greatly reduces the complexity of the sample-stage design. Additional benefits are the faster acquisition, the robust data analysis, and the possibility to deploy the technique even in complex sample environments.

4.5.2. Lateral variations of chirality and composition

In our samples we found strong lateral domain wall chirality variations. We have seen in simulations that such variations can be caused by lateral changes of the DMI or the saturation magnetization. However, the simulations predict a considerable spread of M_s for Bloch and Néel sections in the same domain wall, for which we do not find strong evidence in the MFM signal. Therefore, either lateral variations of the DMI strength or considerable in-plane anisotropy terms are likely necessary as well to achieve such strong chirality variations.
We furthermore observed worm-like MFM contrast modulations, which – based on our current knowledge – we connect to lateral compositional variations that intriguingly are present exactly along the as-grown domain walls. As these variations are present even in pristine samples, they must have formed during sample growth. The question remains whether the compositional lines influenced the formation of the as-grown domain state or the other way round.
The compositional lines appear to act as pinning sites for domain walls, as after field cycling domain walls prefer to form where they are present. Therefore, one could assume that the compositional lines appeared first and then acted as natural boundaries that imprinted their position in the later emerging magnetic domains. However, it appears more likely that the domains where present first, following a thought experiment: If the compositional lines were present first, we would expect to see instances where during the establishment of the as-grown magnetic state two domains with the same OOP magnetization direction merged at such a pinning site. The result woud be a compositional line inside an as-grown domain and without an accompanying domain wall. Because we find compositional lines exclusively at the

as-grown domain walls, such domain-merging phenomena did not occur. Hence, it is likely that the domains were present first and, in some way, imprinted their texture onto the material properties.

It remains to be investigated whether it is possible to engineer the compositional lines and to control their emergence. Because not all DyCo-samples showed the compositional lines, some growth parameter needs to exist that determines whether the compositional lines appear. Possible, yet unexplored parameters include the deposition rate, the base and partial argon pressure, and fine-tuning of the material composition. The appearance of compositional lines can likely be inhibited by suppressing the as-grown domain state, e. g., by growing the magnetic material within an applied magnetic bias field. At the same time, it might be possible to take advantage of the interdependence between the domain state and the local composition: As discussed in chapter 1, nanometer engineering of magnetic properties is an emerging field. In chapter 6, we focus on the local modification of the magnetic anisotropy. By artificially enforcing a specific domain pattern during the material growth in the spirit of magnetolithography [181], the controlled creation of microscopic patterns of reduced saturation magnetization might be possible in the long term.

To conclude, by utilizing our newly developed XMLD-based vector imaging technique, we have found strong spatial chirality changes along domain walls in DyCo thin films. As these chirality variations are caused by variations in the material properties, the challenge remains to pinpoint which material property is fluctuating and predominately causing the chirality variations.

Particularly puzzling are the newly discovered compositional lines. It is essential to identify and verify the underlying mechanism connecting them to the as-grown domain wall positions and local domain wall chirality. In particular, the origin of the compositional lines needs to be discovered. The significance of our findings is underlined by recent developments with Dy and Co based multilayer systems, grown in another chamber, which indicate that the emergence of compositional lines may very well be a general phenomenon that is not restricted to few special films, but appears in a variety of RE-TM sample structures.

Chapter 5
Defects in magnetic domain walls after single-shot all-optical switching

†Helicity-independent all-optical switching (HI-AOS) is the fastest known way to switch the magnetic order parameter. While the switching process of extended areas is well understood, the formation of domain walls enclosing switched areas remains less explored. Here, we study domain walls around all-optically nucleated magnetic domains using x-ray vector spin imaging and observe a high density of vertical Bloch line defects. Surprisingly, the defect density appears to be independent of optical pulse parameters, significantly varies between materials, and is only slightly higher than in domain walls generated by field cycling. A possible explanation is given by time-resolved Kerr microscopy, which reveals that magnetic domains considerably expand after the initial AOS process. During this expansion, and likewise during field cycling, domain walls propagate at speeds above the Walker breakdown. Micromagnetic simulations suggest that at such speeds, domain walls accumulate defects when moving over magnetic pinning sites, explaining similar defect densities after two very different switching processes. The slightly larger defect density after AOS compared to field-induced switching indicates that some defects are created already when the domain wall comes into existence. Our work shows that engineered low-pinning materials are a key ingredient to uncover the intrinsic dynamics of domain wall formation during ultrafast all-optical switching.

5.1. Introduction

Switching of order parameters is a critical aspect of both current and emerging information technologies, with applications in data storage and logic operations due to its ability to toggle between binary states [182–185]. Examples for such order parameters include ferroelectric polarization and the magnetization of ferro- and ferrimagnetic materials. The magnetization is particularly interesting, as magnetic materials can be engineered to maintain switched states persistently without degrading the host material, allowing for virtually unlimited consecutive switching cycles. Consequently, substantial research efforts are directed towards

understanding the fundamental limits of switching speed, energy efficiency, and reproducibility. Notable examples include investigations of switching field distributions in hard drives and switching current distributions in magnetic random access memory (MRAM) devices [186, 187]. Across these research areas, defects emerge as a central theme, encompassing defects in the host material but also intrinsic defects of the order parameter itself, such as defects in magnetic domain walls. From an applications perspective, domain wall defects are generally undesirable as they introduce stochasticity to switching dynamics and compromise the long-term stability of switched states. However, these defects can also serve as valuable indicators of underlying switching mechanisms and provide insight into switching dynamics. Therefore, it is important to study the creation of defects in domain walls, particularly following ultrafast excitation.

Switching processes and the involved defect creation are best understood in the framework of phase transitions. First-order phase transitions follow a nucleation and growth model [188], exemplified by magnetic field switching via domain nucleation and subsequent driven domain wall motion, where nucleation and pinning occur at material inhomogeneities. These processes are thermally activated (following Arrhenius behavior) and therefore stochastic in nature. In contrast, second-order phase transitions, such as heat-induced transitions or continuous rotation of order parameters, can in principle enable homogeneous switching via the transient vanishing of the order parameter. In practice, however, extrinsic effects like material inhomogeneities and pinning lead to spatial modulation of the switching dynamics. Additionally, even in perfect materials, defects may emerge if symmetry breaking is present, as multiple different emerging states that are energetically degenerate (such as clockwise and counterclockwise Bloch chirality in magnetic domain walls) have the same probability to emerge.

This phenomenon has been formalized as the Kibble-Zurek mechanism, which states that areas of the same sample must choose their order parameter orientation independently if their distance is larger than information can propagate during the phase transition [189, 190]. At the boundaries of mismatching areas, defects may form. The size of these areas, and therefore the defect density, depends on the speed of information propagation (magnon propagation in magnetism) and crucially on the speed of the phase transition. Kibble-Zurek-like defect generation behavior has been observed in both magnetic [191] and ferroelectric material systems [192, 193] and primarily comes into play in ultrafast switching processes.

Helicity-independent all-optical switching (HI-AOS) is a prime example for ultrafast order parameter switching [29, 85]. HI-AOS occurs predominantly in ferrimagnetic Gd-containing rare-earth transition-metal alloys, where a single femtosecond to picosecond laser pulse switches magnetization within picoseconds [194], representing the fastest known way to switch magnetization. While the dynamics are well understood in the macro spin picture, where lateral variations and dynamics

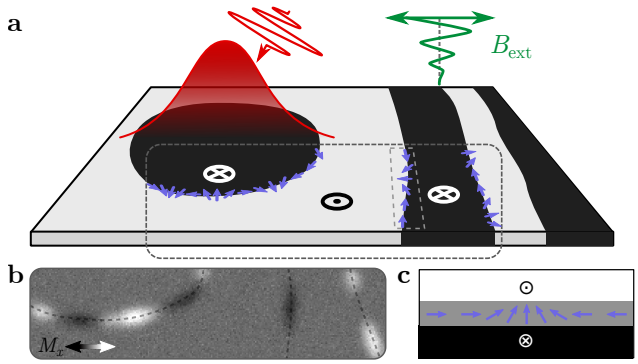

Figure 5.1 | Schematic of the performed AOS domain wall imaging experiment. **a** The domain wall defect structure of optically nucleated bubble domains and stripe domains created by in-plane field cycling is investigated. **b** Expected XMCD x-ray absorption contrast along the domain walls for a tilted measurement geometry and difference imaging, corresponding to the magnetization configuration shown above. **c** Schematic top view of the magnetization structure of a single vertical Bloch line domain wall defect.

are neglected and the sample is described as a singular coherent magnetization vector, recent investigations have revealed that the switching may also have a spatial component [86, 87, 93, 95]. Graves et al. found that ferrimagnetic alloys exhibit significant composition modulations on the nanometer scale, which leads to transversal, non-local angular momentum transfer during the switching process [8]. Independent of such material inhomogeneities, order recovery after optical excitation was also shown to involve spatially inhomogeneous transient localization and coalescence of magnons, mediated by strong non-local spin currents [81]. So far, however, the vast majority of studies do not consider the role of the boundary surrounding the switching area, hence its domain wall.

This chapter aims to investigate the creation dynamics of such all-optically created domain walls. As discussed in section 2.2, in a domain wall the magnetization $\mathbf{M}$ performs a gradual rotation from one fully out-of-plane magnetized *up* to *down* state via a fully in-plane intermediate configuration $\mathbf{M} = (\sin(\psi), \cos(\psi), 0)$ that is defined by the domain wall angle ψ. When a finite-sized area of the initially homogeneously magnetized film is switched, a domain wall is created. During the formation of the domain wall, the in-plane component of the order parameter transitions from zero to a finite value, which can in principle be considered a second-order phase transition on its own. Unless strong DMI imprints a certain chirality on the domain wall, the two possible Bloch chiralities are energetically degenerate, which leads to spontaneous symmetry breaking in the domain wall angle and creation of domain wall defects (vertical Bloch lines) during the creation process [6]. It remains unknown on what time- and length-scales the initial in-plane order is established and how the domain wall forms. As it is unfeasible to study the ultrafast, stochastic creation process of the internal domain wall magnetization structure

directly in time-resolved experiments, the final state domain defect pattern is the most accessible observable that can provide insight into the involved mechanisms. Here, we use x-ray vector imaging to investigate the domain wall structure and domain wall defect density after all-optical switching and laser-induced demagnetization, as well as field cycling (Fig. 5.1a). A high density of Bloch line defects is observed across all excitation schemes (Fig. 5.1b,c). Importantly, we find an almost negligible difference in the defect density when comparing different excitation methods and parameters in the same sample, which is unexpected in the framework of the Kibble-Zurek mechanism: Different excitation pulse lengths should in principle change the speed of the transition by altering the delay between switching of the rare-earth and the transition-metal element [95, 194] and thereby affect the defect density. By comparing optical defect nucleation in materials with different pinning with time-resolved Kerr microscopy data and micromagnetic simulations, we find evidence that post-nucleation the domain wall accumulates defects by moving over magnetic pinning sites. The dominance of this additional extrinsic defect nucleation process would then mask defects that are intrinsically created by the phase transition itself.

5.2. Materials & Methods

5.2.1. Materials

†X-ray imaging experiments were conducted on Ta(3 nm)/GdFe(20 nm)/Pt(3 nm) and Ta(3 nm)/GdFe(20 nm)/Ta(3 nm) samples, sputter-grown with nominally identical GdFe alloy layers on x-ray transparent SiN-membranes. Both samples have perpendicular anisotropy and exhibit HI-AOS. The variation in capping materials, Ta and Pt, is motivated by the frequent use of these materials in spintronics applications; sizable spin-orbit interactions, such as interfacial anisotropy or Dzyaloshinskii-Moriya interaction, are not expected to emerge from these interfaces in the present case due to the large thickness of the magnetic film. This is confirmed later by the lack of a preferred chirality in the domain walls.

†Temperature-dependent measurements of the out-of-plane magnetic coercivity H_c, as shown in Fig. 5.2a, yield the magnetization compensation temperature T_M of the materials. Both materials compensate above room temperature, at slightly different temperatures of 323 K (Ta/GdFe/Pt) and 370 K (Ta/GdFe/Ta). We use the compensation temperature as a sensitive indicator of the actual composition of the magnetically active layer. Specifically, by interpolating composition-compensation-temperature graphs from literature [195], we reconstruct the compositions of the GdFe layers as $Gd_{0.255}Fe_{0.745}$ for the Ta/GdFe/Pt sample and $Gd_{0.259}Fe_{0.741}$ for the Ta/GdFe/Ta sample. The slight difference in composition is likely caused by diffusion of Gd into the Pt capping layer [196].

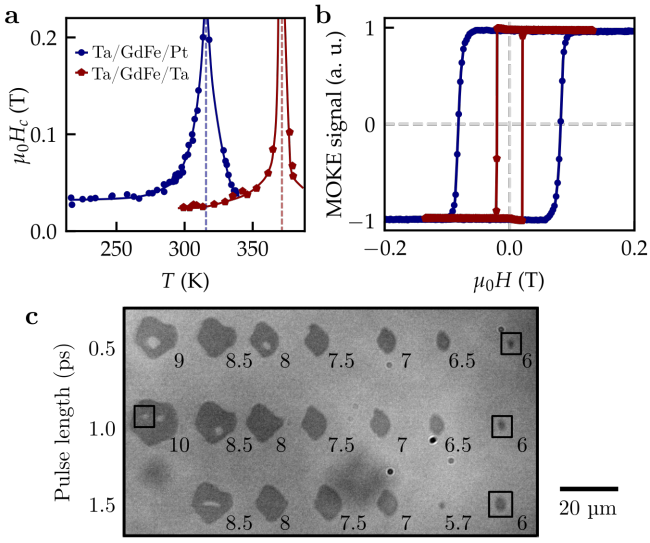

Figure 5.2 | Magnetic material properties and preparations. **a** Coercive field vs. temperature, acquired by zero-offset Hall-transport measurements. The estimated compensation temperatures are marked by the dashed lines, solid lines are guides to the eye. **b** Room temperature hysteresis curves recorded with MOKE. **c** Kerr microscopy image of laser-nucleated domains in Ta/GdFe/Pt. The laser pulse energy for each bubble is given in arb. units. Gray contrast corresponds to out-of-plane magnetization. Marked bubble domains were imaged with STXM.

†The main difference between the two samples is in their magnetic pinning. Specifically, Ta/GdFe/Ta shows a sharp, square hysteresis loop at room temperature (Fig. 5.2b), indicating that switching at the coercive field $H_c = 20\,\mathrm{mT}$ is dominantly nucleation-limited. That is, the nucleation threshold of domains is above the pinning-threshold required to move domain walls. In contrast, Ta/GdFe/Pt shows a smoother field induced transition and a higher coercivity of $H_c = 82\,\mathrm{mT}$. The more roundish shape of the hysteresis loop of Ta/GdFe/Pt indicates that domains nucleate at low fields but remain pinned until the field exceeds the depinning field. Notably, in either sample, the motion of domain walls takes place primarily at the coercive field, and for both samples this driving field during field cycling is above the Walker breakdown field expected for materials with low DMI [1].

5.2.2. Preparations

†Bubble domains were created with single shots of a linearly polarized, 1030 nm wavelength fiber laser in the initially uniformly out-of-plane magnetized film of both samples. Multiple laser fluences and temporal pulse widths above and below the AOS-threshold [87] were chosen, such that all-optically switched domains of varying size and also demagnetized bubble domain clusters were created (Fig. 5.2c). Very small switched domains below a sample-specific size threshold collapsed spontaneously within milliseconds to seconds after nucleation (as observed in similar

setups [194]). The laser fluence was therefore increased such that domain sizes were above the collapse threshold. These nucleated domains were extraordinarily stable; no change in shape was observed between nucleation and x-ray imaging experiment. Even one year later, the domains still proliferated with their original shape.

†We investigated the asymmetric Ta/GdFe/Pt sample also in a demagnetized state, achieved by cycling an in-plane field with decreasing amplitude, which resulted in stable, more than 100 µm wide stripe domains.

5.2.3. XMCD vector spin imaging

†Magnetic images were recorded by scanning transmission x-ray microscopy (STXM) at the MAXYMUS endstation of the BESSY-II synchrotron [120] with an instrument-limited spatial resolution of 25 nm (full width at half maximum, FWHM). Magnetic contrast was obtained using the x-ray circular magnetic dichroism (XMCD) at the Gd M_5 absorption edge (1184 eV). This method is sensitive to the component of Gd sublattice magnetization that is collinear to the x-ray beam. To gain vector spin information, we imaged the sample under various tilt and rotation angles, as illustrated in Figure 5.3. Specifically, the samples were tilted by $\pm 30°$ along the vertical axis (where the $-30°$ tilt was realized by rotating the sample 180° around the out-of-plane axis, see appendix A.3) and further rotated by 90° around the out-of-plane axis. At each set of angles, we recorded images with sizable XMCD contrast, see Fig. 5.3a. The sums and differences of a set of effectively $\pm 30°$ tilted images yield the components of the normalized magnetization $\boldsymbol{m}$ along the in-plane (x,y, comp. Fig. 5.3b) and out-of-plane (z) directions of the sample, respectively. By combining them all, we obtained full vector spin images (Fig. 5.3c). In these full reconstructions we find high densities of vertical Bloch line defects (points of chirality reversal, i.e., 180° rotations of the in-plane magnetization in the domain wall), but no generally preferred domain wall chirality. Note that this technique works particularly well for our materials since the domain wall width (measured to be roughly $\pi\Delta = 60$ nm, see appendix) is larger than the achieved spatial resolution ((44 ± 3) nm in our data, see appendix A.3).

†In practice, we realized that vertical Bloch line defects are already visible in single in-plane-component images (Fig. 5.3b), where they manifest as black-to-white transitions on length scales where the domain wall itself is approximately straight. To optimize time usage at the synchrotron experiment, we therefore omitted the 90° rotation in most cases and henceforth present images of a single in-plane component.

†All raw images analyzed in our study are presented in Fig. 5.4. Some sections of the domain walls could not be reconstructed using our method and are marked with dashed lines in Fig. 5.4. These sections – comprising at most 20 % of any imaged domain wall – either have a signal that is too weak to analyze, or exhibit

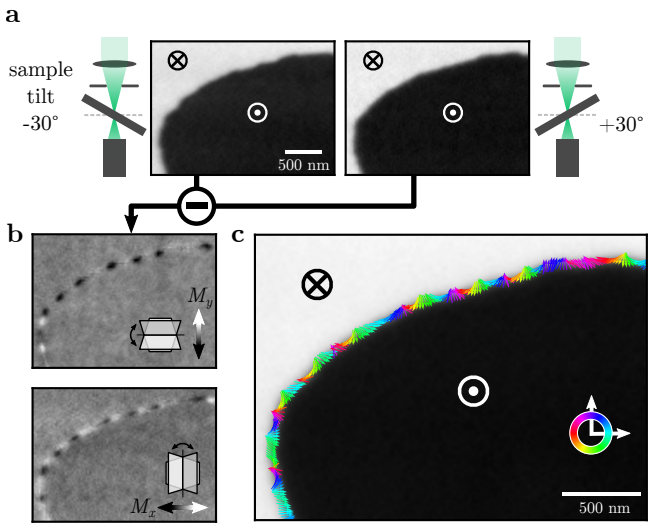

Figure 5.3 | XMCD vector imaging and reconstruction. **a** STXM-images of a domain wall section, recorded with circular polarized x-rays for ±30° effective sample tilt. **b** In-plane components derived from the difference contrast of both tilts. Insets indicate the respective sample tilt directions. **c** Vector reconstruction of the domain wall magnetization shows rapid spatial rotation of the in-plane component.

black-to-white contrast variations perpendicular to the wall which do not align with the expected patterns illustrated in Fig. 5.1. The unusual contrast in these sections may originate from an exceptionally high density of vertical Bloch lines with separations below our imaging resolution. However, simulations indicate that this contrast could also stem from membrane wrinkling (see Fig. A.5 in appendix A.3). Given the lack of conclusive data on defect density within these sections, we excluded them from our analysis. Note that this exclusion has minimal impact on our statistical analysis, as more than 86 % of the total domain wall length exhibits clear black-white contrast modulations, enabling us to resolve the local in-plane magnetization of the domain walls and, consequently, the defects within them. Also note that for circular domains, this method overestimates the total number of vertical Bloch lines by two (see, e. g., Fig. A.5 in appendix A.3). However, since we observe more than 28 vertical Bloch lines in each bubble domain, the impact of this effect is negligible for our study.

5.2.4. Time resolved Kerr microscopy

†Time-resolved data of the all-optical switching process was recorded with wide-field Kerr microscopy. We used a Ta(3 nm)/$Gd_{22}Fe_{72.2}Bi_{5.8}$(20 nm)/Ta(3 nm)-sample with added Bi for an enhanced Kerr-rotation angle [197]. The setup consisted of a custom-built epi-illumination microscope [134] with a 250 fs pulsed laser optical excitation at $\lambda = 1030$ nm as well as the time-delayed probe illumination at $\lambda/2 = 515$ nm (compare Fig. 3.7). Images were recorded at 1 kHz pump-probe

repetition for probe delays between −15 ps and 1 ns. To reset the magnetic film between pump-probe events, a static magnetic field above H_c was applied in the out-of-plane direction. For each delay, images with and without the excitation pulse were recorded and subtracted from one another. Contrast was normalized against the final state image, assuming that the nucleated domain is fully "up"-magnetized, while the material far away is "down"-magnetized. To remove high frequency image noise, a spatial Gaussian filter with standard deviation $\sigma = 200\,\mathrm{nm}$ was applied to each image.

5.2.5. Micromagnetic simulations

†We performed micromagnetic simulations to support our experimental observations to model how material inhomogeneities enable the creation of Bloch line defects during field-induced domain wall propagation. We used mumax3 [168] to simulate a 50 nm thick magnetic film with exchange stiffness $A_{ex} = 7\,\mathrm{pJ/m^3}$, saturation magnetization $M_s = 198\,\mathrm{kA/m}$, and perpendicular anisotropy $K_u = 97.5\,\mathrm{kJ/m^3}$, which were experimentally determined for a comparable DyCo-film of the same material family. The simulated area of $3000\,\mathrm{nm} \times 3000\,\mathrm{nm} \times 50\,\mathrm{nm}$ was spatially discretized into cells of size $3\,\mathrm{nm} \times 3\,\mathrm{nm} \times 50\,\mathrm{nm}$. For the Gilbert damping we chose a generic value of $\alpha = 0.5$.

†To simulate pinning within the material, the simulation area was divided into grains with an average size of 100 nm. Each grain was assigned a local anisotropy that randomly deviates from the mean in a Gaussian distribution of width σ_{K_u}. We modeled the pinning strength by varying σ_{K_u} between $1\,\mathrm{kJ/m^3}$ and $25\,\mathrm{kJ/m^3}$.

†Each individual simulation for a specific set of pinning strength and driving field proceeded as follows. First, a single defect-free Bloch skyrmion was placed within the inhomogeneous material and relaxed to an initial stable state. Next, an out-of-plane field was applied that favors the magnetization direction within the skyrmion. The system was allowed to evolve for 15 ns or until the domain expanded to a volume of 25 % of the simulation space. Finally, the magnetic field was removed again and the relaxation dynamics were simulated until the system reached equilibrium.

5.3. Results

†Our main observations are summarized in Fig. 5.4, where we show images of magnetic domain walls after all-optical switching, laser-induced demagnetization, and magnetic field cycling in our materials. All recorded XMCD difference images show strong in-plane contrast variations within the domain wall, corresponding to vertical Bloch line domain wall defects. Defects are present in both samples and for all nucleation methods and parameters. We measured the distance between

consecutive domain wall defects in each imaged domain wall. We find that the defect density is not constant along any domain wall. Instead, we observe sections with densely packed defects but also defect-free domain wall sections, seemingly without preferential direction.

†We studied the defect density in bubbles created by various laser pulse durations and intensities in Ta/GdFe/Pt. Surprisingly, we did not find any evident excitation parameter dependence (see appendix A.3). In consequence, we combined all of these data sets into a single histogram of the distances d between neighboring defects (Fig. 5.4a). The distribution shows a prominent peak that can be well described by a Γ-distribution. The count of observed distances drops to zero at 50 nm, the realized imaging resolution in the experiment.

†We use the fitted peak position as the measure for the characteristic defect distance and the reported fitting errors as the corresponding uncertainty. For optically created domains in Ta/GdFe/Pt we obtain a characteristic defect-defect distance of $d_{\mathrm{peak}} = (134 \pm 15)$ nm (Fig. 5.4a), for a field-cycling-created wall in the same sample (201 ± 93) nm (Fig. 5.4b), and for an all-optically created domain in Ta/GdFe/Ta (289 ± 84) nm (Fig. 5.4c). These peak distances are, even within their error bars, comfortably larger than the spatial resolution of the images. The same applies to the entire left-hand tail of the distributions and to the size of vertical Bloch lines in full vector spin images (Fig. 5.3c). Therefore, we are confident that our statistical analysis is valid despite the finite resolution of our images.

†We turned to time-resolved Kerr microscopy (Fig. 5.5) in search for the dynamics that could be responsible for the observed defect densities. Figure 5.5a shows multiple stages of the all-optical switching process. The initially homogeneously magnetized film is demagnetized shortly after the laser pulse hits the sample. After approximately 50 ps, the switched domain starts to form within the exposed area. The remagnetization of the material occurs first at the edges, where less heat is deposited by the laser pulse. Also, a fully connected domain wall around the switched area is first observable at this delay. The switching of the center of the domain follows subsequently. The apparent granular structure of the switched domain is experimental noise, which is also present in the data before the excitation (Fig. 5.5a at −15 ps). Due to this graininess, we cannot clearly determine whether the domain wall forms initially as a circumference of the entire bubble or as small, local segments. What we clearly see, however, is a well-defined domain wall after 50 ps which gradually expands outwards. This domain wall motion continues up to the maximum measured delay time of 1 ns, as illustrated in Fig. 5.5b. Note that expansion occurred even though the external resetting magnetic field was applied in the opposite direction.

†The domain expands on average (290 ± 90) nm between 50 ps and 1 ns. This value is considerable compared to the size of domains imaged in Fig. 5.4 and especially in comparison to the defect-defect distances and the domain wall width. The average

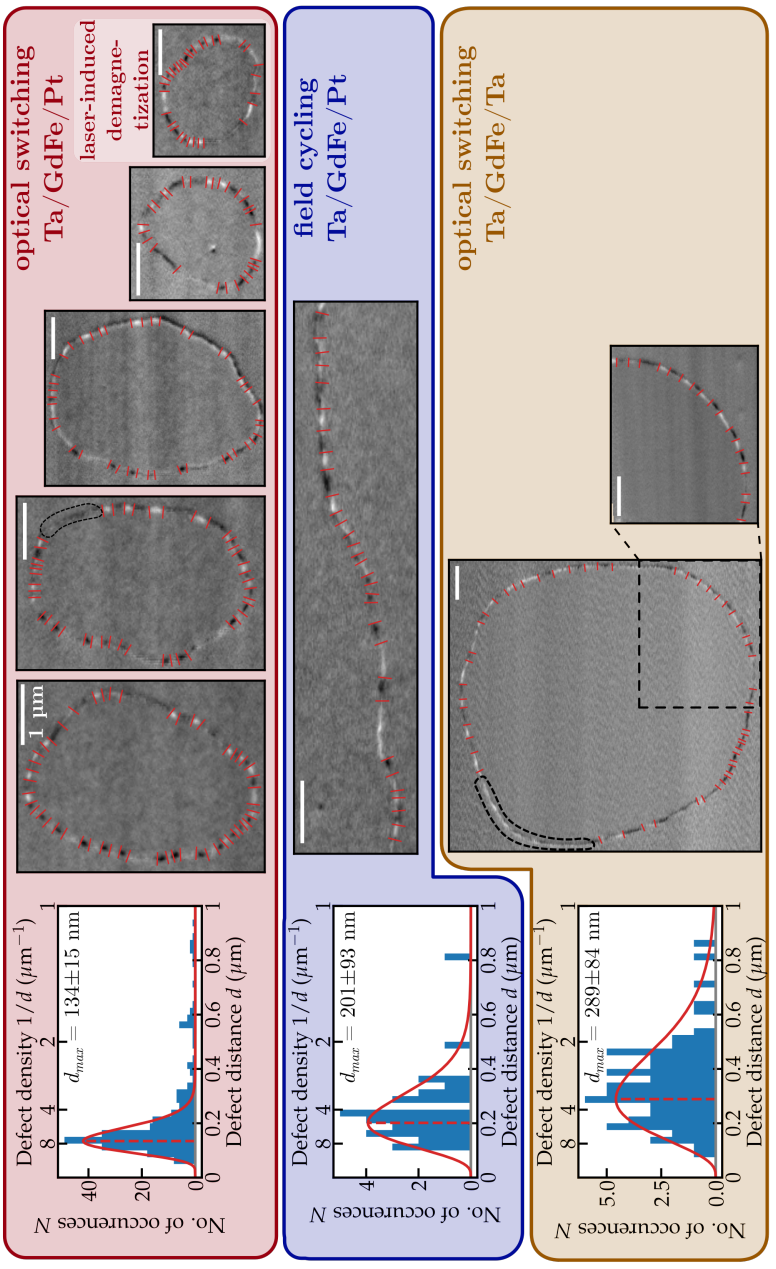

Figure 5.4 | Domain wall defect density for various nucleation channels. a Distribution of distances between consecutive domain wall defects in optically nucleated domains in Ta/GdFe/Pt (in parts highlighted in Fig. 5.2c). The histogram, the best fitting Γ-distribution and the peak position with uncertainty are depicted, as well as the original source microscopy-images. Red dashes indicate vertical Bloch lines. Because no distinct dependence of the defect density on the laser parameters was found, all laser-nucleated domains were merged into the same statistic. The same information is given for **b** a domain wall created by field cycling and for **c** a bubble domain in Ta/GdFe/Ta created by AOS. Domain wall sections marked by dashed lines highlight regions with unclear defect structure.

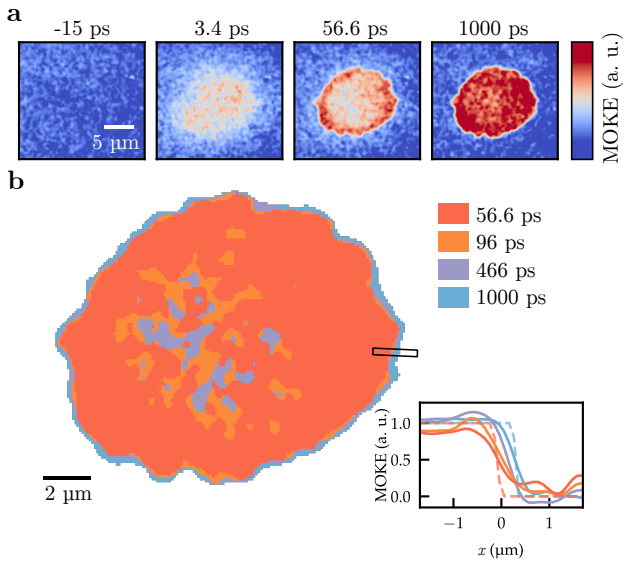

Figure 5.5 | Time-resolved Kerr microscopy of all-optical domain nucleation. a Snapshots of the nucleation process before laser irradiation, during thermal demagnetization and during the formation of the switched domain. The color scale is normalized such that the contrast at the largest delay corresponds to full negative (blue) and positive (red) magnetization. **b** Threshold of the MOKE-contrast for multiple states between the domain wall formation and the maximum recorded delay, which shows the gradual expansion of the domain outwards. The inset shows one exemplary line-scan with the Gaussian-smoothed raw data (filled lines) and the corresponding profile after thresholding (dashed lines). The threshold corresponds to $M_z = 0$, as determined in the fully demagnetized state.

domain wall velocity of $250\,\mathrm{m\,s^{-1}}$ during the expansion is safely above reported Walker breakdown speeds for comparable materials, even with finite DMI [1]. Cause for the expansion could be the laser-induced transient thermal gradient. Notably, the domain wall moves away from the hot region, which is generally unexpected, but has been observed in ferrimagnets before [198, 199].

†Micromagnetic simulations provide a model to reproduce the expansion dynamics. Instead of a thermal excitation, an external magnetic field was used as a generic driving force for the expansion. We find that the originally defect-free domain wall accumulates defects during the expansion, as shown in Fig. 5.6b. While some defects annihilate in the relaxation step, most of the Bloch lines still exist in the final state (Fig. 5.6c). Generally, a higher material inhomogeneity leads to the generation of more vertical Bloch lines and increases their stability. Moreover, we find that driving fields around and above the Walker breakdown field B_W result in a high density of defects, whereas fields far below the Walker breakdown create almost no domain wall defects. These observations are in line with previous theoretical studies that report on a critical field value above which Bloch lines nucleate during propagation [200]. Generally, this value is at or slightly below the Walker breakdown field and – in the related case of horizontal Bloch lines, which can themselves cause the creation of vertical Bloch lines [59] – depends on the local anisotropy [6]. The presence of areas with reduced perpendicular anisotropy, as in our simulation, therefore explains the Bloch line creation below the critical field value [21].

5.4. Discussion

†Our findings suggest that the domain wall defect structure after HI-AOS is at least partially influenced by post-nucleation domain wall propagation dynamics. The speed at which domain walls propagate during this post-nucleation expansion is well above the Walker breakdown velocities. Even though the exact driving forces for the domain expansion after HI-AOS are not known, the likelihood of precessional motion at such velocities is high. The simulations indicate that under such precessional motion, domain walls accumulate vertical Bloch line defects if they move over sufficiently strong pinning sites. Intuitively, we can understand this behavior by considering that local variations of the magnetic properties lead to locally different domain wall precession frequencies. The consequence is a spatial mismatch in the internal spin structure. If the mismatch becomes too large, a pair of vertical Bloch lines forms.

†The creation of defects during propagation does not exclude the possibility that some defects are already produced during the initial HI-AOS process. However, the experiments suggest that propagation-induced defects dominate in our experiments as this explains the insensitivity to the laser excitation parameters (e. g., pulse

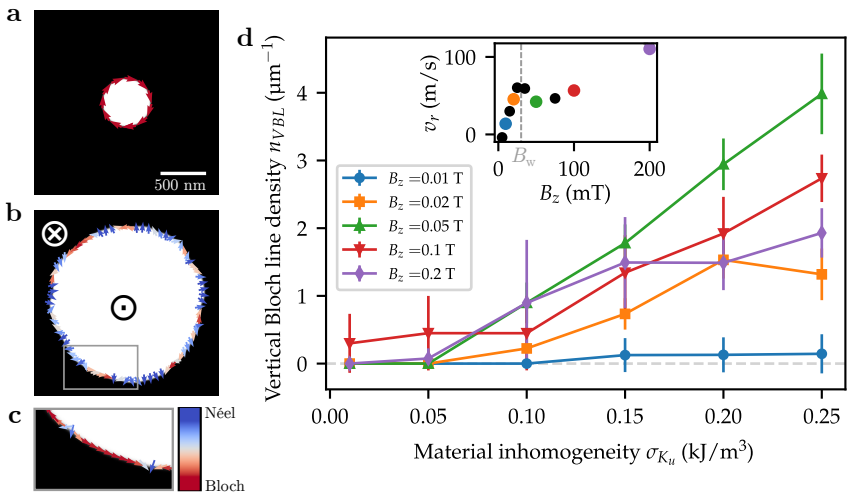

Figure 5.6 | Micromagnetic simulations of field-induced bubble-domain expansion in an inhomogeneous medium. **a** Initial homochiral Bloch domain and **b** final state bubble after field-induced expansion. **c** Bloch line defects after subsequent relaxation of the dynamic state. **d** Density of vertical Bloch line defects for increasing material inhomogeneity for various out-of-plane driving fields B_z. Each data point is the average of five simulations with randomized material inhomogeneity. The inset shows the dependence of the domain wall propagation speed on the applied driving field in a defect-free sample, with the determined Walker breakdown field.

duration and fluence), the similarity of defect densities after HI-AOS and field cycling, and the larger defect density in the higher-pinning Ta/GdFe/Pt as compared to the lower-pinning Ta/GdFe/Ta.

†The small increase in defects in optically created domain walls compared to field cycling provides a hint that some defects were present in the domain walls already at the moment of their creation. The increase is small, however, compared to the total number of present defects and lies within the uncertainty of the analysis. To properly investigate the nature of vertical Bloch line defects produced intrinsically by HI-AOS, the likelihood of defect production during post-switching dynamics must be strongly reduced. Our study suggests that the defect density in domain walls after magnetic field cycling can serve as a valuable metric in this optimization.

†To conclude, our investigation has revealed a high density of domain wall defects within domain walls produced by helicity-independent all-optical switching. We attribute their origin to post-nucleation expansion dynamics, during which the nucleated domain walls move at high speeds over magnetic pinning sites. This interpretation is consistent with the insensitivity of the defect density on the stimulus that has triggered the switching, and the dependence on extrinsic pinning in the material. Our study demonstrates that systematic investigation of defects can provide insights into the dynamics of the switching process without requiring time-resolved experiments – particularly valuable for stochastic dynamics

where stroboscopic imaging is impossible. The observed behavior contrasts with predictions based on the Kibble-Zurek mechanism, suggesting that in magnetic systems with strong pinning, post-nucleation domain wall motion dominates defect generation. More broadly, our findings illustrate how defect analysis can provide valuable perspectives on the limitations of speed, reproducibility, and stability in order parameter switching, with potential implications beyond magnetization to other switchable states, such as polarization in ferroelectrics or charge density in correlated electronic materials.

Chapter 6
Skyrmion localization dynamics after optical excitation

The nucleation of skyrmions by an ultrashort laser pulse is the fastest known way to create such topological textures. Despite their technological relevance, the involved nucleation mechanisms are still under debate. The discovery of a transient fluctuating regime during the topological phase transition suggested that the nucleation dynamics are exchange driven and laterally homogeneous. However, recent engineering developments in ion-patterned magnetic multilayers allowed for the controlled positioning of optically nucleated skyrmions, which is in stark contrast to previously reported spatially homogeneous nucleation statistics. Here, we report on the localization dynamics of optically nucleated skyrmions in magnetic multilayers. By patterning the sample with a regular grid of artificial nucleation sites, the time-resolved small angle x-ray scattering contributions of localized and non-localized skyrmions can be separated. With the support of atomistic spin dynamics simulations we can ascertain that skyrmion nuclei are homogeneously created throughout the entire film. In the subsequent cooling process the nuclei collapse or proliferate depending on the local material properties. The localization is therefore a local and decay-driven process. Surprisingly, the local skyrmion stability is described with good precision by an analytical model with room temperature parameters, providing a pathway for materials screening.

6.1. Introduction

Fundamental interactions in physics can be accessed by reaching high energies, small length scales, or short timescales. Hence, ultrafast dynamics provide a means to probe such fundamental interactions. For example, ultrafast demagnetization has revealed energy dissipation channels [27], while all-optical switching has provided insight into the complex exchange interactions between ferrimagnetic sublattices [85, 93]. Additionally, ultrafast studies of metal-insulator transitions have shed light on the interplay of lattice and electron dynamics [201].

One particularly exotic property of physical systems is their topological charge, which, as an originally mathematical concept, can have significant influence on their behavior. In magnetism, topological spin textures cannot be transformed ("combed") into a homogeneous and therefore topologically trivial ferromagnetic state without a discontinuous transition [202, 203]. In the micromagnetic framework this discontinuity gives rise to an intrinsic exchange energy penalty, which needs to be overcome in the nucleation of topological textures. This energy barrier has been coined as "topological protection" of a topologically non-trivial magnetic texture.

Magnetic skyrmions are circular bubble domains that carry topological charge. Due to their particle-like response to external stimuli, skyrmions are of great interest for spintronics applications [204], which gives the involved switching speeds and the topological energy barrier direct technological relevance. Avenues to create skyrmions in ferromagnetic multilayer systems include resistive heating [76], field cycling [149] and spin-torque pulses [151, 205]. However, the fastest known way to create a skyrmion state in such samples is by laser heating [70, 206]. The observed sub 300 ps nucleation dynamics were interpreted as the transient removal of the topological energy barrier due to a reduction of the exchange interaction and decoupling of individual magnetic layers in the stack [70]. The reduction of the fundamental exchange interaction is expected to dominate the nucleation process. In consequence, lateral variations of DMI and anisotropy should be inconsequential and nucleation should be a laterally homogeneous process. This expectation was confirmed by simulations as well as by homogeneous nucleation statistics in quasi-static imaging experiments [70]. In contrast, recent quasi-static experiments in ion-irradiated multilayers demonstrated controlled skyrmion nucleation by optical means at predetermined artificial pinning sites [16, 207]. These opposite results raise the question of when and how local material properties influence skyrmion localization during the optical nucleation process.

In this chapter, we investigate the localization dynamics of skyrmions during the optical nucleation process in a Co/Pt-multilayer with time-resolved SAXS (Fig. 6.1a). By creating a regular square grid of artificial nucleation sites (Fig. 6.1b), we can determine whether the majority of magnetic features are localized at one of these sites. Such a localized magnetization configuration applies the symmetry of the grid onto the magnetic state, which in turn results in qualitatively different magnetic x-ray scattering compared to a disordered magnetic state. The concept is illustrated in Fig. 6.1, where the simulated SAXS scattering pattern from a state of localized, ordered skyrmions (Fig. 6.1d) reflects the square symmetry of the magnetic configuration. In comparison, a non-localized magnetic state with (at most) close range order shows broad, isotropic scattering (Fig. 6.1c).

We find a delayed onset of the localization after the initial fluctuation-mediated skyrmion nucleation. Our data reveals that the localization starts approximately 300 ps after the optical stimulus, hence, after the reported nucleation time, and is

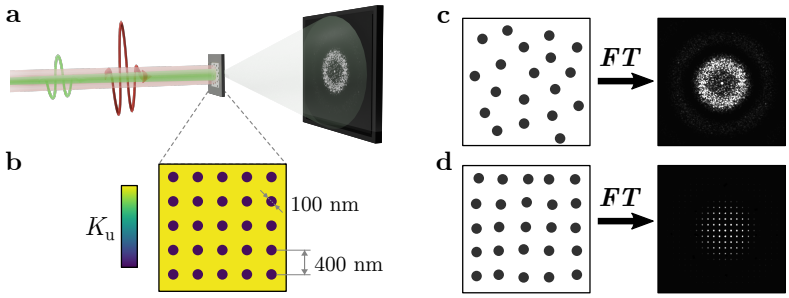

Figure 6.1 | Concept of the localization experiment. **a** Schematic of the time resolved SAXS scheme, including the optical pump, x-ray probe, sample, and x-ray detector. **b** Grid of artificial pinning sites with locally reduced perpendicular anisotropy. Qualitative difference in scattering patterns for **c** disordered and **d** ordered (hence, localized) skyrmions on artificial nucleation sites.

essentially complete after one nanosecond. Atomistic spin dynamics simulations suggest that localization is a purely decay-driven, local process: Fluctuations enable the global emergence of skyrmion nuclei, holding topological charge, in the high-temperature phase. However, these skyrmions collapse during cooldown if they are not located in a suitable environment. This way, our findings unite the current understanding of global, exchange-driven nucleation dynamics with the recent reports of localization of laser-induced skyrmions.

6.2. Sample fabrication and characterization

As a basis for this experiment we used a Co/Pt multilayer with the layer configuration SiN/Ta(3 nm)/$[$Co(0.6 nm)/Pt(0.8 nm)$]_{15}$/Ta(2 nm), which is a well-established host for optically created, stray-field stabilized magnetic skyrmions [70, 78, 208]. The Co/Pt-multilayer material was fabricated by confocal ac- and dc-magnetron sputtering at a base pressure of 6.5×10^{-9} mbar and Argon working pressure of 2.7×10^{-3} mbar on 150-nm-thick Si_3N_4-membrane chips. Layer thicknesses were calibrated with a quartz monitor prior to the deposition. 200 µm × 200 µm large x-ray transparent apertures allowed for transmission-based scattering experiments.

6.2.1. Ion irradiation

Bombardment of multilayer materials with various accelerated ions can modify the physical properties of a solid-state sample. Carefully choosing the used element, acceleration voltage and ion dose allows for modification of the topography or only the magnetic properties of a thin film. The development of focused ion beam microscopes has enabled the manipulation of material parameters on a microscopic level with the goal of creating magnetic microstructures for spintronics applications [209]. Bombarding the film with ions leads to an intermixing at

the interfaces between individual layers. Such intermixing reduces the interfacial anisotropy. The interfacial DMI is reduced in the same manner [210, 211]. Multiple studies have shown that the ion-treatment makes magnetic multilayers more hospitable for magnetic skyrmions, which has been demonstrated for He [16, 212], N [213] and Ga [214, 215] ions. Intriguing are recent studies on skyrmion confinement: By selectively irradiating small patches of material with He-ions, where the patch diameters are comparable to the skyrmion size, a preferable nucleation site for skyrmions could be established by multiple groups [14–16]. Indeed, independent of the nucleation method, for certain applied field ranges, skyrmions exclusively and repeatedly nucleate at these sites.

We chose to create such artificial nucleation sites with a focused ion beam microscope using gallium-ions (Thermofisher HELIOS 600). The maximum available ion-acceleration voltage of 30 keV was used, such that the Ga-ions penetrate through the entire material stack and modify the layers homogeneously. Due to the strong exchange coupling between individual Co-layers, we expect the multilayer material to still act as a homogeneous material along the film normal, even if the ions induce stronger intermixing in the top layers of the material stack.

We determined the most suitable ion dose by irradiating $15 \times 15\,\mu m^2$-large patches of the multilayer sample with various ion doses and characterizing the irradiated areas with Kerr-microscopy and STXM. Figure 6.2 illustrates the impact of the ions on the material: The plots in Fig. 6.2a show the OOP-hysteresis loop of two ion doses compared to the pristine, non-irradiated film. Higher irradiation doses enable spontaneous domain-nucleation at higher applied fields and also push the saturation field to higher values. Hence, the stability of magnetic domains is increased and their nucleation barrier is reduced. Additionally, the domain size decreases with increasing ion-dose (compare top-left insets in Fig. 6.2a). This is a sign for a decreasing perpendicular magnetic anisotropy, which was postulated as the main material modification in the artificial pinning sites [16]. We chose a dose of $2.3\,\text{ions/nm}^2$ for our experiment, as this dose neither altered the topography of the sample nor changed the qualitative shape of the sheared hysteresis but still substantially altered nucleation- and saturation-fields compared to the pristine material.

With the identified ideal ion dose we prepared rectangular grids of nucleation sites (henceforth called “dots”). We chose a lattice period of 400 nm between dots and a dot diameter of 100 nm (compare Fig. 6.1b). As observed in STXM, the natural mean domain width in the pristine material is roughly 175 nm and shrinks to approximately 90 nm in the irradiated areas (compare insets in Fig. 6.2a). In consequence, the magnetic structures can be comfortably localized within neighboring dots and their periodicity can be distinguished from the non-treated material. Additionally, each individual dot is only large enough to host a single

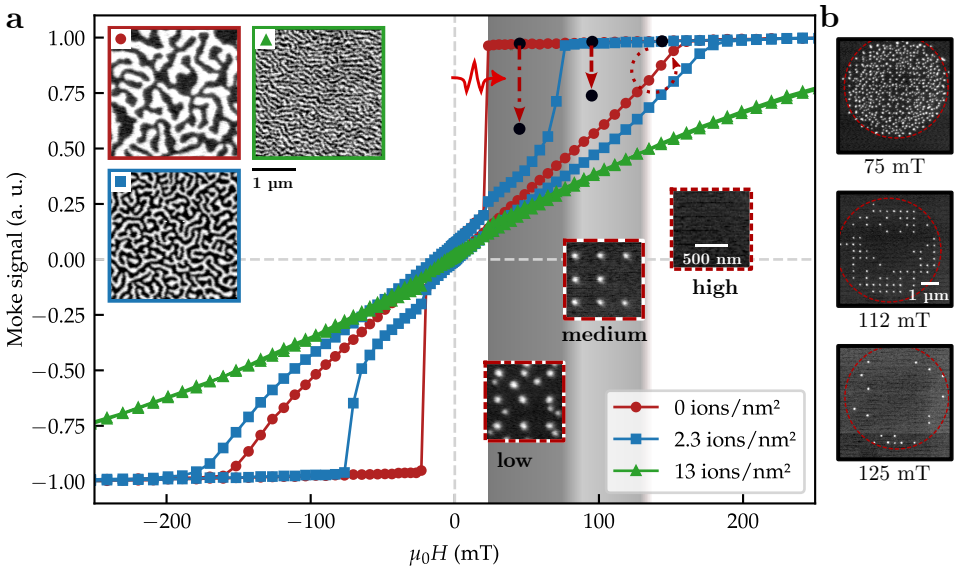

Figure 6.2 | Characterization of the irradiated sample. a Out-of-plane hysteresis loops recorded with Kerr-microscopy within $15 \times 15\,\mu m^2$-large regions of the specified Ga-irradiation dose, specifically no irradiation, the dose used in the time-resolved experiment ($2.3\,ions/nm^2$) and a significantly higher dose. Insets on the left show the domain state at 0 mT applied field for each dose. Insets on the right show the domain state in the irradiated dot-array after excitation of the initially homogeneously magnetized sample with an optical laser pulse for three regimes of applied fields. **b** Skyrmion states after single-shot laser irradiation for various applied magnetic fields. Each state was created from saturation. The dashed circle indicates the rough outline of the laser spot. Recorded with STXM.

skyrmion, assuming that the skyrmion diameter is roughly identical to the width of individual worm domains.

6.3. Quasistatic experiments

While time resolved measurements give direct insight into the dynamics of the nucleation and localization process, quasistatic experiments readily unlock information about the final states long after the excitation. In this section, we report on the magnetic domain states that result from the optical heating with an ultrashort laser pulse. We investigated the field and pulse-energy dependence of the nucleation statistics as well as the impact of the artificial nucleation sites on the topology of pinned features.

6.3.1. Optical excitation

Magnetic-field and fluence studies were performed with STXM. The sample was saturated in-situ by an OOP-field and consequently exposed to a few-picosecond

long laser pulse after reducing the applied field to a desired value. The resulting images of magnetic states are shown in Figure. 6.2.

Generally, the laser pulse leads to the nucleation of circular magnetic domains, which are assumed to be skyrmions. However, depending on the applied field, their location and density varies (compare Fig. 6.2a, insets): At low fields (30 mT up to approx. 75 mT), a dense cluster of bubble domains is created, as it is the case in the non-irradiated material without artificial sites. At high fields (> 130 mT), the final state remains homogeneously saturated. In a medium field range in-between, however, each irradiated dot is occupied by a single bubble, while the rest of the material is homogeneously magnetized. In this regime, the final, localized skyrmion arrangement after optical excitation is an almost perfectly spatially ordered magnetic state, as desired for the time resolved SAXS experiment. The three field regimes are not sharply separated. Instead, with increasing field, the density of skyrmions decreases, first in the non-irradiated areas and at higher fields also at the irradiated positions. Finally, increasing the applied field leads to a reduction of the size of the nucleated magnetic features. Note that the magnetic skyrmions in the irradiated dots are generally larger than in the pristine material. In contrast, the worm domain size decreases with the ion dose and thus exhibits the inverse behavior. Both behaviors reflect the reduction in the domain wall energy. In the case of densely packed worm domains, this allows for a reduction in the stray field, while an isolated magnetic feature can grow (as discussed in section 2.3.1).

In the STXM setup, the laser spot on the sample had a Gaussian profile with a diameter of roughly 10 µm. By imaging the entire laser-exposed area, we could observe the dependence of the nucleation statistics on the deposited heat. Irrespective of the absolute amount of deposited thermal energy, we can assume a monotonous increase in fluence towards the center of the laser excitation profile. Three example images are shown in Fig. 6.2b for the identical laser fluence but varying applied field. In general, we found a ring-like structure with lower skyrmion densities in the center of the exposed area compared to the surrounding. Right at the edge of the laser spot, we found only a few nucleated skyrmions exclusively on irradiated sites, as the deposited thermal energy is generally not high enough to nucleate domains. The density of skyrmions increases as the laser-deposited energy increases, which also includes skyrmions outside the irradiated dots. However, in the center of the laser spot, where the highest amount of energy was transferred into the material, the skyrmion density is reduced. At higher fields, the effect was more pronounced. While artificial pinning sites were occupied in regions of intermediate deposited heat, the center of the exposed area stayed bare of any magnetic texture. We confirmed that lowering the laser intensity lead to an increase of nucleated features in the center.

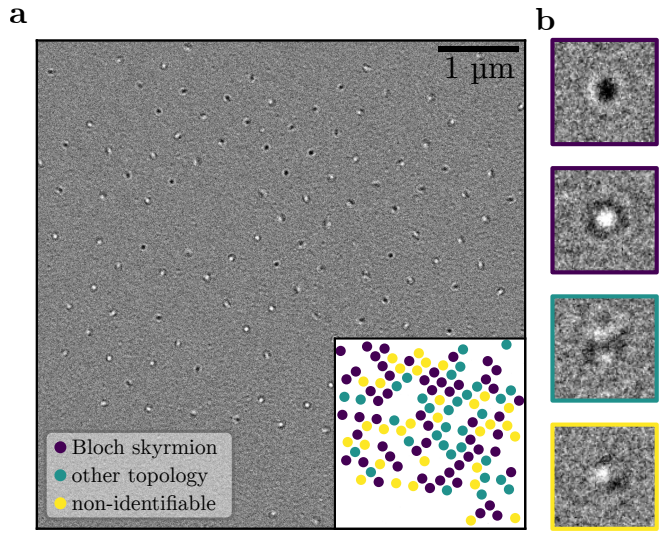

Figure 6.3 | Lorentz-TEM evaluation of skyrmion topology. a Overview image of the laser-induced bubble-domain state after saturation and subsequent laser excitation at 100 mT. The associated topology for each bubble is indicated in the inset, with each circle corresponding to one bubble domain in the main image. **b** Magnified examples for each category. The first two images show Bloch skyrmions with opposite chirality. The third image depicts a feature that is clearly not a skyrmion, while the fourth feature bears similarity to a skyrmion but does not clearly show the expected ring-like contrast.

6.3.2. Lorentz-TEM

While the STXM measurements could confirm the presence of round magnetic features on the irradiated dots, we also needed to determine the topology of the observed magnetic bubbles. While laser-heating of Co/Pt-multilayers has been observed to create clusters of Bloch-skyrmions [70], the impact of local Ga^+-irradiation on the topology of the nucleated features was not clear. Lorentz-TEM is particularly well suited to image domain walls with Bloch chirality, especially in ferromagnetic samples with large, non-compensated magnetic moments. Therefore, we performed Lorentz-TEM imaging to verify that these magnetic features on the irradiated dots were indeed skyrmions. The film was optically excited in-situ with an in-coupled laser in the microscope setup. For each applied magnetic field, the initial and final state were recorded and the difference image computed to suppress topographic charge contrast. Figure 6.3a shows the difference contrast of the magnetic state at an applied field of 100 mT, hence, a value where magnetic features exclusively nucleate on the irradiated dots. Topology classification of the nucleated magnetic bubbles was performed fully manually (i. e., by examining each feature and comparing to the expected contrast [146, 216] for a Bloch type skyrmion and deciding whether the similarity is high enough).

Our samples were grown on x-ray transparent membranes that are not specially prepared for TEM imaging. Together with the significant amount of platinum within the sample itself, imperfections in the membranes caused a significant topography signal, which still persists in the signal even after background subtraction. Due to the remaining background signal, the topology of some magnetic textures was hard to determine. Each magnetic domain was therefore classified as one of three options: As a Bloch-skyrmion, a non-topological bubble domain or as a magnetic feature with non-identifiable topology. Examples for each feature class are shown in Fig. 6.3b. The classification for each bubble domain is depicted in the inset of Fig. 6.3a. Of all features, the topology of 29 % remains unknown and a rigorous investigation would require regrowing the sample on specialized TEM-substrates. Of the remaining magnetic bubbles, (63 ± 10) % match the Lorentz-TEM signal of a Bloch skyrmion, while the rest clearly has a different (usually trivial) topology. The estimated error takes the uncertainty into account that stems from the unidentified bubbles, assuming that the ratio of skyrmions to non-topological features is the same.

The significant amount of non-topological bubble domains specifically on the irradiated dots is unexpected, as the pristine film reportedly hosts exclusively skyrmions after laser excitation [70]. Also, we need to interpret the time-resolved SAXS experiments with the knowledge that during the nucleation process both species of bubble domains emerge. Nevertheless, the majority of nucleated and localized bubbles are in fact skyrmions, making the sample a suitable system to study their dynamics.

6.4. Time resolved SAXS

6.4.1. Setup & experiment

The main scattering experiment was performed at the SCS-beamline at the European XFEL facility in Hamburg, Germany. An illustration of the setup is depicted in Fig. 6.4a. Scattering patterns were recorded on a PiMTE3 in-vacuum CCD detector equipped with a wire-mounted beamstop to block 0th-order transmission. An electromagnet was used to apply magnetic fields and in-situ restore the saturated magnetic state before each pump-probe event. The intensity of the x-ray probe pulses was adjusted with a gas attenuator such that the pulse did not perturb the magnetic state of the sample. We determined the x-ray perturbation threshold by recording SAXS hysteresis loops at varying FEL-intensities, where intensities above the threshold lead to a shift of the spontaneous nucleation field towards higher values (compare appendix A.5).

In prior experiments we had observed that the XFEL showed strong pulse-to-pulse variation of the Poynting vector. Averaging the scattering patterns of many pulses

lead to an effective reduction in coherence. To reduce the spatial jitter of the FEL, an up-stream circular aperture was introduced. Only a small, coherent portion of each FEL pulse was transmitted through and scattered at the aperture. The resulting Airy disk pattern at the sample position was then solely defined by the aperture. As trade-off, the intensity variability of pulses on the sample as well as the illuminated sample area increased. For the excitation we used an optical pulsed fs-laser ("OL") with a central wavelength of $\lambda = 800\,\mathrm{nm}$ and pulse length of $\tau \approx 50\,\mathrm{fs}$), which was synchronized to the FEL-pulse delivery with an adjustable delay. We observed spatial jitter between consecutive pulses much stronger than the FWHM of the laser spot itself, which lead to strongly varying intensities on the probed part of the sample. To monitor the spatial OL-jitter we installed a secondary camera to record a virtual image of the laser spot during each excitation for later sorting and classification of the data.
Time resolved data was recorded with a conventional stroboscopic pump-probe scheme, with each cycle consisting of the following steps (compare Fig. 6.4b):

1. The electromagnet applies a magnetic field of $B_{\mathrm{reset}} = 300\,\mathrm{mT}$, which is comfortably above the saturation field of the sample, to reset the magnetic state to a homogeneous OOP-magnetization.

2. The magnetic field is reduced to the value B_{meas}, for which we want to record a pump probe event.

3. The OL is triggered and excites the magnetic material to start the skyrmion nucleation process.

4. A singe FEL pulse hits the sample after a delay τ and is scattered at the magnetic contrast, which is recorded on the detector.

5. The camera starts the readout of the recorded scattering information and prepares the sensor for the next acquisition. Meanwhile, steps 1 and 2 are performed to prepare for the next pump-probe cycle.

To ensure proper synchronization to the 10 Hz logic of the FEL facility, the duration of one complete pump-probe cycle was set to 0.3 s, with the majority of the time being dedicated to magnet cycling and the synchronization of individual triggers. Each pump-probe event was recorded roughly 2000 times and each event stored separately (in contrast to accumulating multiple events into one frame before triggering the readout of the camera) for the subsequent separation of frames where the local fluence of the OL was not strong enough to excite the sample fully.
The position of the pump laser spot on the sample was monitored by recording the partial reflection of the laser on the vacuum-incoupling window at the virtual sample position. Quasi-static data of the final states was recorded with the same pump-probe logic. However, the number of x-ray pulses per bunch was increased

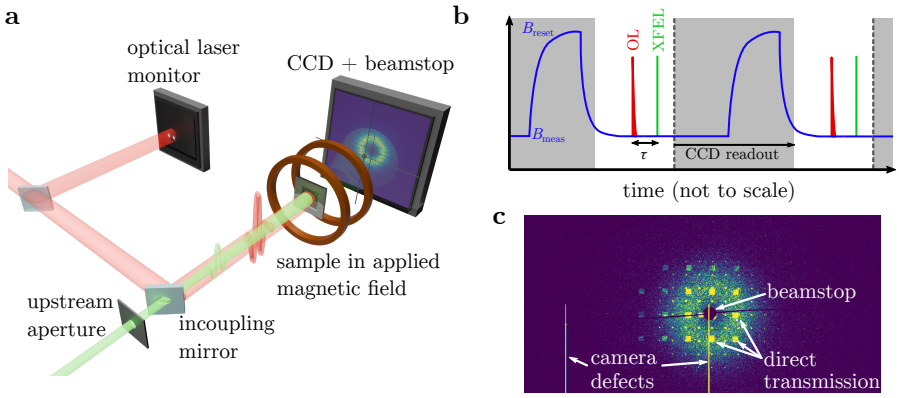

Figure 6.4 | Experiment procedure for time resolved SAXS. a Sketch of the idealized experimental setup. **b** Utilized control scheme to record time-resolved data. After resetting the magnetic state at B_{reset} and consequently reducing the applied field to B_{meas}, the optical pump and x-ray probe pulse hit he sample with the specified time delay τ. **c** Example of a final state CCD-exposure, showing magnetic scattering but additionally undesirable artifacts that need to be removed in post-processing.

to 48, which lead to a corresponding 48 times stronger signal on the camera for each cycle.

6.4.2. Data treatment

We recorded time resolved SAXS data for three applied magnetic fields B_{meas}, with each corresponding to one of the three field regimes introduced in section 6.3.1. In the following, the applied fields of 65 mT, 115 mT and 165 mT will therefore be referred to as *low*, *medium* and *high* applied magnetic field. An exemplary out-of-camera CCD-frame is shown in Fig. 6.4c. The signal consists of multiple components: On one hand, the magnetic signal, divided into isotropic (often ring-like) scattering from disordered magnetic features and a grid of Bragg-scattering-like dots from magnetic features with long-range order. On the other hand, parts of the scattering are covered by camera defects, the beamstop shadow and multiple bright, square spots. The latter are direct transmission of x-rays through neighboring membranes, caused by the large spot size due to the widening of the FEL by the upstream aperture. Figure 6.5 shows SAXS images for various pump-probe delays at the three chosen magnetic field values. The following post-processing steps were applied to the data shown.

Adaptive thresholding: In each individual pump-probe CCD frame, large areas were not exposed to any photons. Especially at high q scattering statistics are low and the recorded signal mostly consists of single photon events, while for the majority of frames, most pixels do not record a photon. If no photon is recorded, these areas of the frame only contribute thermal readout noise to the final image

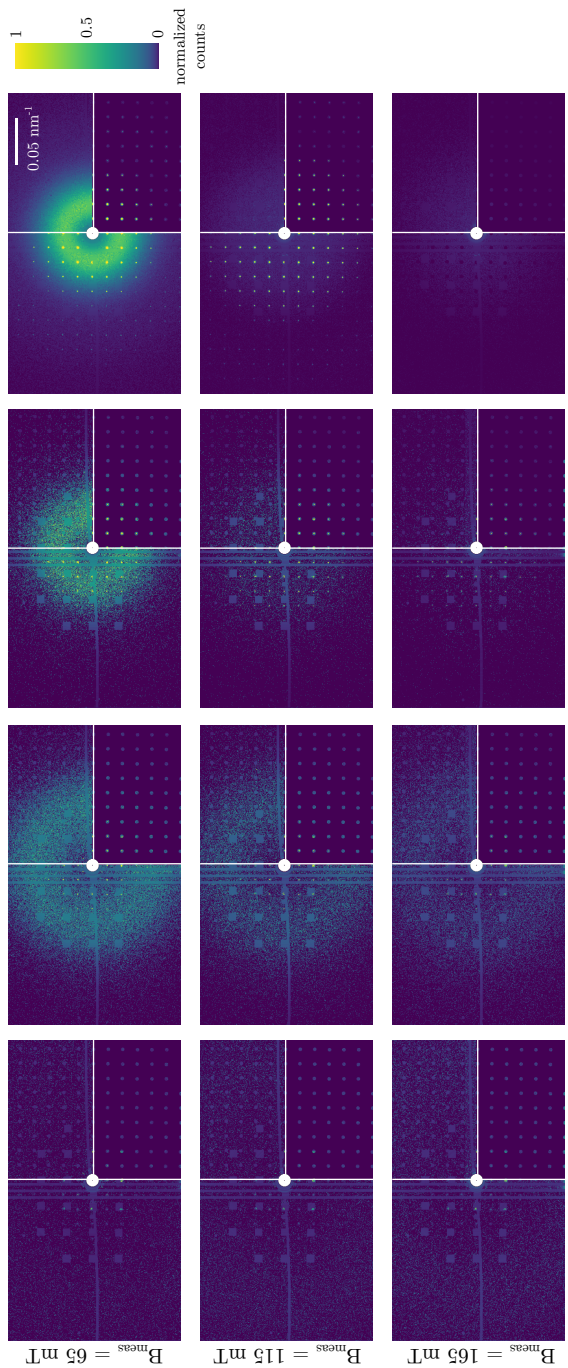

Figure 6.5 | Recorded SAXS scattering patterns for varying time delays after the optical pump pulse and external magnetic fields **a** 65 mT, **b** 115 mT and **c** 165 mT. The left side of each image shows the frame after post-processing, including the removal of direct membrane transmission and interpolation of covered parts of the scattering pattern. The white circle in the center represents the regime that was completely covered by the beamstop, hence without any recorded information. The top right shows the purely isotropic scattering, while the bottom right shows the complementary Bragg scattering signal.

that is the average over all individual frames for the same delay. To remove this noise contribution, thresholding was applied to each frame slightly above the background noise level and all pixels below this threshold were counted as zero. Due to the electronic readout design of the CCD, each quadrant of the image has a different background level. To compensate for this, a spatially varying threshold was applied, depending on the pixel coordinate.

Azimuthal averaging and separation of signal contributions: In some parts of the CCD-frames, a combination of Bragg scattering, isotropic scattering and artifacts collectively define the acquired signal. For proper analysis, these three components needed to be separated. Bragg peak positions were first determined by manually selecting four different Bragg positions, extracting their scattering order and base vectors and using these to calculate the remaining peak positions. All peaks, as well as the areas with parasitic stray light and the beamstop-covered parts of the CCD, were masked. The remaining image contains only isotropic scattering. Exploiting the isotropic nature, the masked areas were filled in with the azimuthal average of the scattering intensity for each particular q to get an approximation of the isolated isotropic scattering part (top-right sections in Fig. 6.5). The Bragg-contribution was obtained by subtracting the purely isotropic scattering from the original SAXS pattern (bottom-right sections in Fig. 6.5). For the few peaks that were coinciding with parasitic transmission, the final state CCD image at 165 mT was subtracted as background, as it only contains the direct transmission without any magnetic small-angle scattering. The left image sections in Fig. 6.5 show the total processed SAXS image as a composite of Bragg and isotropic contributions.

Filtering by optical excitation strength: Comparison of absolute scattering intensities requires adequate normalization of the data. The fluctuations in x-ray intensity could be corrected by normalizing the scattering images against the parasitic direct x-ray transmission through the neighboring membranes. However, fluctuations in the optical excitation also need to be identified, because they can lead to qualitatively different magnetic states, as discussed in sec. 6.3.1. It is particularly important to deposit enough energy to excite the system above the nucleation threshold for skyrmions, as demonstrated in [208]. For each pump-probe event, the optical laser spot was recorded with a separate camera outside the endstation. By comparing the monitored laser positions of pulses that resulted in strong SAXS scattering, we could identify a region on the monitor that corresponds to the sample position. The intensity in this region is therefore proportional to the laser fluence in the actual magnetic sample.

Figure 6.6 shows the final scattering intensity of 100 individual final-state CCD-frames versus the estimated laser intensity. The data is noisy in both axes: While only the SAXS images with the highest transmission signal are shown, in these plots the scattering intensity of each frame (hence, data point) is not normalized. The monitored laser fluence also has significant uncertainty. Nevertheless, we can

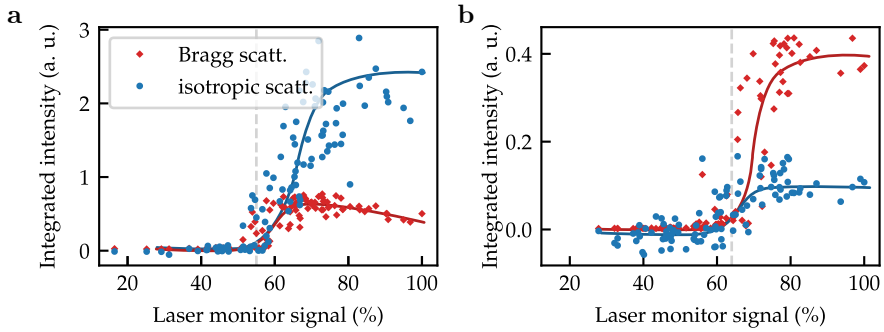

Figure 6.6 | Final state scattering intensity vs. optical excitation strength. The integrated isotropic and Bragg contributions of the 100 brightest individual final state scattering frames are shown. **a** SAXS contributions at low applied field. **b** Scattering contributions at medium applied field. Lines are guides for the eye.

identify a field dependent threshold value, below which the magnetic state essentially stays saturated. Above the threshold, the scattering signal increases rapidly and saturates approximately at 10 % higher intensity. We therefore discarded any frames with a laser monitor signal below this upper saturation threshold, thereby excluding excitations below the nucleation threshold.

6.4.3. Results

Depending on the field regime, the final-state scattering pattern exhibits a prominent structure of bright, Bragg-like peaks. The emergence of these peaks corresponds to magnetic features aligning with the grid of artificial pinning sites in real space. In contrast, isotropic, ring-like scattering stems from features forming outside the irradiated nucleation sites, as is the case for low fields, where the entire film can host stable skyrmions (Fig. 6.5a). While the final state at a low field of 65 mT consists of both an isotropic ring on top of Bragg peaks (hence, mostly disordered skyrmions with a bias towards localizing on the artificial sites), a medium field of 115 mT leads to exclusively pronounced Bragg scattering (Fig. 6.5b). At higher fields, even the Bragg scattering is suppressed in the final state, as the sample returns to homogeneous magnetization. Notably, Bragg features still emerge transiently after the excitation (Fig. 6.5c). The weak, almost uniform, frame-filling scattering at 100 ps delay is the footprint of the sample entering the spatially disordered fluctuation phase, which emerges irrespective of the applied field.

6.4.3.1. Bragg peak analysis

Because the real space magnetic texture and the SAXS image are related by a Fourier transform, we can interpret the Bragg scattering as follows: The *periodicity of Bragg peaks* correlates inversely with the period of the regular skyrmion lattice. Because we imprinted the periodicity ourselves during the sample preparation, this

property is already known to us. The *form of each Bragg-point* is related to the size and shape of the probed area on the sample, hence, the XFEL spot-profile on the membrane (assuming that the optical excitation is homogeneous in the probed area). We find perfectly round, Gaussian spot profiles, which corresponds to a well conditioned Gaussian-like beam shape on the sample. This is likely the result of the deployed up-stream aperture, which conditions the XFEL-beam profile. Finally, the *enveloping function* of the Bragg peak intensity (hence, the global q-dependence of the brightness of each Bragg peak) stems from the form of the individual scatterers, hence the skyrmions on each dot. Specifically, the envelope is impacted by the average shape, size, and positioning of all skyrmions that contribute to the SAXS pattern and is therefore called the structure factor. In the following, we take a closer look at the evolution of the structure factor of the Bragg intensity.

Figure 6.7 shows the average Bragg peak intensity against q for different time delays and for low and medium applied field. The irregular sampling of q reflects the discrete Bragg orders at distances $q_{i,j} = q_0\sqrt{i^2+j^2}, i,j \in \mathbb{Z}$. For both field values, the final states exhibit a local intensity minimum (or even two in the case of low magnetic field). Such a minimum is also visible in some of the time resolved data. There, the minimum is mainly observable for large time delays, which have stronger scattering signal than earlier times. Such radial local minima are characteristic for Airy patterns, which are the result of diffraction on a circular feature. In such a scattering pattern, the position of the first minimum directly depends on the diameter of the feature.

To find the skyrmion diameter, we optimized the fit of the Airy intensity

$$I_{\mathrm{Airy}} = I_0 \left(\frac{2J_1(\gamma)}{\gamma} \right)^2, \tag{6.1}$$

with $\gamma = \frac{\pi D}{\lambda}\sin(\theta)$ and $\theta = 2\arcsin(\frac{q\lambda}{4\pi})$ [99] to each dataset. J_1 is the first Bessel function. Fit parameters were the intensity scale I_0 and the skyrmion diameter D. However, we found that the Airy disk pattern well describes the intensity profile for small q, but fails to properly model the intensity drop at larger q. An example is shown in Fig. 6.7c for the final state. Indeed, the model assumes perfect alignment of all skyrmions on their lattice sites and perfectly sharp domain walls around the skyrmion core, which both do not reflect reality. While multiple ways exist to treat disorder and finite boundaries, we opted to adjust the intensity drop by multiplying a Gaussian envelope function $e^{-\sigma\gamma^2}$, which allows fit and data to agree nicely. The multiplication with a Gaussian essentially models a drop of spatial coherence of the scattering centers, which is caused by deviations from the perfect grid positions as well as a deviation from perfectly circular scattering centers, due to a finite domain wall width.

Fits of the combined model function in Fig. 6.7 are shown for larger delays, with the additional distinction whether the first Airy minimum is clearly observable

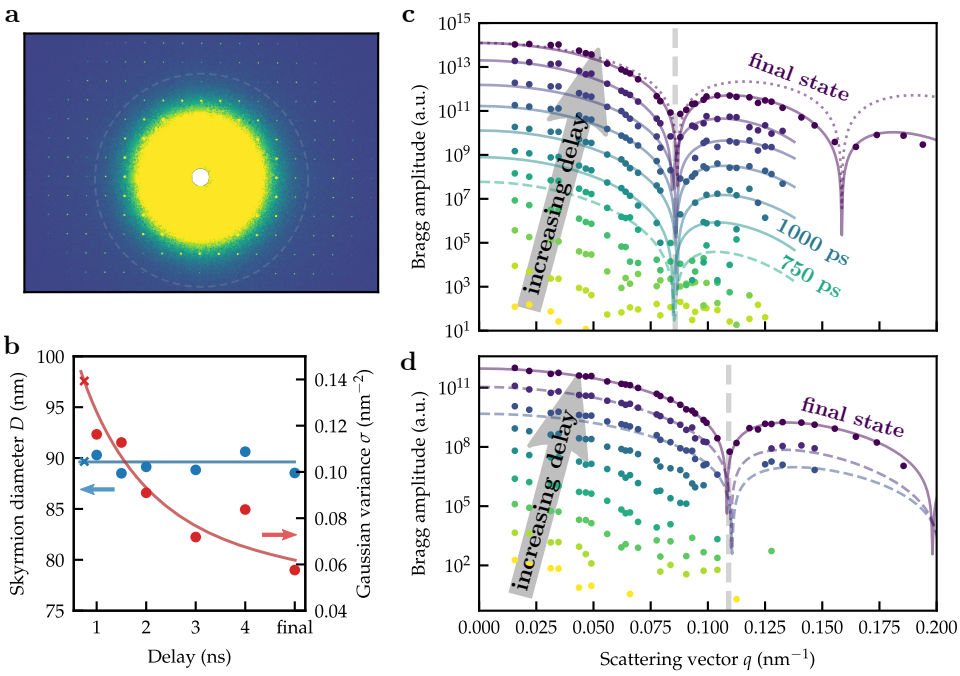

Figure 6.7 | Scattering order resolved Bragg intensity vs. time delay. a Final state SAXS pattern at low field shows a radial minimum in the Bragg peak intensity (marked by the dashed line). **b** Fit results from the q-dependent Bragg intensity distribution. Solid lines act as guide to the eye. The average intensity of each order of Bragg scattering for each recorded delay at **c** low and **d** medium field is plotted logarithmically. An offset increasing with the delay is applied for better readability. Lines show fits of an Airy disk with an additional (fixed) Gaussian envelope. Solid lines show fits where the minimum coincides with the data. Dashed lines show fits for which the intensity minimum position cannot be verified visually due to low SNR. The dotted line shows the expected Bragg amplitude without the Gaussian envelope.

in the data. If the first minimum is not determinable against the noise floor, the fit cannot safely distinguish between a change of the skyrmion diameter D and the width of the Gaussian σ. The final state skyrmions have a diameter of 89 nm and 71 nm at low and medium field, respectively. Hence, they are smaller than the irradiated dot and thus completely reside within the area of altered material properties. The field-dependence of the size is expected and matches with previous studies [208].

While the signal strength at small time delays does not allow for quantitative analysis of the evolution of the skyrmion profile, the fits at larger delays give valuable insight into the long-term dynamics. In the low field regime, we observe that the skyrmion size is constant after 1 ns, as the position of the first Airy minimum does not change with the time delay. Instead, we find a gradual decrease of σ versus time, which correlates to an increase of spatial coherence between skyrmions (Fig. 6.7b). Hence, either the domain walls sharpen or the alignment of

skyrmions to the square grid improves. The fits at smaller delays suggest that the skyrmion diameter is indeed already constant after 750 ps, even though these fits are less reliable. Additionally, the medium field data appears to also show constant skyrmion sizes for large delays, which hints that the constant skyrmion diameter at low fields is not purely a result of close packing of magnetic textures.

6.4.3.2. Analysis of integrated scattering intensity

The Parseval-Plancherel identity [217] describes a relation between the total intensity in real and Fourier space:

$$\int_{-\infty}^{\infty} |f(x)|^2 \, \mathrm{d}x = \int_{-\infty}^{\infty} |\mathcal{F}(f)(q)|^2 \, \mathrm{d}q \tag{6.2}$$

In the Fraunhofer approximation, the SAXS scattering wave front $E(q)$ on the detector is proportional to the Fourier transform of the real-space transmission T in the sample plane. Hence, we can relate the scattering intensity $I(q) = |E(q)|^2$ back to the scattering sources in the sample itself via

$$\int_{-\infty}^{\infty}\int_{-\infty}^{\infty} I(q_x,q_y) \, \mathrm{d}q_x \, \mathrm{d}q_y \propto \int_{-\infty}^{\infty}\int_{-\infty}^{\infty} |T(x,y)|^2 \, \mathrm{d}x \, \mathrm{d}y. \tag{6.3}$$

In section 6.4.2, we completely isolated the isotropic and Bragg-like SAXS scattering intensities I_{iso} and I_{Bragg} in the experimental data. Consequently, as the integral over the sum $I_{\mathrm{iso}} + I_{\mathrm{Bragg}}$ is the sum of individual integrals, eq. 6.3 holds true for each of the two scattering contributions. Specifically, ignoring coherent scattering cross terms, I_{Bragg} is caused exclusively by magnetic scatterers that occupy the artificial nucleation sites and form a perfect square grid. As a result, it serves as a direct measure for the total amount of magnetic contrast localized on these sites. Complementary, I_{iso} is a measure for the strength of magnetic contrast modulation that at most exhibits short range order, hence, the amount of magnetic features that are not localized on the artificial sites. In detail, the interplay of scatterers is somewhat more complex, which will be discussed later.

Although we only recorded a small part of the entire Fourier space, the majority of Fourier intensity is confined to the camera dimensions. Only for small delays significant parts of the isotropic, high-q scattering are cut off. Additionally, the central beamstop covers the low-q regime. Because we only lose a single Bragg peak and the majority of the isotropic scattering intensity is concentrated at higher q, the deviation from Parseval's theorem should be minimal. For each time delay, we integrated the SAXS intensity over the entire available q-space. We performed this analysis for all three magnetic fields, however, we mostly focus on the medium field case, as it most clearly shows the localization dynamics in the dots.

The time evolution of the integrated scattering contributions at medium magnetic field is shown in Fig. 6.8a. Shortly after the optical excitation, the isotropic

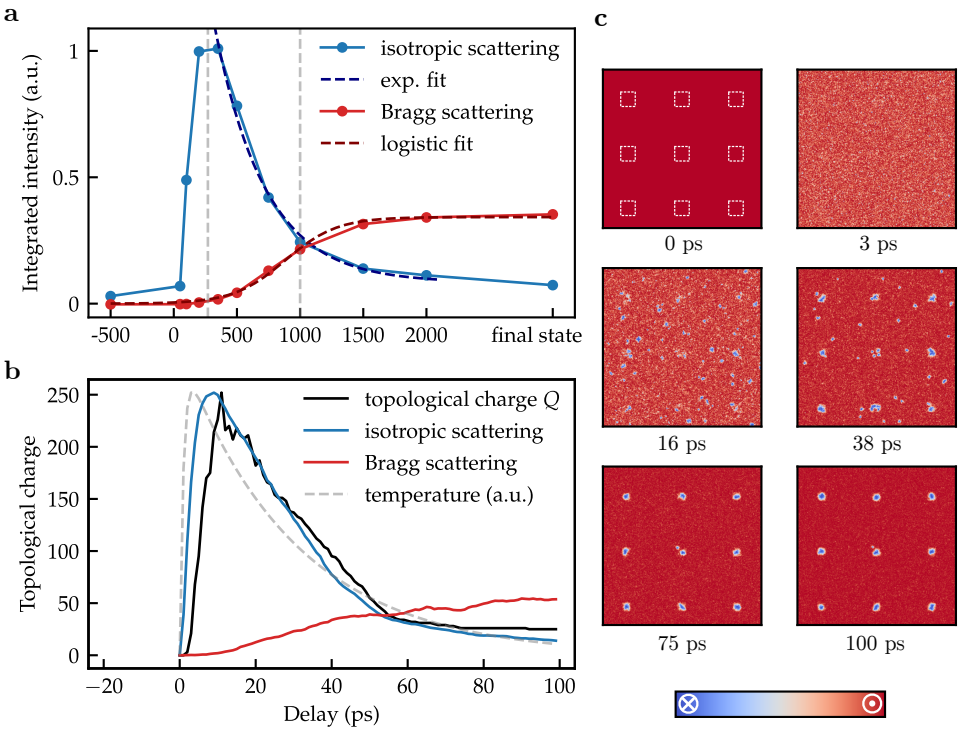

Figure 6.8 | Separated isotropic and Bragg-like q-space contributions in the scattering signal vs. the pump-probe delay. a Experimental data recovered by separating scattering contributions from the CCD-frames as shown in Fig. 6.5. Vertical dashed lines show the peak of the isotropic scattering and the inflection point of the increase in ordered scattering contributions. **b** Data from atomistic spin dynamics simulations that was also separated into Bragg- and isotropic scattering. The deviating timescale compared to the experiment stems from scaling factors in the simulation to speed up the computation. **c** Snap shots of the atomistic simulation state of the real-space magnetization evolution. Colors correspond to the local out-of-plane magnetization component. The areas of reduced anisotropy are indicated by dashed squares.

scattering increases rapidly when the sample enters the fluctuation phase. After a maximum at around 280 ps, the isotropic scattering decays exponentially. At the same time, the Bragg contribution starts to increase, with an inflection point around 750 ps. At 1.5 ns, the Bragg scattering begins to saturate. Therefore, the localization process sets in with a delay only after the sample has exited the fluctuation phase. The same localization delay can be observed for lower and higher field strength (Fig. 6.9) and hence is a field-independent phenomenon.

6.4.4. Atomistic spin dynamics simulation and interpretation

To understand the spatial localization dynamics, atomistic spin dynamics (ADS) simulations were performed by our collaborators in the group of Prof. Johan Mentink, in which a temperature pulse imitates the optical excitation (gray line

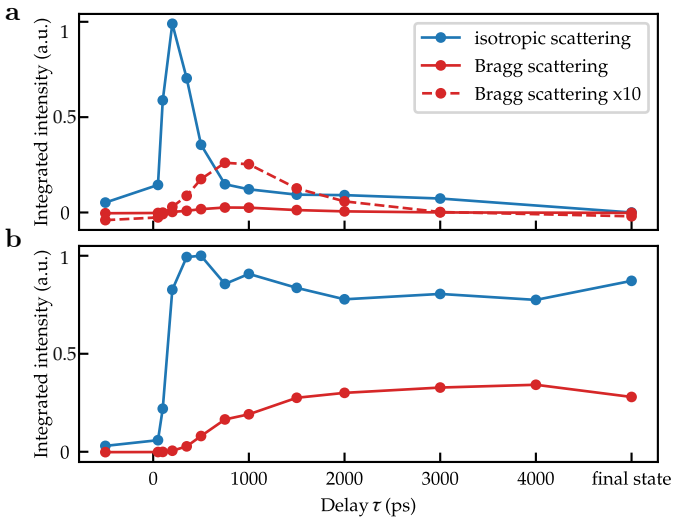

Figure 6.9 | Time evolutions of integrated scattering for high and low field. **a** Integrated Bragg and isotropic Scattering intensity at 165 mT. For better visibility, the Bragg signal is also plotted with increased amplitude. **b** Scattering contributions at 65 mT.

in Fig. 6.8b). The evolution of the initially homogeneous magnetic material is shown in Fig. 6.8c. Irradiated spots were modeled by regular square sections of reduced anisotropy (outlined in Fig. 6.8c for 0 ps). For faster convergence of the simulation, scaled time- and length-scales were used. Fourier-transform of the snapshots returns the SAXS pattern that would correspond to the simulation results. Performing the same separation process of isotropic and Bragg scattering as for the experimental data results in graphs that correspond well with the experiment (Fig. 6.8b), including the initial peak and subsequent exponential decrease of isotropic scattering as well as the delayed gradual increase of the Bragg component. We therefore have the opportunity to match the experimental scattering curves with the simulated real space events.

We can distinguish three phases in the nucleation and localization process. First, the *nucleation-dominated regime* directly after the laser irradiation until 280 ps (experiment time). In this regime, the material reaches its maximum temperature and enters the fluctuation phase, which incites the continuous creation of topological nuclei homogeneously within the magnetic layer (Fig. 6.8c, 3 ps and 16 ps). This leads to a rapid increase in the total topological charge in the system (Fig. 6.8b)). After 300 ps, once the sample cools down sufficiently, the system enters the *decay-dominated regime*. Here, most nuclei outside the spots of altered anisotropy become unstable and quickly collapse, while those within the spots proliferate and grow towards their final skyrmion diameter (Fig. 6.8c, 38 ps). Finally, when each spot is occupied by only a single skyrmion, the sample has reached the *rearrangement regime* (after roughly 1.5 ns experiment time). Here, each skyrmion relaxes towards the center of the respective irradiated area (Fig. 6.8c, 75 ps to

100 ps). Furthermore, the decreasing temperature also reduces the mobility of the bubbles, and they stay closer to their equilibrium position. The result of these dynamics is a comparatively slow, gradual transfer of scattering signal from the isotropic into the Bragg contribution, without the necessity to nucleate or destroy any magnetic features.

6.4.5. Deriving the localization from the static skyrmion stability

In section 2.3.1, we introduced a framework to model the stability of skyrmions in ferromagnetic thin films. The model allows us to determine whether the skyrmion state or homogeneous out-of-plane magnetization is the energetic ground state. Previous studies suggest that for skyrmions to form as the result of thermal (hence also laser induced) excitation, the skyrmion state needs to be this energetic ground state [70]. In the following we investigate if it is sufficient to determine the long-term stability of a skyrmion to predict the outcome of the localization dynamics after laser excitation.

We extracted a set of realistic micromagnetic parameters for the Co/Pt-multilayer, which are listed in table 6.1. See appendix A.4 for a detailed description of how we determined the material parameters by using a variety of characterization tools. Note that the parameters were collected from two samples from different sputtering runs and may have considerable uncertainties but should still reflect a possible set of material properties of a Co/Pt multilayer.

Table 6.1. | Micromagnetic material parameters.

Parameter	value
A_{ex} (pJ/m^3)	12
M_{s} (MA/m)	1.354
D (mJ/m^2)	1.5
$K_{\mathrm{u,\ pristine}}$ (MJ/m^3)	1.35
$K_{\mathrm{u,\ irradiated}}$ (MJ/m^3)	1.25

As the ion bombardment effectively leads to an intermixing at the Co-Pt interfaces, sample characteristics that are governed by these interfaces are much more affected than bulk properties of the Co-layers. The latter include the saturation magnetization and the exchange stiffness. In contrast, the perpendicular magnetic anisotropy is an interfacial effect, which is sensitive to the intermixing [16, 210]. Note that we use a finite DMI value, even though we expect vanishing net-DMI due to symmetric layer stacking. Instead, we utilize the DMI term to take into account flux closure effects in the domain walls. The skyrmion stability model assumes monochiral domain walls and therefore does not take a chirality twist along the sample thickness into account and in consequence overestimates the domain wall energy. As discussed in [54], the flux closure can be expressed as an effective DMI, which we use as a phenomenological correction term here. Because this effective DMI strength thus arises from stray fields and not from indirect interfacial exchange, we do not expect interface intermixing to significantly modify the value. In summary, for our

discussion we therefore assume that the only impact of the ion-irradiation is the local reduction of the perpendicular magnetic anisotropy.

Figure 6.10 shows the analytically calculated skyrmion stability for various applied fields that correspond to the experimental field strengths that were used in the XFEL scattering experiment. Each plot compares the skyrmion energy curve of the irradiated regions with the non-irradiated film. Figure 6.10a corresponds to the high-field regime that does not show any skyrmions in the final state. Accordingly, the energy curve of the non-irradiated film does not show any stable finite skyrmion size, while in the irradiated area a local minimum exists. However, the skyrmion state is not the ground state and the decay energy barrier is extremely shallow. In the low-field regime (Fig. 6.10c), the model predicts a deep global minimum at large skyrmion diameters $> 200\,\mathrm{nm}$ for irradiated as well as non-irradiated areas. In the medium field regime, we find that for the nominal external field value of 115 mT skyrmions should be stable throughout the (non-)irradiated film (Fig. 6.10b, dashed lines), as both curves have a global minimum. If we allow for a slight adjustment of the field upwards to 130 mT, however, the system enters a regime where skyrmions are the ground state in the irradiated areas but at best meta-stable in the non-irradiated film.

Figure 6.10d depicts the skyrmion energy at the minimum position for both irradiation conditions. The three field regimes of skyrmion stability are marked, assuming that laser-induced skyrmion nucleation is only possible if they represent the local magnetic ground state. Due to the shift between both curves, we find the same regions as in the experimental data and as indicated in Fig. 6.2a.

The skyrmion stability model qualitatively fits the observations well. We find, however, that the necessary applied field values in the model do not match perfectly with the experiment, as the former generally tend towards higher values. Besides deficiencies in the measurement of the magnetic field in the experiment, we cannot rule out errors in the determination of the micromagnetic parameters. Parameters were sourced from multiple samples and have strong interdependence, which may lead to increasing deviations from the actual values due to error propagation. Also, the model predicts a skyrmion diameter of 82 nm at medium field inside the irradiated dots. While this value is in the same range as the experimentally observed diameter of 74 nm, it further highlights that the determined material parameters do not perfectly represent the experimental system.

Nevertheless, one likely reason for the difference in the field values is the fact that the model does not take interactions between multiple skyrmions into account. As sketched in Fig. 6.10e, each magnetic bubble or skyrmion creates a stray field in its vicinity. This stray field adds to the applied magnetic field and thereby increases the effective local field compared to the homogeneously magnetized film for any skyrmion that may form close to the existing skyrmion. For the low and medium field regimes, the average distance between skyrmions in our system is

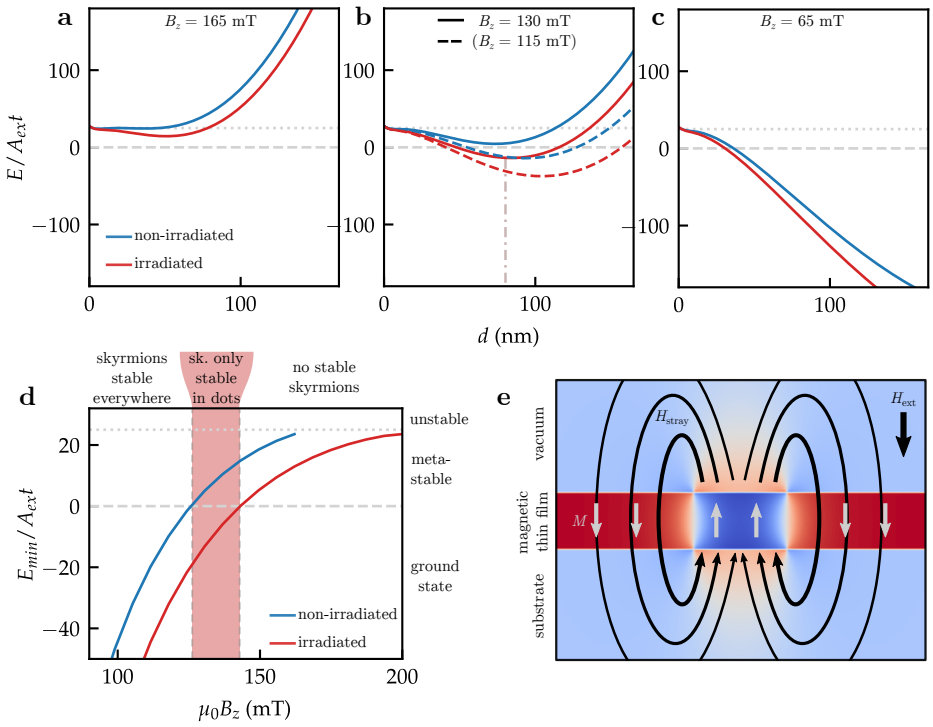

Figure 6.10 | Skyrmion stability considerations of the SAXS sample. Calculated skyrmion energy vs. diameter for the pristine material and the irradiated film at **a** 165 mT **b** 130 mT and **c** 65 mT. In b also the experimental medium field value 115 mT is shown as dashed lines. The dashed and dotted lines mark the transition between skyrmion ground state and metastable state, as well as the energy where the metastable state disappears. **d** Energy of stable, finite sized skyrmions inside and outside the irradiated areas vs. the external field. The red area marks the calculated field regime where skyrmions are the magnetic ground state exclusively inside the irradiated dots. **e** Sketch of additional stray fields induced by already existing skyrmions in the magnetic layer. The existing inversely magnetized skyrmion (blue) creates a stray field H_{stray}, which adds to the applied magnetic field H_{ext} in the rest of the film.

smaller than 400 nm, as determined by the artificial nucleation sites. We can expect stray field interactions to matter at such distances. As the density of skyrmions increases with lower fields, the effect should become even stronger. A similar effect is particularly visible in the low field regime, were neither the predicted skyrmion size nor the equilibrium energy matches the experiment in the slightest, as only isolated individual skyrmions are considered in contrast to the experimentally observed dense skyrmion clusters.

The skyrmion stability model predicts the localization after optical excitation well. While stray field skyrmion-skyrmion interactions need to be considered to optimize the quality of the prediction, even this comparatively simple model of local energy contributions is quantitatively not far from the observed values. Notably, we did not need to consider any dynamic qualities of the system. For example, the anisotropy and saturation magnetization are temperature dependent and thus change transiently during laser heating. Entering the fluctuation state also induces the breakdown of interlayer coupling. Nevertheless, the final-state skyrmion localization pattern appears to depend almost exclusively on the equilibrium stability of the skyrmions.

6.5. Discussion

The dynamics that we find in the simulations allow us to reconcile the contradicting expectation of global optical nucleation with the observed localization. The magnetic system always enters the fluctuation phase – as long as sufficient energy is deposited in the material – and enters the nucleation regime. Independent of the final skyrmion state, the intra- and interlayer exchange reduction leads to the homogeneous emergence of nuclei with topological charge. Notably, topological charge is created exclusively in this regime. However, once exchange is reestablished at lower temperatures, Zeeman and local anisotropy terms again dictate whether a skyrmion is energetically favorable or not. Consequently, skyrmion cores shrink and collapse where they are not energetically stable and proliferate and grow where the local environment is accommodating. Hence, the localization is independent of the initial nucleation, but a purely decay-driven process.

Furthermore, the localization appears to be a local effect. While the simulation shows rearrangement dynamics at larger time delays, these are only small corrective moves towards the center of the irradiated areas once the skyrmions already have grown close to their final diameter. The increase in spatial coherence found in the Bragg-peak analysis at delays past 750 ps, while keeping the Airy-minimum at a constant position, is compatible with the rearrangement of fully formed skyrmions, even though the same observation could also be caused by a contraction of magnetic contrast towards the center of the nucleation sites. This would require that the

overall diameter stays constant, but the effective domain wall starts broad and diffuse and gradually becomes more defined.

The system that is modeled in the atomistic spin dynamics simulations has some drastic simplifications compared to the experiment. The simulation space is two-dimensional and therefore ignores effects along the film's normal direction, including interactions between individual Co-layers. Furthermore, stray field interactions are not simulated, which are the primary energy term that allows for stable skyrmions. Instead, the simulation assumes finite DMI in the material as a substitute stabilizing term for skyrmions. While reports on strong DMI in symmetric multilayers exist [218], our Co/Pt-multilayer cannot exhibit strong DMI, as we observed skyrmions with a Bloch component in Lorentz-TEM. Considering the simplifications, the experimental observations and the modeled dynamics match surprisingly well.

The quasistatic Lorentz-TEM images revealed that a majority of nucleated bubbles on the irradiated dots are Bloch skyrmions. However, a significant number of nucleated features appears to be non-topological. This is in stark contrast to the non-irradiated film, which hosts essentially only skyrmions after the optical excitation [70]. Hence, the local material inhomogeneity created via ion implantation might influence the topology of the locally created magnetic bubbles. Potential causes could be inhomogeneous material modifications along the film normal, due to the low penetration depth of the Ga ions, as well as the more severe structural damage caused by the bombardment, compared to lighter He ions. Thus, it would be of interest to further investigate the impact of the type of ions used on the topology of the localized magnetic textures.

In any case, we can rule out that the shape of the localized bubbles is determined by the irradiated dot. For both low and medium applied fields, the observed skyrmion diameter was below the size of the dot. Crucially, the size is field dependent and shrinks with increasing field, as expected for individual skyrmions in a homogeneous film [64]. In Fig. 6.8a, the decay of the isotropic scattering and the increase of the Bragg contribution can be well described by an exponential decay and a logistic growth model. Notably, the logistic growth describes the recorded data well with a single time constant and it is not necessary to optimize a combination of two independent growth models. Hence, we can surmise that the characteristic timescales of localization are identical for skyrmions and topologically trivial bubbles.

In quasistatic imaging as well as in scattering we observe a significant dependence of the nucleated skyrmion texture on the strength of the optical excitation. We found a minimum threshold intensity to create skyrmions in the multilayer, which depends on the local parameters, including the anisotropy and the applied field. In quasistatic imaging, we also observed an apparent drop of the skyrmion density in the center of the heated area. One explanation for this reduction of the skyrmion density with increasing deposited heat could be that some skyrmions in the regime

of intermediate heat are indeed metastable skyrmions. Hence, they are not the energy ground state but are instead a frozen configuration. Because less energy was deposited in these regions during the excitation, metastable skyrmions had less time to overcome the local decay barrier, compared to the hotter center. Nevertheless, we do not find the same effect in the scattering data. Additionally, the inhomogeneous laser irradiation could also play a role, e. g., in the form of inhomogeneous stray fields arising from a gradient in M_s as a consequence of locally varying demagnetization.

To conclude, we found strong evidence that the localization of optically created magnetic skyrmions sets in after an initial global topological nucleation phase. The effect is driven by the local stability characteristics of the skyrmions, which determine whether they grow or collapse. The locality of the nucleation and localization underlines the potential of laser induced (and generally heat induced) skyrmion nucleation for spintronics applications: Because the localization does not involve ,e. g., magnon currents over large distances or extended movement of topological charge, it should be possible to miniaturize the host sample towards technologically relevant scales while retaining the capability of controlled ultrafast skyrmion creation. Of technological relevance is also the upper boundary of the time window of skyrmion growth, which we determined to be around 1 ns, after which the skyrmion is essentially fully formed, circular and with its final diameter. So far, the nucleation and localization dynamics discussed here have been observed in one particular kind of Co/Pt multilayers. Future investigations should expand the parameter space and also investigate multilayer structures with strong DMI. Furthermore, the skyrmion nucleation and localization dynamics and time scales in thicker multilayers with only stray field interlayer coupling as well as ferrimagnetic multilayer structures would be of interest.

Chapter 7
Summary and outlook

In this thesis we explored how material inhomogeneities and defects influence both the static configurations and dynamic behavior of chiral spin textures. We elucidated the influence of the presence of such inhomogeneities on the static equilibrium structure of chiral domain walls. We have furthermore explored their involvement in the nucleation dynamics of magnetic domains after laser excitation. The interplay between chiral magnetization patterns and material defects during the ultrafast nucleation dynamics could be derived from quasistatic experiments and also directly followed in the time domain. For our investigations we developed and implemented various characterization techniques based on the use of x-rays. These include multiple implementations of direct imaging techniques that enabled us to resolve the magnetization structure within domain walls. An extended time-resolved small angle x-ray scattering method allowed us to directly investigate ultrafast processes with time resolution.

In the first results chapter (chapter 4), we investigated the domain wall structure in ferrimagnetic DyCo thin films by utilizing XMLD-based vector imaging. We observed strong chirality variations within the domain walls, which resulted in extended Bloch- and Néel-type sections along the same domain wall. Our results show that domain wall chirality is locally imprinted by the material and does not depend on the magnetic history of the sample. We explored possible ways in which the chirality variations can emerge naturally from locally modified material properties assuming full PMA. We found evidence that suggests a relation between the chirality variation and lateral composition changes of the host material and developed a theory around such a lateral phase segregation: Compositional variations can modify the local saturation magnetization and the DMI, leading to the stabilization of Bloch and Néel type domain walls within the same sample. Further investigations revealed that these postulated composition variations are predominately located along the domain walls of the as-grown domain state, leading to a faint background contrast visible in MFM.

Indeed, this thesis has only been the foundation for establishing a conclusive explanation for this faint domain contrast. Continued investigation into the topic by Tamer Karaman have recently brought to light the possibility that an in-plane

anisotropy axis at the original domain wall positions exists that is imprinted at growth. Such an in-plane anisotropy would not only explain the local chirality preference but – in combination with the sperimagnetic nature of certain DyCo alloys – also give an explanation for the faint domain contrast.

In chapter 5, we applied vector imaging to analyze the domain wall defect structure of all-optically created domains. We have found evidence that the strength of the material inhomogeneity impacts the existence of defects in magnetic structures. Irrespective of the involved nucleation method, a higher inhomogeneity leads to a higher density of vertical Bloch line defects. We observed that in all-optical switching, after the initial domain nucleation, the domain wall expands. Similar to field cycling, during the domain wall movement, the propagation through the inhomogeneous medium can introduce Bloch lines. In consequence, we found that the Bloch line nucleation at material inhomogeneities dominates the formation of the domain wall defect structure.

Equipped with these findings, we know that to further investigate the intrinsic nucleation and switching process of domains by HI-AOS, the manufacturing of samples with extremely low pinning will be necessary to remove the inhomogeneity-related domain wall defects. In such samples, the creation of Bloch lines during domain wall propagation is expected to be greatly suppressed and in consequence the domain wall defect density would solely depend on the order and speed of the involved phase transition, e. g., following the Kibble-Zurek formalism. This way, domain wall defect analysis could give insight into the fundamental timescale of domain wall formation during all-optical switching.

So far, helicity-independent all-optical switching has almost exclusively been observed in Gd-containing rare-earth transition-metal alloys. To create such low-pinning samples, the inherent tendency of these alloys to segregate spatially needs to be overcome [8, 33]. Alternatively, one can look at other material systems that show HI-AOS, such as ferrimagnetic multilayers and Heusler-compounds.

In chapter 6 we utilized nano-patterning of a magnetic film to investigate the localization dynamics of magnetic skyrmions at artificial pinning sites. We found that in contrast to the spatially homogeneous process of creation of topological nuclei, the localization of final state skyrmions is a purely local process. Skyrmion cores proliferate and grow via magnon coalescence or decay, depending on the local magnetic properties of the host material. Indeed, we found evidence that the final-state skyrmion texture can be predicted exclusively by static skyrmion stability considerations.

With the knowledge that the SAXS technique gives insight into the localization dynamics, the exploration of a larger parameter space is now possible, e. g., varying the ion dose, irradiated dot size and laser parameters. Due to the concentration of the scattering intensity on the Bragg spots, it could be feasible to perform this kind of experiment at a lab-based HHG- or plasma-source that operates in the ultraviolet

and soft x-ray regime. Here, phase space explorations could be performed without the tight time restrictions of an XFEL beamtime.

Similar to previous investigations of ultrafast skyrmion dynamics, we have performed an indirect investigation of the nucleation process: We recorded the time resolved scattering signal which we then matched to a fitting atomistic model. Although this method already gives enough evidence to make conclusions about the nucleation dynamics, directly following the dynamics with time-resolved imaging methods would be beneficial. As discussed in chapters 5 and 6, it is challenging to follow stochastic dynamics in real-space imaging, as stroboscopic methods cannot be used. Nevertheless, it is highly desirable to be able to directly follow the dynamics with imaging. Here, we laid the groundwork for directly accessing the chirality.

With XMLD-based vector spin imaging we developed a technique to efficiently and reliably record the local chirality of domain walls in materials with perpendicular anisotropy. By using x-ray sources with full polarization control and improving the purity of linear polarization at arbitrary polarization angles, the full potential of the imaging method for robust and fast in-situ domain wall imaging experiments can be unlocked. In particular high-resolution coherent imaging will allow for many experiments even in complex sample environments, due to the simplicity of the optical setup. If XMLD-contrast exists at lower energy absorption edges, the application can likely be extended to lab-based HHG-sources [219].

Finally, combining the time resolution of x-ray free electron lasers with coherent imaging and XMLD vector reconstruction promises time resolved imaging of local chirality and topology dynamics. By also utilizing modern classification routines like coherent correlation imaging [130], one could even disentangle stochastic dynamics with a finite number of possible states. Such dynamics of interest could include the formation of topology during skyrmion nucleation or the response of the chirality of magnetic domain walls and skyrmions to electric, thermal and magnetic perturbations. Altogether, these advances pave the way toward capturing ultrafast nanoscopic spin dynamics and chirality evolution in real space and with fs resolution – a key milestone toward future spintronic and magnetic memory technologies.

Chapter A
Appendix

A.1. Temperature dependent SQUID measurements

To determine the internal material distribution of the DyCo film, temperature dependent magnetization hysteresis curves were recorded via SQUID-magnetometry. To improve the signal quality, magnetization data was recorded in "VSM"-mode, for which the sample oscillates quickly inside the SQUID pickup coils (similarly to conventional vibrating sample magnetometry) and the SQUID signal is acquired by lock-in amplification. This method increases the signal quality and reduces outliers in the data. However, temperature-related sample drift can introduce a deviation (generally a reduction) of the measured magnetic moment. Temperature changes were generally carried out at zero applied field and before each measurement an automatic recentering routine was performed.
The omnipresent transition at zero-field in the loops (comp. Fig. A.1) stems likely from magnetic material that was deposited on the exposed edges of the substrate during sputtering. As this superfluous material does not grow on the flat side of the substrate, it does not share the same properties as the sample film, including its anisotropy, and behaves like a magnetically soft impurity.
Near the compensation temperature the coercive field of the major loop increases. Additionally, a second transition at high magnetic field appears, which has been connected to the introduction of a domain wall that separates the film in two domains along the normal direction [83]. These two domains are above and below their local compensation temperatures, respectively, due to a gradient in the material composition. Therefore, at low fields, exchange leads to parallel alignment of the elemental sublattices and thus antiparallel alignment of the total magnetization of the domains. The increased Zeeman term at high fields overcomes the exchange along the film normal and flips the net-magnetization in the field direction. This behavior is typical for a synthetic antiferromagnet. Another clear indicator for a complex sample of at least two antiferromagnetically coupled subsystems is the observation of negative hysteresis close to the compensation temperature. Note that the loops alone do not specify the spatial shape of the composition variation.

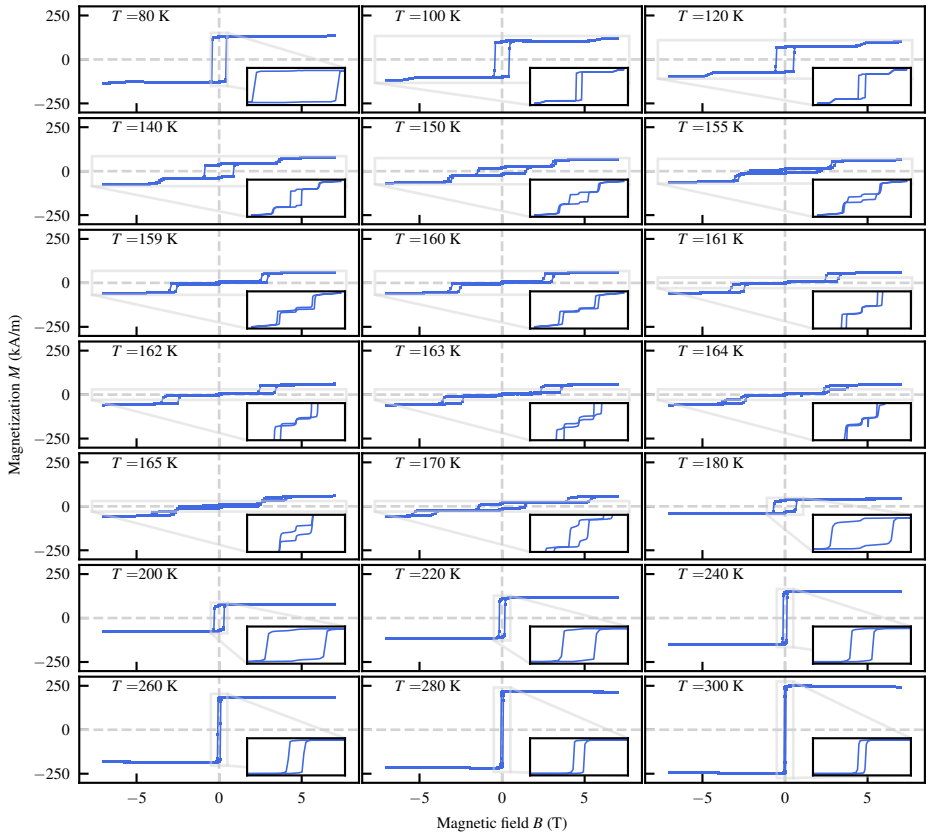

Figure A.1 | Out-of-plane magnetization curves of DyCo vs. temperature recorded via SQUID. While the main figures all show the same range, the insets show a individually chosen zoomed in region to highlight certain features and transitions.

A.2. Determination of the magnetic anisotropy of DyCo

To determine the magnetic anisotropy of the DyCo thin film, we utilized a technique based on determining the saturation energy as described in [220] and [221]. The saturation energy E_s describes the difference in free energy between the saturated (F_s) and demagnetized (F_0) state and is defined as the path integral from full demagnetization to saturation

$$E_\mathrm{s} = F_\mathrm{s} - F_0 = \int_0^{M_\mathrm{s}} H \,\mathrm{d}M. \tag{A.1}$$

By assuming that F_0 is identical for in-plane and out-of-plane, i. e. by starting the integral from the same or an equivalent demagnetized domain state, and shifting the arbitrary free energy scale such that $F_{\mathrm{s,IP}} = 0$, we get

$$F_{\mathrm{s,OOP}} = E_{\mathrm{s,OOP}} - E_{\mathrm{s,IP}} \tag{A.2}$$

as the free energy of the out-of-plane saturated state. This energy is comprised of energy contributions from the uniaxial anisotropy and magnetostatic energy from the stray field.

$$F_{\mathrm{s,OOP}} = \frac{\mu_0 M_\mathrm{s}^2}{2} - K_\mathrm{u} \tag{A.3}$$

By inserting equation (A.2) into equation (A.3) and rearranging, we obtain an expression for the anisotropy constant:

$$K_\mathrm{u} = \frac{\mu_0 M_\mathrm{s}^2}{2} - E_{\mathrm{s,OOP}} + E_{\mathrm{s,IP}} \tag{A.4}$$

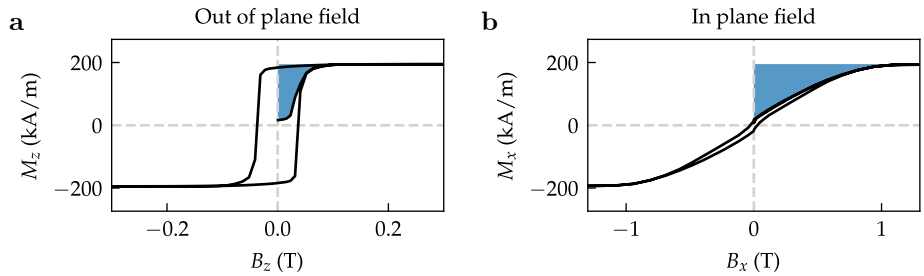

Figure A.2 | SQUID measurements of DyCo to determine K_u. Magnetization and hysteresis curves are shown for **a** out-of-plane **b** in plane sample alignment within the SQUID geometry.

We determined the saturation energies by recording magnetization curves in SQUID. We demagnetized the sample via field-cycling with diminishing amplitude and subsequently recorded the magnetization curve once in the out-of-plane and once in the in-plane configuration (compare Fig. A.2). The highlighted areas represent the integrals according to eq. (A.1). The saturation magnetization was obtained from the same curves by normalizing the measured magnetic moment with respect to the volume of the sample.

A.3. Tilted sample XMCD vector imaging

†The experimental setup of the MAXYMUS microscope allowed for a sample tilt of $+30°$ along the y-axis, but not $-30°$ along the same axis. XMCD absorption contrast is proportional to the projection $\mathbf{M} \cdot \mathbf{k}$ of the local magnetization $\mathbf{M}$ on the propagation direction of the x-ray beam $\mathbf{k}$. Subtracting a set of $\pm 30°$ images isolates the in-plane component because the projections of out-of-plane magnetic moments cancel out while in-plane components perpendicular to the rotation axis add constructively (compare Fig. A.3b and Fig. A.3c). Figure A.3d illustrates that a sample rotation of 180° around the out-of-plane axis results in the same projected image contrast as $-30°$, albeit rotated.

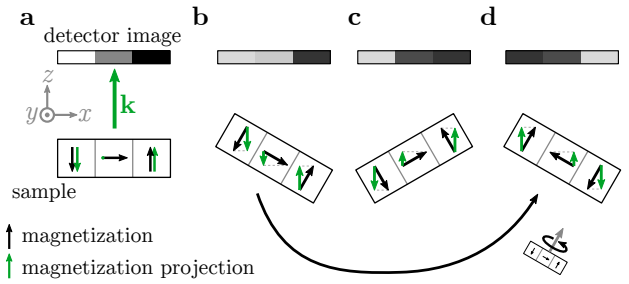

Figure A.3 | Sample manipulation steps performed during vector imaging. Shown is the cross-sectional view through a simplified Néel domain wall. Arrows show the local magnetization and the projection on **E**, which is proportional to the XMCD contrast recorded by the detector. **a** Normal incidence, **b** +30° tilt, **c** −30° tilt. **d** Additional rotation of the +30° tilted sample by 180° around the out-of-plane axis.

†We estimate the spatial resolution of the vector images from the contrast and the apparent width of domain walls in the in-plane images. Specifically, we know that some spins in a domain wall with vertical Bloch lines must point along the x-ray beam in the tilted geometry. Hence, we expect these sections to show $\sin(30°)/\cos(30°) \approx 57.7\,\%$ of the out-of-plane contrast within the domains (where the factor is due to the 30° tilt angle). Multiple measurements of the in-plane domain wall contrast, as indicated in Fig. A.4a, return values between 70 % and 85 % of this expected contrast amplitude. The in-plane domain wall magnetization profile follows $M_{\mathrm{IP}}(x) = M_{\mathrm{s}}/\cosh(x/\Delta)$, with the domain wall width parameter Δ, from which the domain wall width can be estimated as $\pi\Delta$ (compare Fig. A.4b). The finite imaging resolution r results in an apparent smoothing of the domain wall profile, which is modeled by convolving with a Gaussian with FWHM r.

†As shown in figure A.4b, the convolution of the physical domain wall profile with the Gaussian not only widens the observed profile, but also reduces the amplitude, solely depending on the width of the Gaussian r compared to the domain wall width Δ. By adjusting the amplitude of the broadened domain wall profile to the measured values, we find ratios between $\frac{r}{\Delta} = 1.6$ and 2.7. Notably, even the larger value for r is below the full domain wall width $\pi\Delta$, hence the resolution is small enough to reasonably resolve the domain walls and Bloch lines of similar size. Fitting a line-scan of the in-plane contrast with the convolved domain wall profile with the known ratio $\frac{r}{\Delta}$ results in a numeric estimate of $\Delta = (19 \pm 2)\,\mathrm{nm}$, which corresponds to a domain wall width of $\pi\Delta = (60 \pm 6)\,\mathrm{nm}$ and a resolution of $r = (44 \pm 3)\,\mathrm{nm}$. Note that the estimated resolution is weaker than the potentially attainable 25 nm of the MAXYMUS instrument and also spatially variable, due to the tilted sample geometry and resulting depth-of-field effects.

†Simulations of the XMCD transmission contrast show that the in-plane contrast can also be affected by membrane wrinkling, which takes the form of an additional, inherent tilt of the magnetic film. The rotation of the two-dimensional magnetic

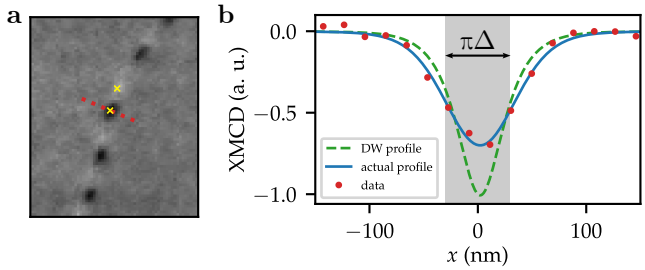

Figure A.4 | Estimation of imaging resolution and domain wall width. a ±30° XMCD difference image. Yellow crosses indicate sampling positions for the contrast measurement. **b** Domain wall cross section. Red dots show line scan indicated in (a). Dashed line shows the isolated domain wall profile, while the continuous line shows the domain wall profile convoluted with the imaging resolution.

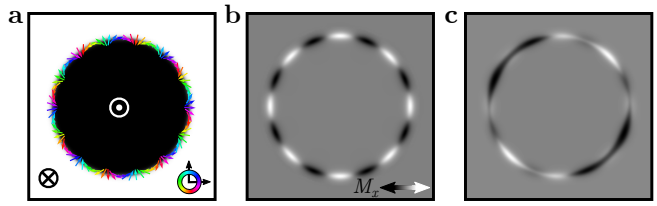

Figure A.5 | Impact of membrane wrinkling on the recovered in-plane information. a Magnetic bubble with high density of vertical Bloch lines. **b** Simulation of the XMCD-based ±30° difference image, assuming a perfectly flat sample. **c** Difference image for the same state with an additional permanent sample tilt of 2° around x and 7° around y.

pattern of a defect-rich bubble domain (Fig. A.5a) was calculated by applying a set of consecutive rotations on the position and direction of each magnetic moment within the simulated magnetic layer. The XMCD-contrast was approximated as the local magnetization component collinear with the beam propagation direction. Figure A.5b shows the difference of one simulated transmission image for a 30° rotation around the y-axis and one image for a 180° rotation around z followed by a 30° rotation around y (as described in Fig. A.3d). Figure A.5c shows the difference image for the same transformations where an additional sample tilt of 2° around x and 7° around y was introduced ahead of the other rotations to imitate a wrinkling membrane. In both cases, the second image was rotated by 180° to restore the original orientation before subtraction. While the domain wall in Fig. A.5b exhibits a clear black-white transition for each vertical Bloch line, the contrast is less clear in Fig. A.5c. Due to the additional tilt, the contrast modulations are suppressed, some sections are biased, while the domain wall contrast is reduced in others.

†We note that we exclude scanning artifacts to be the origin of the black-and-white modulations in the in-plane difference images. Repeated scans of the same domain wall with a stable point-by-point scanning mode resulted in the same recovered in-plane component, hence stochastic and systematic distortions did not

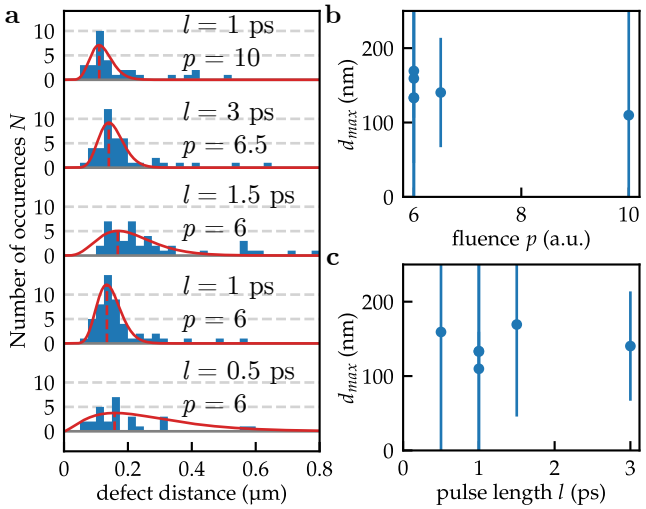

Figure A.6 | Dependence of the vertical Bloch line statistics on the laser parameters. a Histograms of the defect-distances and best fitting Γ-functions for each nucleated bubble in the Ta/GdFe/Pt sample with the annotated pulse length l and pulse energy p (in a. u.). **b** Fitted peak positions against the laser fluence. **c** Fitted peak positions against the pulse length.

impact the reconstruction. All small domains were imaged in this point-by-point scanning mode. Large domains were imaged in the faster line-at-once scanning mode, which has introduced distortion artifacts in the past. However, we found no signs of distortions in the present experiment, neither in direct comparison with point-by-point test scans nor in the process of combining images from different angles.

†Multiple bubble domains resulting from various sets of laser excitation parameters were imaged in the Ta/GdFe/Pt sample. Figure A.6 shows the distance statistics of domain wall defects for each parameter set. Within the fit uncertainties, no parameter dependence is apparent, neither for the pulse energy (Fig. A.6b), nor for the pulse duration (Fig. A.6c).

A.4. Determination of micromagnetic properties of Co/Pt-multilayers

The validity of our discussion of the local skyrmion stability in the Co/Pt-multilayer samples requires the model to be as close as possible to the experimental system. To make the calculations as realistic as possible, we performed a set of measurements to acquire the micromagnetic parameters of the material. Besides the spatial structure of the film, these include the exchange stiffness A_{ex}, the saturation magnetization M_{s}, the DMI strength D and the magnetic perpendicular anisotropy constant K_{u}. It is difficult to extract all parameters from the same sample, especially

in case of local ion irradiation (examples from literature require, e. g., the creation of microscopic Hall crosses [210]). We therefore obtained the parameters by measuring properties on two multilayer samples (the actual membrane sample and a nominally identical reference multilayer on a silicon substrate that was fabricated in the same sputtering system around the same time), in combination with a set of crucial assumptions:

1. The saturation magnetization, the exchange stiffness and the DMI do not vary between the two samples. The first two are mainly bulk properties of the Co-layers, which should not drastically change between sample depositions.

2. The exchange stiffness is expected to be in the range of 10-25 pJ/m. Previous reports measured values in this range for similar samples [222].

3. Flux closure domain walls are expected in the material, which we model by allowing a finite DMI strength.

4. Skyrmions and domain walls show clear Bloch contrast in Lorentz-TEM (compare section 6.3.2). Therefore, the DMI cannot be so strong that it stabilizes exclusively Néel type domain walls.

5. The main effect of ion irradiation is a reduction of the local perpendicular anisotropy. We ignore any further parameter modifications by ion bombardment.

We measured the saturation magnetization of the reference sample via SQUID magnetometry in an MPMS3-setup. The out-of-plane hysteresis loop was recorded and the linear diamagnetic background subtracted. The resulting magnetization curve is shown in figure A.7a. The determined saturation magnetization $M_\mathrm{s} = 1.354\,\mathrm{MA/m}$ as well as the saturation field $H_\mathrm{sat} = 130\,\mathrm{mT}$ are indicated.
We used Stoner-Wohlfahrt analysis to determine the magnetic anisotropy $K_\mathrm{u,pristine}$ of the same reference film. We recorded hysteresis curves for various different angles between the sample and the applied field direction. For each angle, we measured the out-of-plane magnetization component with a zero-offset corrected Hall-transport setup, as depicted in Fig. A.7b. For the evaluation, we only considered the high field regime ($\mu_0 H > 1\,\mathrm{T}$). In this field range, no domains exist and the magnetization rotates coherently. In consequence, the Stoner-Wohlfahrt model description solely requires the material parameters to determine the effective anisotropy of the film. Fitting the dataset according to the procedure described in [223], we acquired a ratio of $K_\mathrm{eff}/M_\mathrm{s} = 1.6\,\mathrm{J/Am^2}$. With the known M_s, this result corresponds to $K_\mathrm{u} = 1.57\,\mathrm{MJ/m^3}$.
With the saturation magnetization and anisotropy known, we estimated the strength of exchange and DMI interaction from the saturation field. We used the analytical skyrmion model [64] to find a set of parameters which predict a skyrmion collaps for

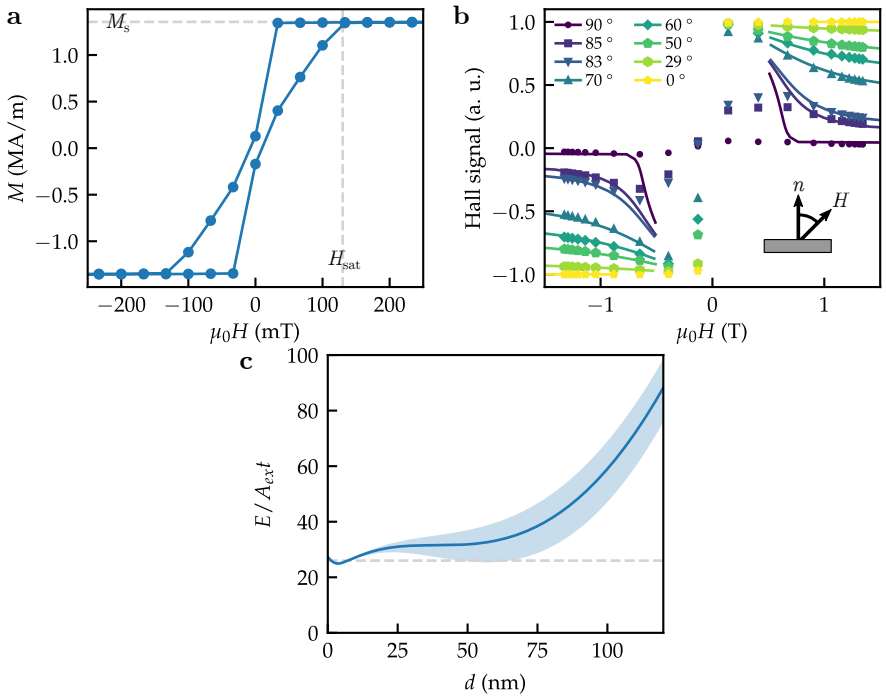

Figure A.7 | Auxiliary measurements of micromagnetic properties. a Measurement of the Co magnetization in a reference sample measured with SQUID. **b** Magnetization vs. field of the same reference sample for various applied field angles. Solid lines show the fit result of a single-domain Stoner Wohlfahrt model. **c** Skyrmion energy curve at the saturation field H_{sat}, at which the local minimum vanishes. The shaded area depicts the range caused by a 10 % variance in the material parameters, exemplary shown for the exchange stiffness.

the measured saturation field. When increasing the field, a domain state will only be stable until H_{sat} is reached. In the skyrmion model, this condition is reflected in the disappearance of the local energy minimum at finite skyrmion diameter (comp. Fig. 2.5a). Figure A.7c depicts this condition for the reference film. We find $D = 1.5\,\mathrm{mJ/m^2}$ and $A_{\mathrm{ex}} = 12\,\mathrm{pJ/m^3}$, respectively. Note that the values are not entirely unambiguous because a larger D also results in a larger A_{ex}.

Finally, in a similar manner, the anisotropies of the irradiated and non-irradiated sample where determined. While the reference film has a saturation field of $H_{\mathrm{sat}} = 130\,\mathrm{mT}$, the non-irradiated multilayer exhibits saturation at $H_{\mathrm{sat}} = 175\,\mathrm{mT}$ and the irradiated patches an even higher $H_{\mathrm{sat}} = 200\,\mathrm{mT}$ (compare MOKE curves in Fig. 6.2a). By decreasing the perpendicular anisotropy, we can also shift the saturation field to higher values in our model: The domain wall surrounding the skyrmion is less energy intensive and thus a stronger external field is required to destabilize the skyrmion. We find anisotropy values of $K_{\mathrm{u}} = 1.35\,\mathrm{MJ/m^3}$ for the non-irradiated film and $K_{\mathrm{u}} = 1.25\,\mathrm{MJ/m^3}$ for the ion-irradiated areas.

A.5. XFEL probe beam intensity calibration

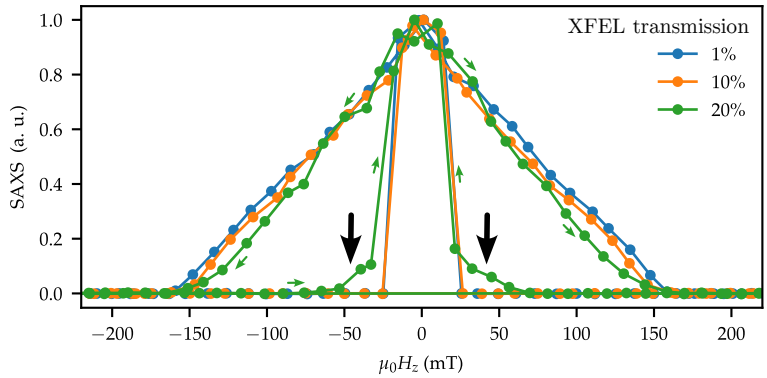

Figure A.8 | SAXS hysteresis curves for various XFEL intensities. Plots show the frame-integrated total scattering intensity vs. the applied magnetic field for the specified photon transmission through a gas cell upstream of the sample. Small green arrows indicate the direction of the field sweep.

Similar to infrared and optical irradiation, high intensity x-ray pulses can modify the magnetic state of the Co/Pt multilayer. For the pump-probe experiment it was paramount to only modify the magnetic texture with the optical pump pulse and not perturb the sample with the x-ray probe. Specifically, high-intensity X-FEL pulses can initiate skyrmion nucleation by themselves and excessive x-ray fluences may anneal the magnetic host material irreversibly. To determine the highest possible x-ray fluence, we recorded static hysteresis curves. Figure A.8 shows the integrated SAXS scattering intensity during the field sweep for various x-ray fluences in the sample. The intensity is directly related to the number of domains in the probed area, hence, no scattering is equivalent to a saturated sample. While 1 % and 10 % x-ray intensity show identical nucleation fields, 20 % intensity exhibits a higher nucleation field. At this X-FEL intensity, the deposited energy per x-ray pulse is high enough to nucleate magnetic patterns by itself.

List of Figures

List of Tables

Publications and Contributions

1. List of publications

1. **D. Metternich**, M. Schneider, G. Mercurio., T. Hegstad, M. Möller, R. Battistelli, C. Klose, S. Wittrock, M. Patram, K. Puzhekadavil Joy, V. Deinhart, D. Engel, T. Sidiropoulos, R. E. Carley, L. Mercadier, A. Scherz, M. Teichmann, S. Zayko, B. Sorokin, K. Bagschik, C. Ropers, J. Mentink, B. Pfau & F. Büttner: Mechanism and timescale of skyrmion localization after ultrafast topological switching. (in preparation)

2. L.-M. Kern, K. Litzius, V. Deinhart, M. Schneider, C. Klose, K. Gerlinger, R. Battistelli, **D. Metternich**, D. Engel, C. M. Günther, M.-J. Huang, K. Höflich, F. Büttner, S. Eisebitt & B. Pfau: From Ordered States to Emergent Complexity in Spin-Orbit Torque-Driven Skyrmion Dynamics. (under review)

3. A. Wittmann, O. Gomonay, B. H. Lee, A. E. Kossak, A. Churikova, R. Battistelli, **D. Metternich**, E. A. Tremsina, M. Weigand, F. Maccherozzi, A. Morales, G. P. Hellmann, F. Büttner, C. Degen, S. Wintz, J. Sinova, N. O. Birge & G. S. D. Beach: Magnetic roses: novel topological spin textures stabilized by non-chiral long-range interactions. (under review)

4. **D. Metternich**, K. Litzius, S. Wintz, K. Gerlinger, S. Petz, D. Engel, T. Sidiropoulos, R. Battistelli, F. Steinbach, M. Weigand, S. Wittrock, C. von Korff Schmising & F. Büttner: Defects in magnetic domain walls after single-shot all-optical switching. *Structural Dynamics* **12**, 024504 (2025).

5. R. Battistelli, **D. Metternich**, M. Schneider, L.-M. Kern, K. Litzius, J. Fuchs, C. Klose, K. Gerlinger, K. Bagschik, C. M. Günther, D. Engel, C. Ropers, S. Eisebitt, B. Pfau, F. Büttner & S. Zayko: Coherent x-ray magnetic imaging with 5 nm resolution. *Optica* **11**, 234–237 (2024).

6. L.-M. Kern, B. Pfau, V. Deinhart, M. Schneider, C. Klose, K. Gerlinger, S. Wittrock, D. Engel, I. Will, C. M. Günther, R. Liefferink, J. H. Mentink, S. Wintz, M. Weigand, M.-J. Huang, R. Battistelli, **D. Metternich**, F. Büttner, K. Höflich & S. Eisebitt: Deterministic Generation and Guided Motion of Magnetic Skyrmions by Focused He^+-Ion Irradiation. *Nano Letters* **22**, 4028–4035 (2022).

7. K. Gerlinger, R. Liefferink, M. Schneider, L.-M. Kern, C. Klose, **D. Metternich**, D. Engel, F. Capotondi, D. De Angelis, M. Pancaldi, E. Pedersoli, F. Büttner, S. Eisebitt, J. H. Mentink, & B. Pfau: Robust scenario for the generation of non-equilibrium topological fluctuation states. Preprint at https://doi.org/10.48550/arXiv.2212.03143 (2022).

8. K. Gerlinger, B. Pfau, F. Büttner, M. Schneider, L.-M. Kern, J. Fuchs, D. Engel, C. M. Günther, M. Huang, I. Lemesh, L. Caretta, A. Churikova, P. Hessing, C. Klose, C. Strüber, C. von K. Schmising, S. Huang, A. Wittmann, K. Litzius, **D. Metternich**, R. Battistelli, K. Bagschik, A. Sadovnikov, G. S. D. Beach & S. Eisebitt: Application concepts for ultrafast laser-induced skyrmion creation and annihilation. *Applied Physics Letters* **118**, 192403 (2021).

2. List of conference talks

1. The mechanism and timescale of skyrmion localization during all-optical topological switching, DPG spring meeting, Berlin 2024.

2. Direct observation of bulk-DMI-stabilized Néel-type domain walls in ferrimagnetic rare-earth transition-metal alloys, Joint European Magnetic Symposia, Warsaw 2022.

Bibliography

[1] A. Thiaville *et al.*: Dynamics of Dzyaloshinskii Domain Walls in Ultrathin Magnetic Films. *Europhysics Letters* **100**, 57002 (2012). DOI: 10.1209/0295-5075/100/57002.

[2] F. Ajejas *et al.*: Tuning Domain Wall Velocity with Dzyaloshinskii-Moriya Interaction. *Applied Physics Letters* **111**, 202402 (2017). DOI: 10.1063/1.5005798.

[3] A. Hubert and R. Schäfer: *Magnetic Domains: The Analysis of Magnetic Microstructures*. Springer-Verlag, Berlin, Heidelberg, New York, 1998. ISBN: 978-3-540-64108-7.

[4] V. L. Sobolev: Internal Structure of a Domain Wall in Ultrathin Magnetic Film. *Journal of Magnetism and Magnetic Materials* **177–181**, 195–196 (1998). DOI: 10.1016/S0304-8853(97)00331-4.

[5] A. Fert *et al.*: From Early Theories of Dzyaloshinskii–Moriya Interactions in Metallic Systems to Today's Novel Roads. *Journal of the Physical Society of Japan* **92**, 081001 (2023). DOI: 10.7566/JPSJ.92.081001.

[6] A. P. Malozemoff and J. C. Slonczewski: *Magnetic Domain Walls in Bubble Materials*. Academic Press, New York, 1979. ISBN: 978-0-12-002951-8.

[7] Y. Yoshimura *et al.*: Soliton-like Magnetic Domain Wall Motion Induced by the Interfacial Dzyaloshinskii–Moriya Interaction. *Nature Physics* **12**, 157–161 (2016). DOI: 10.1038/nphys3535.

[8] C. E. Graves *et al.*: Nanoscale Spin Reversal by Non-Local Angular Momentum Transfer Following Ultrafast Laser Excitation in Ferrimagnetic GdFeCo. *Nature Materials* **12**, 293–298 (2013). DOI: 10.1038/nmat3597.

[9] D.-H. Kim *et al.*: Bulk Dzyaloshinskii–Moriya Interaction in Amorphous Ferrimagnetic Alloys. *Nature Materials* **18**, 685–690 (2019). DOI: 10.1038/s41563-019-0380-x.

[10] D. J. Craik and G. Myers: Bloch Lines and Hysteresis in Uniaxial Magnetic Crystals. *The Philosophical Magazine: A Journal of Theoretical Experimental and Applied Physics* **31**, 489–502 (1975). DOI: 10.1080/14786437508226532.

[11] P. Chaudhari, C. H. Bajorek, and M. H. Kryder: Amorphous Gd-Co Alloys for Magnetic Bubble Applications. In: *Magnetic Bubbles*. Ed. by H. Jouve. Academic Press, London, Orlando, 1986. Chap. 2, 31–90. ISBN: 978-0-12-391220-6.

[12] M. S. Pierce *et al.*: Influence of Structural Disorder on Magnetic Domain Formation in Perpendicular Anisotropy Thin Films. *Physical Review B* **87**, 184428 (2013). DOI: 10.1103/PhysRevB.87.184428.

[13] R. Wolfe *et al.*: Ion Implanted Patterns for Magnetic Bubble Propagation. In: *AIP Conference Proceedings*. AIP, Denver, Colorado, 1973, 339–343. DOI: 10.1063/1.2946913.

[14] M. V. Sapozhnikov *et al.*: Artificial Dense Lattice of Magnetic Bubbles. *Applied Physics Letters* **109**, 042406 (2016). DOI: 10.1063/1.4958300.

[15] M. V. Sapozhnikov *et al.*: Direct Observation of Topological Hall Effect in Co/Pt Nanostructured Films. *Physical Review B* **103**, 054429 (2021). DOI: 10.1103/PhysRevB.103.054429.

[16] L.-M. Kern *et al.*: Deterministic Generation and Guided Motion of Magnetic Skyrmions by Focused He^+-Ion Irradiation. *Nano Letters* **22**, 4028–4035 (2022). DOI: 10.1021/acs.nanolett.2c00670.

[17] R. B. J. Warnar and P. J. Calomeris: *Computer Science & Technology : Foreign and Domestic Accomplishments in Magnetic Bubble Device Technology*. U.S. Dept. of Commerce, National Bureau of Standards, Washington, 1977.

[18] D. J. Breed and U. Enz: Garnet Films for High Bubble Velocities and High Bubble Mobilities. In: *Magnetic Bubbles*. Ed. by H. Jouve. Academic Press, London, Orlando, 1986. Chap. 3, 91–137. ISBN: 978-0-12-391220-6.

[19] R. Wolfe and J. C. North: Suppression of Hard Bubbles in Magnetic Garnet Films by Ion Implantation. *Bell System Technical Journal* **51**, 1436–1440 (1972). DOI: 10.1002/j.1538-7305.1972.tb02661.x.

[20] A. Hubert: Statics and Dynamics of Domain Walls in Bubble Materials. *Journal of Applied Physics* **46**, 2276–2287 (1975). DOI: 10.1063/1.321822.

[21] R. A. Kosinski, J. J. Zebrowski, and A. Sukiennicki: On the Effect of Material Inhomogeneities on the Generation of Vertical Bloch Lines. *Journal of Physics D: Applied Physics* **22**, 451 (1989). DOI: 10.1088/0022-3727/22/3/012.

[22] B. Seng *et al.*: Direct Imaging of Chiral Domain Walls and Néel-Type Skyrmionium in Ferrimagnetic Alloys. *Advanced Functional Materials* **31**, 2102307 (2021). DOI: 10.1002/adfm.202102307.

[23] G. Schütz *et al.*: Absorption of Circularly Polarized X Rays in Iron. *Physical Review Letters* **58**, 737–740 (1987). DOI: 10.1103/PhysRevLett.58.737.

[24] J. Stöhr: *The Nature of X-Rays and Their Interactions with Matter*. Vol. 288. Springer International Publishing, Cham, 2023. ISBN: 978-3-031-20744-0. DOI: 10.1007/978-3-031-20744-0.

[25] S. Zayko *et al.*: Coherent Diffractive Imaging beyond the Projection Approximation: Waveguiding at Extreme Ultraviolet Wavelengths. *Optics Express* **23**, 19911–19921 (2015). DOI: 10.1364/OE.23.019911.

[26] R. Battistelli *et al.*: Coherent X-Ray Magnetic Imaging with 5 nm Resolution. *Optica* **11**, 234–237 (2024). DOI: 10.1364/OPTICA.505999.

[27] E. Beaurepaire: Ultrafast Spin Dynamics in Ferromagnetic Nickel. *Physical Review Letters* **76** (1996). DOI: 10.1103/PhysRevLett.76.4250.

[28] C. D. Stanciu *et al.*: All-Optical Magnetic Recording with Circularly Polarized Light. *Physical Review Letters* **99**, 047601 (2007). DOI: 10.1103/PhysRevLett.99.047601.

[29] T. Ostler *et al.*: Ultrafast Heating as a Sufficient Stimulus for Magnetization Reversal in a Ferrimagnet. *Nature Communications* **3**, 666 (2012). DOI: 10.1038/ncomms1666.

[30] D. Metternich *et al.*: Defects in Magnetic Domain Walls after Single-Shot All-Optical Switching. *Structural Dynamics* **12**, 024504 (2025). DOI: 10.1063/4.0000287.

[31] J. M. D. Coey: *Magnetism and Magnetic Materials*. Cambridge University Press, Cambridge, 2009. ISBN: 978-0-511-67743-4.

[32] R. Gross and A. Marx: *Festkörperphysik*. Oldenbourg, München, 2012. ISBN: 978-3-486-71294-0.

[33] E. Kirk *et al.*: Anisotropy-Induced Spin Reorientation in Chemically Modulated Amorphous Ferrimagnetic Films. *Physical Review Materials* **4**, 074403 (2020). DOI: 10.1103/PhysRevMaterials.4.074403.

[34] A. Chanda *et al.*: Tunable Competing Magnetic Anisotropies and Spin Reconfigurations in Ferrimagnetic $Fe_{100-x}Gd_x$ Alloy Films. *Physical Review B* **104**, 094404 (2021). DOI: 10.1103/PhysRevB.104.094404.

[35] D. Mergel, H. Heitmann, and P. Hansen: Pseudocrystalline Model of the Magnetic Anisotropy in Amorphous Rare-Earth–Transition-Metal Thin Films. *Physical Review B* **47**, 882–891 (1993). DOI: 10.1103/PhysRevB.47.882.

[36] R. J. Gambino and J. J. Cuomo: Selective Resputtering-induced Anisotropy in Amorphous Films. *Journal of Vacuum Science and Technology* **15**, 296–301 (1978). DOI: 10.1116/1.569574.

[37] V. G. Harris and T. Pokhil: Selective-Resputtering-Induced Perpendicular Magnetic Anisotropy in Amorphous TbFe Films. *Physical Review Letters* **87**, 067207 (2001). DOI: 10.1103/PhysRevLett.87.067207.

[38] D. Lordan *et al.*: Origin of Perpendicular Magnetic Anisotropy in Amorphous Thin Films. *Scientific Reports* **11**, 3734 (2021). DOI: 10.1038/s41598-020-78950-7.

[39] W. Y. Zhang *et al.*: Origin of Perpendicular Magnetic Anisotropy and Evolution of Magnetic Domain Structure of Amorphous Pr–TM–B (TM=Fe, Co) Films. *Journal of Magnetism and Magnetic Materials* **322**, 900–908 (2010). DOI: 10.1016/j.jmmm.2009.11.022.

[40] Y. Takeno, K. Kaneko, and K. Goto: Magnetic Properties of Amorphous $(Tb_{1-x}Gd_x)_{30}Fe_{70}$ Thin Films. *Japanese Journal of Applied Physics* **30**, 1701 (1991). DOI: 10.1143/JJAP.30.1701.

[41] M. Ding and S. J. Poon: Tunable Perpendicular Magnetic Anisotropy in GdFeCo Amorphous Films. *Journal of Magnetism and Magnetic Materials* **339**, 51–55 (2013). DOI: 10.1016/j.jmmm.2013.03.007.

[42] V. G. Harris *et al.*: Structural Origins of Magnetic Anisotropy in Sputtered Amorphous Tb-Fe Films. *Physical Review Letters* **69**, 1939–1942 (1992). DOI: 10.1103/PhysRevLett.69.1939.

[43] E. C. Stoner and E. P. Wohlfarth: A Mechanism of Magnetic Hysteresis in Heterogeneous Alloys. *Philosophical Transactions of the Royal Society of London. Series A, Mathematical and Physical Sciences* **240**, 599–642 (1948). DOI: 10.1098/rsta.1948.0007.

[44] M. Zelent *et al.*: Spin Dynamics in Patterned Magnetic Multilayers with Perpendicular Magnetic Anisotropy. In: *Solid State Physics*. Ed. by R. Macedo. Vol. 73. Academic Press, 2022, 1–51. DOI: 10.1016/bs.ssp.2022.08.002.

[45] I. Dzyaloshinsky: A Thermodynamic Theory of "Weak" Ferromagnetism of Antiferromagnetics. *Journal of Physics and Chemistry of Solids* **4**, 241–255 (1958). DOI: 10.1016/0022-3697(58)90076-3.

[46] T. Moriya: Anisotropic Superexchange Interaction and Weak Ferromagnetism. *Physical Review* **120**, 91–98 (1960). DOI: 10.1103/PhysRev.120.91.

[47] R. E. Camley and K. L. Livesey: Consequences of the Dzyaloshinskii-Moriya Interaction. *Surface Science Reports* **78**, 100605 (2023). DOI: 10.1016/j.surfrep.2023.100605.

[48] T. Gilbert: A Phenomenological Theory of Damping in Ferromagnetic Materials. *IEEE Transactions on Magnetics* **40**, 3443–3449 (2004). DOI: 10.1109/TMAG.2004.836740.

[49] I. Cimrák: A Survey on the Numerics and Computations for the Landau-Lifshitz Equation of Micromagnetism. *Archives of Computational Methods in Engineering* **15**, 1–37 (2007). DOI: 10.1007/BF03024947.

[50] M. Heide, G. Bihlmayer, and S. Blügel: Dzyaloshinskii-Moriya Interaction Accounting for the Orientation of Magnetic Domains in Ultrathin Films: Fe/W(110). *Physical Review B* **78**, 140403 (2008). DOI: 10.1103/PhysRevB.78.140403.

[51] I. Lemesh, F. Büttner, and G. S. D. Beach: Accurate Model of the Stripe Domain Phase of Perpendicularly Magnetized Multilayers. *Physical Review B* **95**, 174423 (2017). DOI: 10.1103/PhysRevB.95.174423.

[52] E. Schlömann: Domain Walls in Bubble Films. I. General Theory of Static Properties. *Journal of Applied Physics* **44**, 1837–1849 (1973). DOI: 10.1063/1.1662460.

[53] E. Schlömann: Domain Walls in Bubble Films. II. Static Properties of Thick Films. *Journal of Applied Physics* **44**, 1850–1854 (1973). DOI: 10.1063/1.1662461.

[54] I. Lemesh and G. S. D. Beach: Twisted Domain Walls and Skyrmions in Perpendicularly Magnetized Multilayers. *Physical Review B* **98**, 104402 (2018). DOI: 10.1103/PhysRevB.98.104402.

[55] J. C. Slonczewski: Theory of Domain-wall Motion in Magnetic Films and Platelets. *Journal of Applied Physics* **44**, 1759–1770 (1973). DOI: 10.1063/1.1662444.

[56] A. Manchon: *Spintronics Lectures*. URL: https://physiquemanchon.wixsite.com/research/spintronics-lectures (visited on 09/21/2024).

[57] P. Chauve, T. Giamarchi, and P. Le Doussal: Creep and Depinning in Disordered Media. *Physical Review B* **62**, 6241–6267 (2000). DOI: 10.1103/PhysRevB.62.6241.

[58] P. J. Metaxas *et al.*: Creep and Flow Regimes of Magnetic Domain-Wall Motion in Ultrathin Pt/Co/Pt Films with Perpendicular Anisotropy. *Physical Review Letters* **99**, 217208 (2007). DOI: 10.1103/PhysRevLett.99.217208.

[59] F. B. Hagedorn: Dynamic Conversion during Magnetic Bubble Domain Wall Motion. *Journal of Applied Physics* **45**, 3129–3140 (1974). DOI: 10.1063/1.1663737.

[60] J. Masell and K. Everschor-Sitte: Current-Induced Dynamics of Chiral Magnetic Structures: Creation, Motion, and Applications. In: *Chirality, Magnetism and Magnetoelectricity: Separate Phenomena and Joint Effects in Metamaterial Structures*. Ed. by E. Kamenetskii. Springer International Publishing, Cham, 2021, 147–181. ISBN: 978-3-030-62844-4. DOI: 10.1007/978-3-030-62844-4_7.

[61] S. Li, X. Wang, and T. Rasing: Magnetic Skyrmions: Basic Properties and Potential Applications. *Interdisciplinary Materials* **2**, 260–289 (2023). DOI: 10.1002/idm2.12072.

[62] W. Jiang *et al.*: Direct Observation of the Skyrmion Hall Effect. *Nature Physics* **13**, 162–169 (2017). DOI: 10.1038/nphys3883.

[63] K. Litzius *et al.*: Skyrmion Hall Effect Revealed by Direct Time-Resolved X-ray Microscopy. *Nature Physics* **13**, 170–175 (2017). DOI: 10.1038/nphys 4000.

[64] F. Büttner, I. Lemesh, and G. S. D. Beach: Theory of Isolated Magnetic Skyrmions: From Fundamentals to Room Temperature Applications. *Scientific Reports* **8**, 4464 (2018). DOI: 10.1038/s41598-018-22242-8.

[65] B. Dai *et al.*: Electric Field Manipulation of Spin Chirality and Skyrmion Dynamic. *Science Advances* **9**, eade6836 (2023). DOI: 10.1126/sciadv.ade68 36.

[66] J. A. Cape and G. W. Lehman: Magnetic Domain Structures in Thin Uniaxial Plates with Perpendicular Easy Axis. *Journal of Applied Physics* **42**, 5732–5756 (1971). DOI: 10.1063/1.1660007.

[67] G. A. Jones: Magnetic Bubble Domains. *Science Progress* **63**, 219–240 (1976).

[68] A. O. Leonov *et al.*: The Properties of Isolated Chiral Skyrmions in Thin Magnetic Films. *New Journal of Physics* **18**, 065003 (2016). DOI: 10.1088/1 367-2630/18/6/065003.

[69] A. N. Bogdanov and D. A. Yablonskii: Thermodynamically Stable "Vortices" in Magnetically Ordered Crystals. The Mixed State of Magnets. *Sov. Phys. JETP* **68**, 101 (1989).

[70] F. Büttner *et al.*: Observation of Fluctuation-Mediated Picosecond Nucleation of a Topological Phase. *Nature Materials* **20**, 30–37 (2021). DOI: 10.1038/s41563-020-00807-1.

[71] J. Wild *et al.*: Entropy-Limited Topological Protection of Skyrmions. *Science Advances* **3**, e1701704 (2017). DOI: 10.1126/sciadv.1701704.

[72] W. Jiang *et al.*: Blowing Magnetic Skyrmion Bubbles. *Science* **349**, 283–286 (2015). DOI: 10.1126/science.aaa1442.

[73] S. Finizio *et al.*: Deterministic Field-Free Skyrmion Nucleation at a Nanoengineered Injector Device. *Nano Letters* **19**, 7246–7255 (2019). DOI: 10.1021/acs.nanolett.9b02840.

[74] I. Lemesh *et al.*: Current-Induced Skyrmion Generation through Morphological Thermal Transitions in Chiral Ferromagnetic Heterostructures. *Advanced Materials* **30**, 1805461 (2018). DOI: 10.1002/adma.201805461.

[75] G. Berruto *et al.*: Laser-Induced Skyrmion Writing and Erasing in an Ultrafast Cryo-Lorentz Transmission Electron Microscope. *Physical Review Letters* **120**, 117201 (2018). DOI: 10.1103/PhysRevLett.120.117201.

[76] Z. Wang *et al.*: Thermal Generation, Manipulation and Thermoelectric Detection of Skyrmions. *Nature Electronics* **3**, 672–679 (2020). DOI: 10.1038 /s41928-020-00489-2.

[77] N. Bergeard *et al.*: Irreversible Transformation of Ferromagnetic Ordered Stripe Domains in Single-Shot Infrared-Pump/Resonant-x-Ray-Scattering-Probe Experiments. *Physical Review B* **91**, 054416 (2015). DOI: 10.1103/PhysRevB.91.054416.

[78] K. Gerlinger *et al.*: *Robust Scenario for the Generation of Non-Equilibrium Topological Fluctuation States*. 2022. DOI: 10.48550/arXiv.2212.03143. arXiv: 2212.03143.

[79] W. Zhang *et al.*: Optical Creation of Skyrmions by Spin Reorientation Transition in Ferrimagnetic CoHo Alloys. *ACS Applied Materials & Interfaces* **15**, 5608–5619 (2023). DOI: 10.1021/acsami.2c19411.

[80] S. P. Parappurath and J. R. Mohanty: Non-Equillibrium Ultrafast Optical Excitation as a Stimulus for Ultra-Small Field-Free Magnetic Skyrmions in Ferrimagnetic GdFeCo. *Journal of Applied Physics* **136**, 123908 (2024). DOI: 10.1063/5.0223860.

[81] E. Iacocca *et al.*: Spin-Current-Mediated Rapid Magnon Localisation and Coalescence after Ultrafast Optical Pumping of Ferrimagnetic Alloys. *Nature Communications* **10**, 1756 (2019). DOI: 10.1038/s41467-019-09577-0.

[82] T. A. Ostler *et al.*: Crystallographically Amorphous Ferrimagnetic Alloys: Comparing a Localized Atomistic Spin Model with Experiments. *Physical Review B* **84**, 024407 (2011). DOI: 10.1103/PhysRevB.84.024407.

[83] C. Luo *et al.*: X-Ray Magnetic Linear Dichroism as a Probe for Non-Collinear Magnetic State in Ferrimagnetic Single Layer Exchange Bias Systems. *Scientific Reports* **9**, 18169 (2019). DOI: 10.1038/s41598-019-54356-y.

[84] F. Jakobs: Unifying Femtosecond and Picosecond Single-Pulse Magnetic Switching in Gd-Fe-Co. *Physical Review B* **103**, 104422 (2021). DOI: 10.1103/PhysRevB.103.104422.

[85] C. D. Stanciu *et al.*: Subpicosecond Magnetization Reversal across Ferrimagnetic Compensation Points. *Physical Review Letters* **99**, 217204 (2007). DOI: 10.1103/PhysRevLett.99.217204.

[86] W. Zhang *et al.*: Criteria to Observe Single-Shot All-Optical Switching in Gd-based Ferrimagnetic Alloys. *Physical Review B* **109**, 094412 (2024). DOI: 10.1103/PhysRevB.109.094412.

[87] J. Wei *et al.*: All-Optical Helicity-Independent Switching State Diagram in Gd - Fe - Co Alloys. *Physical Review Applied* **15**, 054065 (2021). DOI: 10.1103/PhysRevApplied.15.054065.

[88] Y. Yang *et al.*: Ultrafast Magnetization Reversal by Picosecond Electrical Pulses. *Science Advances* **3**, e1603117 (2017). DOI: 10.1126/sciadv.1603117.

[89] M. L. M. Lalieu *et al.*: Deterministic All-Optical Switching of Synthetic Ferrimagnets Using Single Femtosecond Laser Pulses. *Physical Review B* **96**, 220411 (2017). DOI: 10.1103/PhysRevB.96.220411.

[90] L. Avilés-Félix *et al.*: Integration of Tb/Co Multilayers within Optically Switchable Perpendicular Magnetic Tunnel Junctions. *AIP Advances* **9**, 125328 (2019). DOI: 10.1063/1.5129821.

[91] M. Beens *et al.*: Comparing All-Optical Switching in Synthetic-Ferrimagnetic Multilayers and Alloys. *Physical Review B* **100**, 220409 (2019). DOI: 10.1103/PhysRevB.100.220409.

[92] C. Banerjee *et al.*: Single Pulse All-Optical Toggle Switching of Magnetization without Gadolinium in the Ferrimagnet Mn_2Ru_xGa. *Nature Communications* **11**, 4444 (2020). DOI: 10.1038/s41467-020-18340-9.

[93] I. Radu *et al.*: Transient Ferromagnetic-like State Mediating Ultrafast Reversal of Antiferromagnetically Coupled Spins. *Nature* **472**, 205–208 (2011). DOI: 10.1038/nature09901.

[94] J. H. Mentink *et al.*: Ultrafast Spin Dynamics in Multisublattice Magnets. *Physical Review Letters* **108**, 057202 (2012). DOI: 10.1103/PhysRevLett.108.057202.

[95] C. Davies *et al.*: Pathways for Single-Shot All-Optical Switching of Magnetization in Ferrimagnets. *Physical Review Applied* **13**, 024064 (2020). DOI: 10.1103/PhysRevApplied.13.024064.

[96] F. Jakobs and U. Atxitia: Universal Criteria for Single Femtosecond Pulse Ultrafast Magnetization Switching in Ferrimagnets. *Physical Review Letters* **129**, 037203 (2022). DOI: 10.1103/PhysRevLett.129.037203.

[97] G. Sala *et al.*: Asynchronous Current-Induced Switching of Rare-Earth and Transition-Metal Sublattices in Ferrimagnetic Alloys. *Nature Materials* **21**, 640–646 (2022). DOI: 10.1038/s41563-022-01248-8.

[98] E. Abbe: Beiträge Zur Theorie Des Mikroskops Und Der Mikroskopischen Wahrnehmung. *Archiv für Mikroskopische Anatomie* **9**, 413–468 (1873).

[99] F. L. Pedrotti, L. M. Pedrotti, and L. S. Pedrotti: *Introduction to Optics*. 3rd ed. Pearson/Prentice Hall, Upper Saddle River, N.J, 2007. ISBN: 978-0-13-149933-1.

[100] N. Gray: Knowing the Limit. *Nature Cell Biology* **11**, S8 (2009). DOI: 10.1038/ncb1940.

[101] R. T. Borlinghaus: Super-Resolution - On a Heuristic Point of View About the Resolution of a Light Microscope. *Analytik News* (2015).

[102] J. Stöhr and H. C. Siegmann: *Magnetism: From Fundamentals to Nanoscale Dynamics*. Springer-Verlag, Berlin, Heidelberg, New York, 2006. ISBN: 978-3-540-30282-7.

[103] D. T. Attwood: *Soft X-Rays and Extreme Ultraviolet Radiation: Principles and Applications*. Cambridge University Press, Cambridge, New York, 2000. ISBN: 978-0-521-65214-8.

[104] B. Pfau and S. Eisebitt: X-Ray Resonant Scattering and Holography with Application to Magnetization Dynamics. In: *Structural Dynamics with X-ray and Electron Scattering*. Ed. by K. Amini, A. Rouzée, and M. J. J. Vrakking. Royal Society of Chemistry, 2023, 254–300. ISBN: 978-1-83767-156-4. DOI: 10.1039/BK9781837671564-00254.

[105] J. Kirz and C. Jacobsen: The History and Future of X-ray Microscopy. *Journal of Physics: Conference Series* **186**, 012001 (2009). DOI: 10.1088/1742-6596/186/1/012001.

[106] L. Baumgarten: X-ray Absorption Spectroscopies. In: *Scattering Methods for Condensed Matter Research: Towards Novel Applications at Future Sources*. Ed. by M. Angst. Forschungszentrum Jülich, Jülich, 2012. Chap. F4, 91–137. ISBN: 978-3-89336-759-7.

[107] A. C. Thompson *et al.*: *X-Ray Data Booklet*. 2nd edition. University of California, Berkeley, 2001.

[108] B. Watts: Calculation of the Kramers-Kronig Transform of X-ray Spectra by a Piecewise Laurent Polynomial Method. *Optics Express* **22**, 23628–23639 (2014). DOI: 10.1364/OE.22.023628.

[109] J. Neethirajan *et al.*: Soft X-Ray Phase Nanomicroscopy of Micrometer-Thick Magnets. *Physical Review X* **14**, 031028 (2024). DOI: 10.1103/PhysRevX.14.031028.

[110] C. Donnelly *et al.*: High-Resolution Hard X-ray Magnetic Imaging with Dichroic Ptychography. *Physical Review B* **94**, 064421 (2016). DOI: 10.1103/PhysRevB.94.064421.

[111] J. L. Erskine and E. A. Stern: Calculation of the M_{23} Magneto-Optical Absorption Spectrum of Ferromagnetic Nickel. *Physical Review B* **12**, 5016–5024 (1975). DOI: 10.1103/PhysRevB.12.5016.

[112] B. T. Thole, G. van der Laan, and G. A. Sawatzky: Strong Magnetic Dichroism Predicted in the $M_{4,5}$ X-Ray Absorption Spectra of Magnetic Rare-Earth Materials. *Physical Review Letters* **55**, 2086–2088 (1985). DOI: 10.1103/PhysRevLett.55.2086.

[113] G. van der Laan *et al.*: Experimental Proof of Magnetic X-Ray Dichroism. *Physical Review B* **34**, 6529–6531 (1986). DOI: 10.1103/PhysRevB.34.6529.

[114] M. M. Schwickert *et al.*: X-Ray Magnetic Linear Dichroism in Absorption at the L Edge of Metallic Co, Fe, Cr, and V. *Physical Review B* **58**, R4289(R) (1998). DOI: 10.1103/PhysRevB.58.R4289.

[115] J. Stöhr *et al.*: Principles of X-Ray Magnetic Dichroism Spectromicroscopy. *Surface Review and Letters* **05**, 1297–1308 (1998). DOI: 10.1142/S0218625X98001638.

[116] J. B. Goedkoop *et al.*: Calculations of Magnetic X-Ray Dichroism in the 3d Absorption Spectra of Rare-Earth Compounds. *Physical Review B* **37**, 2086–2093 (1988). DOI: 10.1103/PhysRevB.37.2086.

[117] J. Díaz and C. Blanco-Roldán: Magnetic Moment Orientation and In-Depth Distribution of Dysprosium near the Surface of $DyCo_{4.6}$ Thin Films from x-Ray Circularly Polarized Absorption. *Physical Review B* **104**, 054439 (2021). DOI: 10.1103/PhysRevB.104.054439.

[118] J. Kirz and D. Sayre: Soft X-Ray Microscopy of Biological Specimens. In: *Synchrotron Radiation Research*. Ed. by H. Winick and S. Doniach. Springer, Boston, MA, 1980, 277–322. ISBN: 978-1-4615-7998-4. DOI: 10.1007/978-1-4615-7998-4_8.

[119] M. Weigand: Realization of a New Magnetic Scanning X-ray Microscope and Investigation of Landau Structures under Pulsed Field Excitation. PhD thesis. Universität Stuttgart, Stuttgart, 2014. ISBN: 978-3-95404-991-2.

[120] M. Weigand *et al.*: TimeMaxyne: A Shot-Noise Limited, Time-Resolved Pump-and-Probe Acquisition System Capable of 50 GHz Frequencies for Synchrotron-Based X-ray Microscopy. *Crystals* **12**, 1029 (2022). DOI: 10.3390/cryst12081029.

[121] T. Li, A. J. Senesi, and B. Lee: Small Angle X-ray Scattering for Nanoparticle Research. *Chemical Reviews* **116**, 11128–11180 (2016). DOI: 10.1021/acs.chemrev.5b00690.

[122] O. Hellwig *et al.*: X-Ray Studies of Aligned Magnetic Stripe Domains in Perpendicular Multilayers. *Physica B: Condensed Matter* **336**, 136–144 (2003). DOI: 10.1016/S0921-4526(03)00282-5.

[123] K. S. Gerlinger: Nanometer scale observation of magnetization textures induced by ultrashort laser pulses. PhD thesis. Technische Universität Berlin, Berlin, 2023.

[124] J. T. Winthrop and C. R. Worthington: X-Ray Microscopy by Successive Fourier Transformation. *Physics Letters* **15**, 124–126 (1965). DOI: 10.1016/0031-9163(65)91304-1.

[125] B. Pfau and S. Eisebitt: X-Ray Holography. In: *Synchrotron Light Sources and Free-Electron Lasers: Accelerator Physics, Instrumentation and Science Applications*. Ed. by E. J. Jaeschke *et al.* Springer International Publishing, Cham, 2016, 1093–1133. ISBN: 978-3-319-14394-1. DOI: 10.1007/978-3-319-14394-1_28.

[126] S. Eisebitt *et al.*: Lensless Imaging of Magnetic Nanostructures by X-ray Spectro-Holography. *Nature* **432**, 885–888 (2004). DOI: 10.1038/nature03139.

[127] J. Geilhufe *et al.*: Achieving Diffraction-Limited Resolution in Soft-X-ray Fourier-transform Holography. *Ultramicroscopy* **214**, 113005 (2020). DOI: 10.1016/j.ultramic.2020.113005.

[128] S. Flewett *et al.*: Holographically Aided Iterative Phase Retrieval. *Optics Express* **20**, 29210–29216 (2012). DOI: 10.1364/OE.20.029210.

[129] F. Büttner: Topological Mass of Magnetic Skyrmions Probed by Ultrafast Dynamic Imaging. PhD thesis. Johannes Gutenberg-Universität, Mainz, 2013.

[130] C. Klose *et al.*: Coherent Correlation Imaging for Resolving Fluctuating States of Matter. *Nature* **614**, 256–261 (2023). DOI: 10.1038/s41586-022-05537-9.

[131] J. McCord: Progress in Magnetic Domain Observation by Advanced Magneto-Optical Microscopy. *Journal of Physics D: Applied Physics* **48**, 333001 (2015). DOI: 10.1088/0022-3727/48/33/333001.

[132] M. R. Parker: The Kerr Magneto-Optic Effect (1876–1976). *Physica B+C* **86–88**, 1171–1176 (1977). DOI: 10.1016/0378-4363(77)90836-1.

[133] T. Haider: A Review of Magneto-Optic Effects and Its Application. *International Journal of Electromagnetics and Applications* **7**, 17–24 (2017).

[134] F. Steinbach *et al.*: Wide-Field Magneto-Optical Microscope to Access Quantitative Magnetization Dynamics with Femtosecond Temporal and Sub-Micrometer Spatial Resolution. *Journal of Applied Physics* **130**, 083905 (2021). DOI: 10.1063/5.0060091.

[135] E. M. Pugh, N. Rostoker, and A. Schindler: On the Hall Effect in Ferromagnetics. *Physical Review* **80**, 688–692 (1950). DOI: 10.1103/PhysRev.80.688.

[136] D. Culcer: The Anomalous Hall Effect. In: *Encyclopedia of Condensed Matter Physics*. Vol. 1. Elsevier Ltd, 2024, 587–601. ISBN: 978-0-12-803581-8. DOI: 10.1016/B978-0-323-90800-9.00006-8.

[137] R. C. O'Handley: *Modern Magnetic Materials: Principles and Applications*. John Wiley & Sons Ltd, New York, 1999. ISBN: 978-0-471-15566-9.

[138] F. D. M. Haldane: Berry Curvature on the Fermi Surface: Anomalous Hall Effect as a Topological Fermi-Liquid Property. *Physical Review Letters* **93**, 206602 (2004). DOI: 10.1103/PhysRevLett.93.206602.

[139] R. Abrudan *et al.*: Element-Specific Magnetization Damping in Ferrimagnetic $DyCo_5$ Alloys Revealed by Ultrafast X-ray Measurements. *Physica Status Solidi RRL* **15**, 2100047 (2021). DOI: 10.1002/pssr.202100047.

[140] R. L. Fagaly: Superconducting Quantum Interference Device Instruments and Applications. *Review of Scientific Instruments* **77**, 101101 (2006). DOI: 10.1063/1.2354545.

[141] M. Buchner *et al.*: Tutorial: Basic Principles, Limits of Detection, and Pitfalls of Highly Sensitive SQUID Magnetometry for Nanomagnetism and Spintronics. *Journal of Applied Physics* **124**, 161101 (2018). DOI: 10.1063/1.5045299.

[142] M. A. Garcia *et al.*: Sources of Experimental Errors in the Observation of Nanoscale Magnetism. *Journal of Applied Physics* **105**, 013925 (2009). DOI: 10.1063/1.3060808.

[143] P. Stamenov and J. M. D. Coey: Sample Size, Position, and Structure Effects on Magnetization Measurements Using Second-Order Gradiometer Pickup Coils. *Review of Scientific Instruments* **77**, 015106 (2006). DOI: 10.1063/1.2149190.

[144] H. Hopster and H. P. Oepen, eds.: *Magnetic Microscopy of Nanostructures*. 1st ed. Springer, Berlin, New York, 2004. ISBN: 978-3-540-40186-5.

[145] M. J. Benitez *et al.*: Magnetic Microscopy and Topological Stability of Homochiral Néel Domain Walls in a $Pt/Co/AlO_x$ Trilayer. *Nature Communications* **6**, 8957 (2015). DOI: 10.1038/ncomms9957.

[146] M. Heigl *et al.*: Dipolar-Stabilized First and Second-Order Antiskyrmions in Ferrimagnetic Multilayers. *Nature Communications* **12**, 2611 (2021). DOI: 10.1038/s41467-021-22600-7.

[147] J. M. D. Coey *et al.*: Magnetic Structure of an Amorphous Rare-Earth Transition-Metal Alloy. *Physical Review Letters* **36**, 1061–1064 (1976). DOI: 10.1103/PhysRevLett.36.1061.

[148] L. Caretta *et al.*: Fast Current-Driven Domain Walls and Small Skyrmions in a Compensated Ferrimagnet. *Nature Nanotechnology* **13**, 1154–1160 (2018). DOI: 10.1038/s41565-018-0255-3.

[149] K. Chen *et al.*: Observation of Compact Ferrimagnetic Skyrmions in DyCo3 Film. *Nanoscale* **12**, 18137–18143 (2020). DOI: 10.1039/D0NR02947E.

[150] S. Yang *et al.*: Fundamentals and Applications of the Skyrmion Hall Effect. *Applied Physics Reviews* **11**, 041335 (2024). DOI: 10.1063/5.0218280.

[151] F. Büttner *et al.*: Field-Free Deterministic Ultrafast Creation of Magnetic Skyrmions by Spin–Orbit Torques. *Nature Nanotechnology* **12**, 1040–1044 (2017). DOI: 10.1038/nnano.2017.178.

[152] T. Herranen and L. Laurson: Domain Walls within Domain Walls in Wide Ferromagnetic Strips. *Physical Review B* **92**, 100405 (2015). DOI: 10.1103/PhysRevB.92.100405.

[153] J. Hütner, T. Herranen, and L. Laurson: Multistep Bloch-line-mediated Walker Breakdown in Ferromagnetic Strips. *Physical Review B* **99**, 174427 (2019). DOI: 10.1103/PhysRevB.99.174427.

[154] H. A. Dürr *et al.*: Chiral Magnetic Domain Structures in Ultrathin FePd Films. *Science* **284**, 2166–2168 (1999). DOI: 10.1126/science.284.5423.2166.

[155] J.-Y. Chauleau *et al.*: Chirality in Magnetic Multilayers Probed by the Symmetry and the Amplitude of Dichroism in X-Ray Resonant Magnetic Scattering. *Physical Review Letters* **120**, 037202 (2018). DOI: 10.1103/PhysRevLett.120.037202.

[156] L.-C. Peng *et al.*: Lorentz Transmission Electron Microscopy Studies on Topological Magnetic Domains. *Chinese Physics B* **27**, 066802 (2018). DOI: 10.1088/1674-1056/27/6/066802.

[157] M. A. Marioni *et al.*: Halbach Effect at the Nanoscale from Chiral Spin Textures. *Nano Letters* **18**, 2263–2267 (2018). DOI: 10.1021/acs.nanolett.7b04802.

[158] G. Chen *et al.*: Tailoring the Chirality of Magnetic Domain Walls by Interface Engineering. *Nature Communications* **4**, 2671 (2013). DOI: 10.1038/ncomms3671.

[159] G. Chen *et al.*: Novel Chiral Magnetic Domain Wall Structure in Fe / Ni / Cu (001) Films. *Physical Review Letters* **110**, 177204 (2013). DOI: 10.1103/PhysRevLett.110.177204.

[160] E. C. Corredor *et al.*: SEMPA Investigation of the Dzyaloshinskii-Moriya Interaction in the Single, Ideally Grown Co/Pt(111) Interface. *Physical Review B* **96**, 060410 (2017). DOI: 10.1103/PhysRevB.96.060410.

[161] K. Chen *et al.*: Temperature-Dependent Magnetic Properties of Ferrimagnetic $DyCo_3$ Alloy Films. *Physical Review B* **91**, 024409 (2015). DOI: 10.1103/PhysRevB.91.024409.

[162] P. Hansen *et al.*: Magnetic and Magneto-optical Properties of Rare-earth Transition-metal Alloys Containing Dy, Ho, Fe, Co. *Journal of Applied Physics* **69**, 3194–3207 (1991). DOI: 10.1063/1.348561.

[163] A.-O. Mandru *et al.*: Pervasive Artifacts Revealed from Magnetometry Measurements of Rare Earth-Transition Metal Thin Films. *Journal of Vacuum Science & Technology A* **38**, 023409 (2020). DOI: 10.1116/1.5135504.

[164] T. Kobayashi *et al.*: Magnetization Process of Exchange-Coupled Ferrimagnetic Double-Layered Films. *Japanese Journal of Applied Physics* **20**, 2089 (1981). DOI: 10.1143/JJAP.20.2089.

[165] K. Chen *et al.*: Observation of a Chirality-Induced Exchange-Bias Effect. *Physical Review Applied* **12**, 024047 (2019). DOI: 10.1103/PhysRevApplied.12.024047.

[166] S. Kim *et al.*: Magnetic Droplet Nucleation with a Homochiral Néel Domain Wall. *Physical Review B* **95**, 220402 (2017). DOI: 10.1103/PhysRevB.95.220402.

[167] F. P. Chmiel *et al.*: Observation of Magnetic Vortex Pairs at Room Temperature in a Planar α-Fe_2O_3/Co Heterostructure. *Nature Materials* **17**, 581–585 (2018). DOI: 10.1038/s41563-018-0101-x.

[168] A. Vansteenkiste *et al.*: The Design and Verification of MuMax3. *AIP Advances* **4**, 107133 (2014). DOI: 10.1063/1.4899186.

[169] J. Schwenk *et al.*: Bimodal Magnetic Force Microscopy with Capacitive Tip-Sample Distance Control. *Applied Physics Letters* **107**, 132407 (2015). DOI: 10.1063/1.4932174.

[170] H. J. Hug *et al.*: Quantitative Magnetic Force Microscopy on Perpendicularly Magnetized Samples. *Journal of Applied Physics* **83**, 5609–5620 (1998). DOI: 10.1063/1.367412.

[171] X. Zhao *et al.*: Magnetic Force Microscopy with Frequency-Modulated Capacitive Tip–Sample Distance Control. *New Journal of Physics* **20**, 013018 (2018). DOI: 10.1088/1367-2630/aa9ca9.

[172] A.-O. Mandru *et al.*: Coexistence of Distinct Skyrmion Phases Observed in Hybrid Ferromagnetic/Ferrimagnetic Multilayers. *Nature Communications* **11**, 6365 (2020). DOI: 10.1038/s41467-020-20025-2.

[173] H. S. Cho *et al.*: Characteristics of 360°-Domain Walls Observed by Magnetic Force Microscope in Exchange-Biased NiFe Films. *Journal of Applied Physics* **85**, 5160–5162 (1999). DOI: 10.1063/1.369110.

[174] N. Chowdhury *et al.*: 360° Domain Walls in Magnetic Thin Films with Uniaxial and Random Anisotropy. *Physical Review B* **98**, 134440 (2018). DOI: 10.1103/PhysRevB.98.134440.

[175] P. J. A. van Schendel *et al.*: A Method for the Calibration of Magnetic Force Microscopy Tips. *Journal of Applied Physics* **88**, 435–445 (2000). DOI: 10.1063/1.373678.

[176] T. A. Butcher *et al.*: Ptychographic Nanoscale Imaging of the Magnetoelectric Coupling in Freestanding BiFeO. *Advanced Materials* **36**, 2311157 (2024). DOI: 10.1002/adma.202311157.

[177] C. Donnelly *et al.*: Three-Dimensional Magnetization Structures Revealed with X-ray Vector Nanotomography. *Nature* **547**, 328–331 (2017). DOI: 10.1038/nature23006.

[178] A. Apseros *et al.*: X-Ray Linear Dichroic Tomography of Crystallographic and Topological Defects. *Nature* **636**, 354–360 (2024). DOI: 10.1038/s41586-024-08233-y.

[179] K. Witte *et al.*: From 2D STXM to 3D Imaging: Soft X-ray Laminography of Thin Specimens. *Nano Letters* **20**, 1305–1314 (2020). DOI: 10.1021/acs.nanolett.9b04782.

[180] C. Donnelly *et al.*: Time-Resolved Imaging of Three-Dimensional Nanoscale Magnetization Dynamics. *Nature Nanotechnology* **15**, 356–360 (2020). DOI: 10.1038/s41565-020-0649-x.

[181] A. Bardea and R. Naaman: Magnetolithography: From Bottom-Up Route to High Throughput. *Small* **5**, 316–319 (2009). DOI: 10.1002/smll.200801058.

[182] S. Manipatruni, D. E. Nikonov, and I. A. Young: Beyond CMOS Computing with Spin and Polarization. *Nature Physics* **14**, 338–343 (2018). DOI: 10.1038/s41567-018-0101-4.

[183] A. D. Kent and D. C. Worledge: A New Spin on Magnetic Memories. *Nature Nanotechnology* **10**, 187–191 (2015). DOI: 10.1038/nnano.2015.24.

[184] M. Hoffmann *et al.*: Negative Capacitance in HfO2- and ZrO2-Based Ferroelectrics. In: *Ferroelectricity in Doped Hafnium Oxide: Materials, Properties and Devices*. Ed. by U. Schroeder, C. S. Hwang, and H. Funakubo. Woodhead Publishing, 2019, 473–493. ISBN: 978-0-08-102430-0. DOI: 10.1016/B978-0-08-102430-0.00023-1.

[185] A. Sebastian *et al.*: Memory Devices and Applications for In-Memory Computing. *Nature Nanotechnology* **15**, 529–544 (2020). DOI: 10.1038/s41565-020-0655-z.

[186] A. Berger, B. Lengsfield, and Y. Ikeda: Determination of Intrinsic Switching Field Distributions in Perpendicular Recording Media (Invited). *Journal of Applied Physics* **99**, 08E705 (2006). DOI: 10.1063/1.2164416.

[187] D. C. Worledge *et al.*: Switching Distributions and Write Reliability of Perpendicular Spin Torque MRAM. In: *2010 International Electron Devices Meeting*. 2010, 12.5.1–12.5.4. DOI: 10.1109/IEDM.2010.5703349.

[188] M. Baumgartner *et al.*: Spatially and Time-Resolved Magnetization Dynamics Driven by Spin–Orbit Torques. *Nature Nanotechnology* **12**, 980–986 (2017). DOI: 10.1038/nnano.2017.151.

[189] T. W. B. Kibble: Topology of Cosmic Domains and Strings. *Journal of Physics A: Mathematical and General* **9**, 1387 (1976). DOI: 10.1088/0305-4470/9/8/029.

[190] W. Zurek: Cosmological Experiments in Condensed Matter Systems. *Physics Reports* **276**, 177–221 (1996). DOI: 10.1016/S0370-1573(96)00009-9.

[191] T. Eggebrecht *et al.*: Light-Induced Metastable Magnetic Texture Uncovered by *in Situ* Lorentz Microscopy. *Physical Review Letters* **118**, 097203 (2017). DOI: 10.1103/PhysRevLett.118.097203.

[192] S.-Z. Lin *et al.*: Topological Defects as Relics of Emergent Continuous Symmetry and Higgs Condensation of Disorder in Ferroelectrics. *Nature Physics* **10**, 970–977 (2014). DOI: 10.1038/nphys3142.

[193] S. M. Griffin and N. A. Spaldin: On the Relationship between Topological and Geometric Defects. *Journal of Physics: Condensed Matter* **29**, 343001 (2017). DOI: 10.1088/1361-648X/aa7b5c.

[194] J. Gorchon *et al.*: Role of Electron and Phonon Temperatures in the Helicity-Independent All-Optical Switching of GdFeCo. *Physical Review B* **94**, 184406 (2016). DOI: 10.1103/PhysRevB.94.184406.

[195] P. Hansen *et al.*: Magnetic and Magneto-optical Properties of Rare-earth Transition-metal Alloys Containing Gd, Tb, Fe, Co. *Journal of Applied Physics* **66**, 756–767 (1989). DOI: 10.1063/1.343551.

[196] J. Hintermayr, A. Ullrich, and M. Albrecht: Structure and Magnetic Properties of Ferrimagnetic $[Gd/Fe]_n$ Multilayer and Gd_xFe_{100-x} Thin Films. *AIP Advances* **11**, 095214 (2021). DOI: 10.1063/5.0057667.

[197] P. Hansen and M. Urner-Wille: Magnetic and Magneto-Optic Properties of Amorphous GdFeBi-films. *Journal of Applied Physics* **50**, 7471–7476 (1979). DOI: 10.1063/1.326923.

[198] Y. A. Shokr *et al.*: Steering of Magnetic Domain Walls by Single Ultrashort Laser Pulses. *Physical Review B* **99**, 214404 (2019). DOI: 10.1103/PhysRevB.99.214404.

[199] A. Donges *et al.*: Unveiling Domain Wall Dynamics of Ferrimagnets in Thermal Magnon Currents: Competition of Angular Momentum Transfer and Entropic Torque. *Physical Review Research* **2**, 013293 (2020). DOI: 10.1103/PhysRevResearch.2.013293.

[200] J. Theile, R. A. Kosinski, and J. Engemann: Numerical Computations of Vertical Bloch Lines Motion in the Presence of a Periodic In-Plane Magnetic Field. *Journal of Magnetism and Magnetic Materials* **62**, 139–142 (1986). DOI: 10.1016/0304-8853(86)90135-6.

[201] S. Wall *et al.*: Ultrafast Changes in Lattice Symmetry Probed by Coherent Phonons. *Nature Communications* **3**, 721 (2012). DOI: 10.1038/ncomms1719.

[202] J. Zang, V. Cros, and A. Hoffmann, eds.: *Topology in Magnetism*. Springer International Publishing, Cham, 2018. ISBN: 978-3-319-97333-3. DOI: 10.1007/978-3-319-97334-0.

[203] H.-B. Braun: Topological Effects in Nanomagnetism: From Superparamagnetism to Chiral Quantum Solitons. *Advances in Physics* **61**, 1–116 (2012). DOI: 10.1080/00018732.2012.663070.

[204] A. Fert, N. Reyren, and V. Cros: Magnetic Skyrmions: Advances in Physics and Potential Applications. *Nature Reviews Materials* **2**, 1–15 (2017). DOI: 10.1038/natrevmats.2017.31.

[205] S. Woo *et al.*: Deterministic Creation and Deletion of a Single Magnetic Skyrmion Observed by Direct Time-Resolved X-ray Microscopy. *Nature Electronics* **1**, 288–296 (2018). DOI: 10.1038/s41928-018-0070-8.

[206] S.-G. Je *et al.*: Creation of Magnetic Skyrmion Bubble Lattices by Ultrafast Laser in Ultrathin Films. *Nano Letters* **18**, 7362–7371 (2018). DOI: 10.1021/acs.nanolett.8b03653.

[207] L.-M. J. Kern: Controlled Manipulation of Magnetic Skyrmions: Generation, Motion and Dynamics. PhD thesis. Technische Universität Berlin, Berlin, 2023.

[208] K. Gerlinger *et al.*: Application Concepts for Ultrafast Laser-Induced Skyrmion Creation and Annihilation. *Applied Physics Letters* **118**, 192403 (2021). DOI: 10.1063/5.0046033.

[209] C. Chappert *et al.*: Planar Patterned Magnetic Media Obtained by Ion Irradiation. *Science* **280**, 1919–1922 (1998). DOI: 10.1126/science.280.5371.1919.

[210] M. C. H. de Jong *et al.*: Local Control of Magnetic Interface Effects in Chiral Ir|Co|Pt multilayers using Ga^+ Ion Irradiation. *Physical Review B* **105**, 064429 (2022). DOI: 10.1103/PhysRevB.105.064429.

[211] N. S. Gusev *et al.*: Modification of the Interfacial Dzyaloshinskii–Moriya Interaction in Cobalt/Heavy Metal Films Irradiated with Helium Ions. *Physics of the Solid State* **63**, 1373–1377 (2021). DOI: 10.1134/S1063783421090110.

[212] R. Juge *et al.*: Helium Ions Put Magnetic Skyrmions on the Track. *Nano Letters* **21**, 2989–2996 (2021). DOI: 10.1021/acs.nanolett.1c00136.

[213] Y. Zhao *et al.*: Local Manipulation of Skyrmion Nucleation in Microscale Areas of a Thin Film with Nitrogen-Ion Implantation. *ACS Applied Materials & Interfaces*, 15004–15013 (2023). DOI: 10.1021/acsami.3c00266.

[214] K. Fallon *et al.*: Controlled Individual Skyrmion Nucleation at Artificial Defects Formed by Ion Irradiation. *Small* **16**, 1907450 (2020). DOI: 10.1002/smll.201907450.

[215] S. Miki *et al.*: Spatial Control of Skyrmion Stabilization Energy by Low-Energy Ga^+ Ion Implantation. *Applied Physics Letters* **122**, 202401 (2023). DOI: 10.1063/5.0153768.

[216] M. Hassan *et al.*: Dipolar Skyrmions and Antiskyrmions of Arbitrary Topological Charge at Room Temperature. *Nature Physics* **20**, 615–622 (2024). DOI: 10.1038/s41567-023-02358-z.

[217] K. Yosida: *Functional Analysis*. Vol. 123. Springer-Verlag, Berlin, Heidelberg, 1995. ISBN: 978-3-540-58654-8. DOI: 10.1007/978-3-642-61859-8.

[218] S. D. Pollard *et al.*: Observation of Stable Néel Skyrmions in Cobalt/Palladium Multilayers with Lorentz Transmission Electron Microscopy. *Nature Communications* **8**, 14761 (2017). DOI: 10.1038/ncomms14761.

[219] S. Zayko *et al.*: Ultrafast High-Harmonic Nanoscopy of Magnetization Dynamics. *Nature Communications* **12**, 6337 (2021). DOI: 10.1038/s41467-021-26594-0.

[220] F. Büttner *et al.*: Magnetic States in Low-Pinning High-Anisotropy Material Nanostructures Suitable for Dynamic Imaging. *Physical Review B* **87**, 134422 (2013). DOI: 10.1103/PhysRevB.87.134422.

[221] B. Pfau: Imaging Magnetic Nanostructures using Soft X-ray Fourier Transform Holography. PhD thesis. Technische Universität Berlin, Berlin, 2013.

[222] W. Legrand *et al.*: Spatial Extent of the Dzyaloshinskii-Moriya Interaction at Metallic Interfaces. *Physical Review Materials* **6**, 024408 (2022). DOI: 10.1103/PhysRevMaterials.6.024408.

[223] R. Lavrijsen: Another Spin in the Wall : Domain Wall Dynamics in Perpendicularly Magnetized Devices. PhD thesis. Technische Universiteit Eindhoven, Eindhoven, 2011. ISBN: 9789038624174. DOI: 10.6100/IR693486.

Acknowledgments

Reflecting on the past five years, I am deeply grateful to the many individuals who have positively influenced my PhD journey. Their help and input have been instrumental, and I extend my heartfelt thanks to each of them.

First and foremost, I would like to express my sincere gratitude to Prof. Felix Büttner for offering me the opportunity to pursue a PhD in his group. Thank you for providing me with numerous opportunities to acquire new skills, meet collaboration partners, and conduct high-level research. Your support in terms of access to facilities, outreach, and scientific input has been invaluable. I am also grateful for your guidance in scientific writing. I hope this work shows that it has not been in vain.

I want to thank Prof. Hans Josef Hug and Prof. Reinoud Lavrijsen for their willingness to act as evaluators for my thesis.

Special thanks go to Lisa Kern, Tamer Karaman, and Riccardo Battistelli for meticulously proofreading large portions of the manuscript. Your comments were extremely appreciated.

I have had the pleasure of collaborating with many wonderful individuals, whether as office mates, group members, long-term collaborators, or during beamtimes at large-scale facilities.

I was in the unique position of being one of the very first members of the Maxray group at the Helmholtz Zentrum Berlin (and later also Augsburg), which has grown considerably since 2020. Thank you to all my colleagues for the great and harmonious working atmosphere. I want to particularly thank Tamer Karaman, Sascha Petz, Steffen Wittrock, and Kai Litzius for their incredible support in the lab and during beamtimes, as well as for the healthy scientific discussions (and somewhat less healthy snacks).

Special thanks go to Riccardo Battistelli, with whom I started my PhD journey. You have been an amazing colleague, and I am confident that you will complete your own PhD with great success very soon.

Due to many collaborations, I also had the pleasure of working with many scientists from the Max-Born-Institute. I want to thank Michael Schneider, Lisa Kern, Kathinka Gerlinger, Christopher Klose, Josefin Fuchs, Victor Deinhart, Martin Hennecke, Themistoklis Sidiropoulos, Dieter Engel, Felix Steinbach, Christian Günther, Clemens von Korff-Schmising, and Bastian Pfau for their support before

and during beamtimes, as well as during many other experiments in the lab, scientific input as well as IT-support at times.
I am also particularly grateful to the beamline scientists of the BOREAS endstation at ALBA, especially Manuel Valvidares, the scientists of the MAXYMUS microscope at BESSY-II, especially Sebastian Wintz, and the scientists of the SCS endstation at European XFEL, especially Giuseppe Mercurio and Robert Carley. Thank you for investing countless hours, day and night, to ensure the success of our experiments.
In the same breath I also have to thank Sascha Petz, Dieter Engel, Michael Schneider, and Riccardo Battistelli for preparing numerous samples, often on very short notice and sometimes even during ongoing beamtimes.
My thanks also go to the groups of Prof. Hans Josef Hug, Prof. Johan Mentink, and Prof. Claus Ropers for providing measurements and simulations crucial to my projects. Without this data, the presented studies would have been far less comprehensive.
I am especially grateful to Bastian Pfau for allowing me to complete my thesis and papers while already working in his group. Yes, I am actually finished now!
Finally, I want to thank my friends from the KSG for making the latter half of my studies so much more enjoyable, and my family for always being there as a haven to return to.